McGILL UNIVERSITY

MASTER'S THESIS

Evaluating MODIS Collection 6 Arctic low-level, single-layer cloud properties during polar day using active remote sensing.

Author:
Henry CARR

Supervisor:
Dr. Andreas ZUEND

Department of Atmospheric and Oceanic Sciences
McGill University, Montreal

September 2023

A thesis submitted to McGill University in partial fulfillment of the requirements of the degree of Master of Science

McGill

MCGILL UNIVERSITY

Abstract

It is known that low-level Arctic clouds are largely responsible for the disagreement in Arctic warming in contemporary climate models. To constrain this uncertainty, accurate retrievals of low-level (less than or equal to 2 km above the surface) cloud-top-height (CTH), cloud fraction and cloud-phase are needed. A comparison of CTH, cloud fraction and cloud-phase is presented between the Moderate Resolution Imaging Spectroradiometer (MODIS) instrument on the Aqua satellite and the Cloud-Aerosol Lidar with Orthogonal Polarization (CALIOP) instrument, where CALIOP is taken to be ground-truth. Single-layer clouds are chosen since MODIS cannot infer the vertical structure of the atmosphere as a passive remote sensing instrument.

Over 1,265,000 cloud comparisons were made for single-layer clouds below 2 km and north of 60 $^{\circ}N$ in 2015 March 1st – September 30th (polar-day). We aimed to first analyze MODIS CTH biases, which are defined relative to CALIOP. We propose two hypotheses for CTH. First, lower-tropospheric-stability (LTS) impacts the CTH bias due to the use of brightness temperature (BT) in the low-level CTH retrieval algorithm. Composites of CTH as a function of LTS and MODIS cloud optical depth suggest that the use of an average Arctic LTS in the MODIS algorithm may result in small biases in CTH due to compensating effects, however, local impacts on CTH retrievals may be large. Moreover, we show that there is a strong geographic dependence of CTH biases. The second CTH hypothesis states that the zonal averaging of the apparent brightness temperature lapse rate (BTLR) and the neglect of surface emissivity differences between sea-ice and open-ocean areas in CTH calculations result in biases. We replicate the calculation of BTLR and CTH values using collocated CALIOP CTH retrievals, MODIS BT retrievals, and clear-sky BT computed with the Community Radiative Transfer Model (CRTM) model. We show that while surface emissivity does impact

CTH computations, large individual errors in CTH might arise with discrepancies between modelled and measured BTs.

Finally, we analyze the CloudMask algorithm against the 2B-GEOPROF-LIDAR instrument and cloud-phase detection algorithm against CALIOP. The CloudMask bias was found to have a surface dependence, and the 10 $^{\circ}$ longitude $\times$ 3 $^{\circ}$ latitude daily average cloud fraction overestimated the 2B-GEORPOF-LIDAR average cloud fraction. Two MODIS 1 *km* thermodynamic phase retrieval techniques (named the Tri-spectral IR thermodynamic phase test, TIR, and Optical Properties phase retrieval, OP) were compared to CALIOP's own phase retrieval algorithm. It was found that agreement between CALIOP and MODIS decreased when sea-ice fractional cover, from collocated AMSR-E retrievals, increased above 0% which may be expected due to issues with MODIS detecting clouds over ice, and that the OP method performed better than the TIR method.

The results have implications for improvements in the passive retrieval of Arctic cloud macrophysical properties. In particular, quantifying the effect of LTS and underlying surface assumptions in CTH.

MCGILL UNIVERSITY

Résumé

Il est connu que les nuages de l'Arctique de basse altitude sont largement responsables de l'incertitude concernant le réchauffement de l'Arctique dans les modèles climatiques contemporains. Pour contraindre cette incertitude, des mesures précises de la hauteur du sommet des nuages (HSN) de basse altitude (moins que ou égal à 2 *km* au dessus de la surface), de la fraction de nuages et de la phase nuageuse sont nécessaires. Une comparaison de la HSN et de la fraction de nuages et de la phase nuageuse est présentée entre l'instrument Moderate Resolution Imaging Spectroradiometer (MODIS) sur le satellite Aqua et l'instrument Cloud-Aerosol Lidar with Orthogonal Polarization (CALIOP), où CALIOP est considéré comme la vérité de terrain. Nous choisissons ici des nuages monocouches car MODIS ne peut pas déterminer la structure verticale de l'atmosphère en tant qu'instrument de télédétection passive. Plus de 1 265 000 comparaisons de nuages ont été effectuées pour des nuages monocouches dont l'altitude est en dessous de 2 *km* et au nord de 60°N entre le 1er mars et le 30 septembre 2015 (jour polaire).

Nous avons d'abord cherché à analyser les biais HSN MODIS, définis par rapport à CALIOP. La première hypothèses, l'instabilité de la basse troposphère (IBT) a un impact sur le biais de la HSN dû à l'utilisation de la température de brillance (TB) dans l'algorithme de récupération de la HSN de basse altitude. Des composites de la HSN en fonction de l'IBT et de la profondeur optique des nuages MODIS suggèrent que l'utilisation d'une IBT arctique moyenne dans l'algorithme MODIS peut entraîner de petits biais dans la HSN dus à des effets compensatoires, mais que l'impact local sur les récupérations de la HSN peuvent être importants. De plus, nous montrons que les biais de HSN ont une grande dépendance géographique.

La deuxième hypothèse concernant la HSN indique que la moyenne zonale du gradient de température de brillance (GTB) apparent et l'omission des différences

d'émissivité de surface entre la glace de mer et la haute mer utilisées dans les calculs de HSN entraînent des biais. Nous avons reproduit le calcul des valeurs de GTB et de hauteur de nuage en utilisant des récupérations de hauteur de nuage de CALIOP colocalisées, des récupérations de TB de MODIS et des récupérations de TB pour un ciel clair calculées avec le Community Radiative Transfer Model (CRTM). Nous montrons que tandis que l'émissivité de surface a un impact sur les calculs de HSN, de grandes erreurs individuelles dans la HSN peuvent provenir des différences entre les TBs modélisées et mesurées.

Enfin, nous analysons l'algorithme CloudMask par rapport à l'instrument 2B-GEOPROF-LIDAR et l'algorithme de détection de phase nuageuse par rapport à CALIOP. Il a été constaté que le biais de CloudMask dépendait de la surface, et la fraction nuageuse moyenne quotidienne sur 10 $^{\circ}$ longitude $\times$ 3 $^{\circ}$ latitude surestimait la fraction nuageuse moyenne de 2B-GEORPOF-LIDAR. Deux techniques de récupération de phase thermodynamique MODIS 1 *km* (appelées test de phase thermodynamique IR trispectral, IRT, et récupération de phase des propriétés optiques, PO) ont été comparées à l'algorithme de récupération de phase de CALIOP. Il a été constaté que l'accord entre CALIOP et MODIS diminuait lorsque la fraction de la couverture de glace de mer, calculée à partir de récupérations AMSR-E colocalisées, augmentait au-dessus de 0 %, ce qui peut être attendu en raison de problèmes de détection des nuages par MODIS au-dessus de la glace, et que la méthode PO avait de meilleurs résultats que la méthode IRT. Les résultats ont des implications pour l'amélioration de la mesure passive des propriétés macrophysiques des nuages arctiques - il s'agit de quantifier l'effet de l'IBT et des hypothèses de surface sous-jacentes dans les récupérations de la HSN, et de comprendre les impacts de la surface terrestre sur les mesures de fraction de nuages.

Acknowledgements

I would like to thank Dr. Andreas Zuend for his guidance and support. I would like to thank the rest of my research group for the helpful discussions throughout my time researching, in particular Dr. Quentin Coopman for his help navigating technical satellite data. I would also like to thank Dr. Chenxi Wang for his help throughout this project collocating and navigating satellite data. I would like to thank both my parents, Haylie & Charles Carr, for all the support over the years and for introducing me to the world of science, and my brother Rupert Carr for convincing me to get into coding.

Contribution of Authors

The research for this thesis was carried out by myself.

Dr. Chenxi Wang, an external collaborator, collocated the MODIS, CALIOP ("Pixel by Pixel Collocation", Section 3.2), and AMSR-E data used in the cloud top height and phase hitrate analysis.

The scripts for the analysis ("Hypothesis 1", Section 3.3) were written by me, and the subsequent analysis, interpretation and discussion was performed and written by me.

Chenxi Wang provided the source code for the Community Radiative Transfer Model (CRTM) which was subsequently edited by me, used for the analysis of the second cloud top height hypothesis ("Hypothesis 2 – Importance of Surface Type Emissivity", Section 2.2). The codes to incorporate surface, environment, MODIS and CALIOP variables into the CRTM code, and to perform further analysis were written by me ("Hypothesis 2", Section 3.4). The subsequent analysis, interpretation and discussion was performed and written by me.

For the CloudMask and 2B-GEOPROF-LIDAR cloud fraction comparison ("Cloud-Mask and Cloud Fractional Agreement", Section 3.5.1), the scripts for the collocation and analysis were written by me, and the subsequent analysis, interpretation and discussion was performed and written by me.

For the idea of comparing CALIOP and MODIS phase hitrate ("Cloud-Phase Hitrate", Section 3.5.2), the scripts for the analysis were written by me, and the subsequent analysis and interpretation was performed and written by me.

Contents

List of Figures

List of Tables

Nomenclature

Acronym	**Description**
ADA	advanced doubling adding
AMSR-E	Advanced Microwave Scanning Radiometer for the Earth Observing System
BT	Brightness Temperature
BTLR	Apparent 11 μm Brightness Temperature Lapse Rate
CALIOP	Cloud-Aerosol Lidar with Orthogonal Polarization
CALIPSO	Cloud-Aerosol Lidar and Infrared Pathfinder Satellite Observation
CMIP	Coupled Model Intercomparison Project
COT	Cloud Optical Thickness
CPR	CloudSat Cloud Profiling Radar
CRTM	Community Radiative Transfer Model
CSR	Clear-Sky-Restoral
CTH	Cloud Top Height
CTP	Cloud Top Pressure
CTT	Cloud Top Temperature
ERA5	European Environment Agency
FOV	Field-of-View
GDAS	Global Data Assimulation System
GEOS	Goddard Earth Observing System
GIFOV	Ground Instantaneous Field-of-View
Lidar	Light Detection and Ranging
LTS	Lower Tropospheric Stability
LUT	Look-Up-Table
MERRA2	Modern Era Retrospective Analysis for Research and Applications Version 2
MODIS	Moderate Resolution Imaging Spectroradiomenter

Acronym	Description
MYD06	MODIS Aqua Level 2 1 *km* Data Product
NASA	National Aeronautic and Space Administration
NIR	Near-Infrared
OP	Optical Properties phase test
OSSE	Observing system simulation experiment
PCL	Partly Cloudy Pixels
PFAAST	Pressure layer Fast Algorithm for Atmospheric Transmittances
SOI	Successive Order of Interaction
SSMI	Special Sensor Microwave Imager
SWIR	Shortwave Infrared
TIR	Tri-spectral IR thermodynamic phase test
TOA	Top of the Atmosphere
VIS	Visible

Chapter 1

Introduction

1.1 Arctic Amplification

Global surface temperatures have increased by greater than 1 °C when measured over the period 1901–2016 (Wuebles et al., 2017) due to anthropogenic gasses like carbon dioxide and methane. Anthropogenic gases can induce a greenhouse effect warming surface temperatures globally, which in turn can induce effects that amplify the warming in the Arctic, an effect known as Arctic Amplification. A large amount of uncertainty remains in the physical processes governing the evolution of Arctic Amplification (Taylor et al., 2021). A large proportion of this uncertainty is due to how low-level clouds are represented in climate models. Zelinka et al. (2020) showed that low-level clouds drive a large proportion of the spread of warming predicted by different models in their global feedback analysis, though it is important to note that their paper did not focus on the Arctic. The importance of clouds for global surface warming is largely due to their radiative feedback effects. Feedback effects describe how changes to variables (other than surface-temperature) due to surface warming impact the incoming and outgoing radiation entering into and leaving the Earth's atmosphere, which in turn feedbacks onto the pre-perturbed surface temperature. In particular, low-level Arctic cloud feedback effects describe how changes to Arctic low-level cloud properties (such as low-level cloud cover amount) due to climate warming in turn affect the shortwave and longwave radiation budgets by either amplifying surface warming (positive feedback) or by dampening surface warming (negative feedback).

While low-level clouds are particularly important for the global mean of the shortwave radiation feedback (Zelinka et al., 2012a), it is known that in the Arctic they also play a crucial role in the longwave radiation feedback (Curry et al., 1996). Low-level clouds emit downwelling longwave radiation towards the Arctic surface, acting to heat the surface. In the Arctic, the annual total downwelling radiation at the surface in the longwave is double that in the shortwave, largely due to the fact that in the polar-night between 1st October – 1st March (depending on the specific latitude) the downwelling shortwave radiation is negligible in comparison (Curry et al., 1996). However, a large amount of uncertainty remains in low-level Arctic clouds and their feedbacks, which play a large role in the spread of warming modelled in the Arctic. For example, Taylor et al. (2019) showed that the differences in models for cloud amount (i.e. the horizontal extent of cloud coverage) was largest for low-level clouds.

In a study that did focus on Arctic Amplification, Hahn et al. (2021) showed that cloud feedback contributes negatively to the annual and zonal mean near-surface warming ($^\circ C$) in scenarios of centered around year-100 of abrupt CO_2 quadrupling (in contrast to the positive contribution seen in the tropics from cloud feedbacks). More specifically, there was stronger warming in the Arctic in phase 6 of the Coupled Model Intercomparison Project (CMIP6) models (an ensemble of models aiming to compare the latest outcomes of global climate models) than the phase 5 (CMIP5) models mostly due to less-negative shortwave low-level cloud amount and scattering feedback. The shortwave scattering feedback is closely tied to cloud optical depth (τ) (Ceppi et al., 2017), and describes how much incident shortwave radiation from space is scattered by the cloud and how this in turn impacts the shortwave radiation budget. These studies show that low-level cloud amount plays a crucial role in the radiative feedback processes governing Arctic Amplification. However there are three more low-level cloud properties that are crucial for understanding the evolution of low-level cloud feedback in the Arctic: cloud-top-pressure (CTP), τ, and cloud-phase.

Zelinka et al. (2012a) used a radiative transfer model method to break up changes to clouds into a diagnostic framework of CTP and τ bins to analyse the net radiative forcing due to changes in cloud amount from a doubling of carbon dioxide. Zelinka et al. (2012a) showed that the sign and strength of the contribution of the changes to the total cloud radiative feedback was dependent on CTP and τ. Moreover, Zelinka et al. (2012a) showed that the shortwave feedback is dominated by low-level cloud changes that contribute positively to the ensemble mean global mean cloud feedback. Low level clouds (as defined by Zelinka et al., 2012a as $680 < \text{CTP} \leq 1000\,hPa$) contributed positively to the global and annual mean of the shortwave feedback with a net shortwave cloud feedback across all latitudes of 0.31 $Wm^{-2}K{-}1$. Meanwhile high clouds ($50 < \text{CTP} \leq 440$ hPa) generally contribute negatively with a net shortwave cloud feedback across all latitudes of -0.19 $Wm^{-2}K{-}1$. Interestingly for latitudes greater than 70 $^{\circ}N$, both high and low clouds contribute negatively to the shortwave cloud feedback.

Moreover, the multi-model-mean net cloud feedback for cloud altitude changes was shown to be in general positive (Ceppi et al., 2017; Zelinka et al., 2016). More specifically, Zelinka et al., 2012b showed that the global mean change in cloud-fraction weighted CTP per degree of warming was -3.68 hPa K^{-1} and that this lead to an annual and ensemble global mean longwave feedback due to cloud-top altitude changes of 0.39 W m^2 K^{-1}. The result for shortwave feedback was -0.07 W m^2 K^{-1}. Importantly, the change in cloud-fraction weighted CTP were negative nearly everywhere except regions dominated by low-level clouds such as the Arctic. Correctly classifying CTP is therefore important for correctly determining the magnitude of cloud feedback.

Zelinka et al., 2012a also showed that the strength and sign of the shortwave feedback closely related to τ. This is because τ governs the amount of incoming shortwave radiation (sunlight) that is reflected back out to space through the top of the atmosphere (TOA), though it is important to highlight that τ also affects longwave downwelling radiation strongly in the Arctic particularly when there is no sunlight in the polar-night (Curry et al., 1996; Intrieri et al., 2002). Zelinka et al., 2012a found, more specifically, that the sign of the contribution of clouds to the ensemble mean zonal mean shortwave feedback depends on both latitude and cloud thickness, with thick clouds ($\tau \geq 23$) contributing negatively for latitudes greater than 50°, while contributing positively equatorward of about 45°. In contrast, thin clouds ($\tau < 3.6$) contribute minimally but positively at higher latitudes. More specifically, Zelinka et al., 2012b showed that the ensemble mean change in cloud-fraction weighted $ln(\tau)$ per degree of global average surface air temperature warming was 0.03 K^{-1}, and the resulting longwave feedback per degree of warming was 0.22 $W\ m^2\ K^{-1}$. The result for shortwave feedback was $-0.14\ W\ m^2\ K^{-1}$. Correctly classifying cloud τ therefore plays a crucial role in the total cloud radiative feedback. Importantly, τ changes are the dominant cause of the negative net-feedback found in the Arctic (Zelinka et al., 2012b). Therefore, correctly classifying cloud optical thickness is crucial for narrowing down the magnitude of cloud feedback in the Arctic.

Cloud-phase can also play a large role in shortwave feedback. More specifically, liquid phase clouds tend to be optically thicker as they tend to have more numerous, smaller droplets compared to ice-phase clouds which tend to have fewer, larger particles. The liquid clouds therefore have larger scattering and reflectance properties, and so changes to the distribution of liquid clouds directly impacts the shortwave feedback (Murray et al., 2021).

We can separate the radiative impact of the phase of the cloud from the phase feedbacks themselves, which describe how changes to the cloud-phase distribution with surface warming changes the radiative properties of the atmosphere. Broadly, Tsushima et al. (2006) showed that replicating the inital distribution of cloud-phase in the mixed phase layer is particularly important for how the cloud-phase distribution changes with a doubling of CO_2. As discussed, cloud-phase has a direct impact on the radiative properties of the atmosphere. Tan et al. (2016) also discussed phase feedbacks for mixed-phase clouds highlighting that the doubling of CO_2 will cause a warming in the atmosphere causing isotherms (lines of constant temperature) to shift to higher altitudes compared to pre-doubling. At a constant altitude compared to pre-doubling the share of liquid phase particles in mixed-phase clouds could therefore increase, subsequently increasing the τ of the cloud. This would result in higher reflectivity and more shortwave radiation reflected back out to space, producing a negative feedback effect. Another example of a cloud-phase feedback was shown by Mitchell et al. (1989). They argued that since ice clouds precipitate more quickly than liquid clouds, a shift towards more liquid water coverage as atmospheric temperatures warm results in greater cloud amount. This in turn has a negative feedback effect as the increase in cloud amount reflects more shortwave radiation back out to space.

Given the importance of the cloud amount, CTP, τ, and cloud-phase distribution for the low-level cloud radiative feedback, correctly simulating their future evolution in climate models is crucial. Satellite observations allow for analysis on large spatial and temporal scales allowing for broader analysis on a variety of scales and variables. We can use these observations to search for emergent constraints that relate these variables and other meteorological observables. Emergent constraints describe empirical relationships between an observable (e.g. cloud fraction) of a current climate system simulation and the long-term projections of a different variable (e.g. the long-term feedback of cloud fraction) (Klein & Hall, 2015; Qu et al., 2018). For example, by finding a relationship between observations of cloud fraction and the long-term feedback of cloud fraction, we can use current observations of cloud fraction to restrict the range of values the feedback takes in future climate projections. More generally, through a better understanding of the relationships between meteorological observables (such as CTP, τ, cloud-phase distribution and low-level cloud amount) and their long-term feedbacks we can better evaluate the simulation of low-level clouds in models and their subsequent radiative response to climate warming in future projections.

In order to search for emergent constraints on the evolution of CTP, τ, cloud-phase distribution and cloud amount for low-level clouds, accurate long-term observations are needed for evaluation. The Moderate Resolution Imaging Spectroradiometer (MODIS) instrument is a passive imaging radiometer mounted onboard the National Aeronautic and Space Administration (NASA) Terra and Aqua satellites, which are polar orbiting satellites. This passive instrument records the outgoing radiation at the TOA for 36 wavelengths ranging from 620 $nm - 14.385$ μm in the infra-red and visible light spectrum emitted directly from the target (Platnick et al., 2018). It has the benefit of a large swath of 2330 km providing greater spatial coverage, and moreover provides a dataset that spans just over two-decades with the Aqua satellite having been launched in 2002. However, the accuracy of this passive instrument is known to be lower over sea-ice surfaces (Liu et al., 2010) since they have a similar surface albedo compared to that of low-level clouds and lack a significant thermal contrast with low-level clouds.

Unlike MODIS, the Cloud-Aerosol Lidar with Orthogonal Polarization (CALIOP) instrument is mounted onboard the Cloud-Aerosol Lidar and Infrared Pathfinder Satellite Observation (CALIPSO) and is a remote sensor that makes active measurements. CALIPSO has a circular low-earth sun-synchronous polar orbit at 705 km above sea level (Winker et al., 2006), meaning that the satellite always passes the same point on the Earth's surface at the same local time with a footprint of 90 m. Rather than passively measuring outgoing radiation it is a Light Detection and Ranging (lidar) instrument that measures the backscatter and depolarization of beams emitted at 1064 nm and 532 nm wavelengths, the latter of which is a linearly polarized beam

(Winker et al., 2006). This polarization allows for depolarization effects from back-scattering to be used to determine cloud-phase more accurately than MODIS (Hu et al., 2009). The lidar instrument also has the ability to provide a vertical cross-section of the structure of the atmosphere, breaking up readings into a 30/60 m vertical resolution depending on the altitude. However, its limitations include having smaller spatial coverage with a horizontal averaging resolution of 333 m, and so provides a smaller data-set when analysing variables across large geophysical scales (Winker et al., 2006). Moreover, while the CALIOP instrument is considered accurate for measuring τ for thin clouds the active beam attenuates quickly for larger ($\tau \geq 3-5$) τ units (Young et al., 2018).

While τ is an important fourth variable in governing Arctic Amplification (Tan et al., 2022), in this thesis we will be focusing on validating cloud-top-height (CTH), cloud amount and cloud-phase detection only for the MODIS instrument for regions with a latitude greater than 60 $^{\circ}N$. This is because of the lack of accurate τ retrievals or measurements available to validate MODIS τ retrievals against. The CALIOP instrument, which we will be using to evaluate CTH and cloud-phase, while possible to collocate with MODIS, attenuates quickly for thick clouds and ground-clutter (non-meteorological targets) can also interfere with the signal. Moreover, since we are evaluating Arctic clouds there are few ground and air-based observations of τ with which to compare (although King et al. (2004) and Eloranta and Ponsardin (2001) have made use of aircraft and ground-based instruments to measure Arctic τ previously). Hence, this thesis will focus on validating MODIS CTH and cloud-phase retrievals for low-lying clouds in the Arctic using CALIOP, where CTH is less than or equal to 2 km above the surface. We will be using the 2B-GEOPROF-LIDAR dataset, a combination of CALIOP and the CloudSat cloud profiling radar (Mace et al., 2007), to analyse cloud amount.

We will focus on single-layer clouds because as a passive instrument, MODIS measures the total atmospheric integrated radiance at the TOA and so MODIS cannot infer the vertical structure of cloud property readings, and hence does not give distinct retrievals for distinct cloud layers. Moreover, we will focus on Arctic polar-day because the MODIS passive instrument utilises bands lying in the visible spectrum as part of the optical property algorithm that retrieves cloud-phase, such as the visible (VIS)/near-infrared (NIR) and shortwave infrared (SWIR) channels (Platnick et al., 2018). Hence, these readings are not available in the polar-night (CTH is available however since it relies on the 11 μm brightness temperature (BT) as will be discussed in Section 4.2). We will therefore also be focusing this thesis on Arctic polar-day retrievals between March 1^{st} - September 30^{th} in 2015, where low-level clouds are common, occurring $80 - 90$ % of the time in the summer (Curry & Ebert, 1992; Shupe et al., 2011). More specifically, we will be analysing collection 6 (C6) which is the most recent update to the MODIS algorithm and contains key changes to its predecessor that have not been analysed in the Arctic, unlike collection 5 (C5) which has been analysed for the Arctic (Ackerman et al., 2008; Holz et al., 2008).

First, in Section 1.2 I will discuss key updates to the C6 algorithm and their expected impact on MODIS' retrieval mechanisms for the CTH, CloudMask, cloud-phase and τ. Despite not analysing τ retrievals directly, we will discuss changes to the τ retrieval mechanism since these are used in the cloud-phase retrieval mechanism (Platnick et al., 2018). Next, in Section 1.3 we will discuss the CALIOP retrieval algorithm for CTH and cloud-phase to be used as the ground truth. After, in Section 2 we will discuss our CTH hypotheses and then in Section 3 our methodology for analysing Arctic single-layer low-level clouds during the polar-day in 2015. This discussion can be broken up into two hypotheses for CTH, another analysis discussing the performance of the CloudMask algorithm for cloud fraction, and an analysis of the cloud-phase retrieval mechanisms. Then, in Section 4, I will discuss my results before discussing my conclusions and future work in Section 5.

1.2 MODIS Retrieval Algorithms and C6 Updates

1.2.1 Cloud Top Height

For low-clouds (CTP greater than 600 hPa) MODIS C6 retrieves CTP using the infrared-window approach (IRW) (Baum et al., 2012). MODIS measures the BT in the 11 μm channel ($BT_{11\ \mu m}$) (Channel 31 of the MODIS instrument) for a pixel with a cloud detected. The BT of an object is related to the measured emission $I(\lambda, T)$ and emissivity (ϵ) such that $I(\lambda, BT) = \epsilon I(\lambda, T)$, such that as ϵ increases so does BT. The C6 algorithm then differences this measurement with the clear-sky BT in the 11 μm channel, derived from the transmittance model called Pressure layer Fast Algorithm for Atmospheric Transmittances (PFAAST) (Hannon et al., 1996). This difference is then divided by the apparent $BT_{11\ \mu m}$ lapse rate (BTLR) pre-calculated from the following equation (Baum et al., 2012):

$$BTLR = \frac{BT_{11\ \mu m}(PFAAST) - BT_{11\ \mu m}(MODIS)}{CTH_{CALIOP}}. \tag{1.1}$$

Here, $BT_{11\ \mu m}(PFAAST)$, $BT_{11\ \mu m}(MODIS)$, CTH_{CALIOP} represent the modelled clear-sky $BT_{11\ \mu m}$ derived from atmospherically corrected surface temperatures using the PFAAST model, MODIS measured cloud-top $BT_{11\ \mu m}$ and CALIOP measured CTH, respectively. The CALIOP CTH is collocated with MODIS using the nearest great circle technique described by Holz et al. (2008) and in Section 3.2. This apparent BTLR is then averaged zonally and monthly to be used in the MODIS IRW algorithm. The 11 μm channel is within the atmospheric window. Since it has a high transmittance through the Earth's atmosphere it is useful for detecting low-lying features in the atmosphere since a large proportion of the radiation from lower levels will reach the TOA in this channel. This allows the passive instrument to detect radiation with this wavelength from atmospheric layers near to the Earth's surface, and so is useful for detecting low-level clouds.

The IRW retrieval method was adapted from the method used in C5 which compared measured $BT_{11\ \mu m}$ to a vertical profile of $BT_{11\ \mu m}$ values calculated utilising the PFAAST radiative transfer model which requires inputs from the gridded Global Data Assimilation System (GDAS) such as atmospheric temperature and water vapour profiles (Baum et al., 2012). Expressly, MODIS measures $BT_{11\ \mu m}$ for a pixel that detects a cloud according to the CloudMask mechanism (which will be discussed in more detail in Section 1.2.2) and compares the value to a modelled profile of $BT_{11\ \mu m}$ values to find the atmospheric layer that is dominating the TOA radiance. In the case of a tropospheric temperature inversion where the same $BT_{11\ \mu m}$ could exist at different pressure levels, the algorithm chooses the higher pressure value.

The C5 method struggled with a positive bias when a low-lying temperature inversion was present, common in marine locations and the Arctic. In particular, C5 was found to have a systematic bias (positive) of more than 2 km in comparison to CALIPSO according to Holz et al. (2008) in regions over open ocean where low-level temperature inversions are often found. Since the C6 method utilises the apparent BTLR in place of the C5 top-down approach to attempt to better estimate differences between surfaces and cloud-top temperatures, these overestimates were reduced. Baum et al. (2012) showed that the inclusion of the apparent BTLR reduced global positive overestimates of CTH in low-lying clouds between 60 $°N$ and 60 $°S$. While the new C6 method has yet to be compared to CALIOP in Arctic regions, the inclusion of apparent BTLR should have a significant impact in the Arctic where low-lying temperature inversions are particularly relevant.

1.2.2 MODIS CloudMask and Clear-Sky Restoral

A major update in C6 has been made to the CloudMask. The MODIS CloudMask algorithm produces a 48 bit output that gives information on cloud cover, tests used during cloud detection, and other relevant meteorological and surface factors. More specifically, bits 1–2 classify each pixel as either cloudy, uncertain clear, probably clear, and confident clear, which is determined from the individual spectral test results.

Previous papers show that CALIOP and MODIS C5 1 *km* products agree in identifying clear scenes in more than 85 % of cases (Ackerman et al., 2008; Holz et al., 2008). One important note is that C5 is clear-sky conservative due to how the CloudMask determines if a scene is cloudy or not. MODIS performs many tests, each of which produce a confidence level (F_i) that each pixel is cloudy between 0 and 1 inclusive, with 0 indicating a cloudy scene. The product of these tests (Q) determines the pixel classification such that a value of 0 also indicates a cloudy scene and there are Q thresholds between 0 and 1 that determine if the pixel is probably cloudy, probably clear, or clear. Hence, if any test detects a cloud the CloudMask will classify that pixel as cloudy since Q will equal 0. The CloudMask is therefore clear-sky conservative (Platnick et al., 2018). However, it is important to highlight that Holz et al. (2008) found in the Arctic winter period that the CloudMask is clear-sky biased in regions of high sea-ice. This is suggested to be due to higher surface albedos dominating the reflectivity functions measured by the sensor at the TOA, which is characteristic in the Arctic winter due to high sea-ice coverage.

Due to the clear-sky conservative nature of the CloudMask, C5 implemented a clear-sky restoral (CSR) logic which aimed to identify pixels that were likely to be poor retrieval candidates, such as broken cloud edges, in order to restore them to clear-sky based on several thresholds. Every pixel identified as cloudy passes through these tests and the CSR logic outputs whether these pixels are: overcast cloudy, not cloudy, partly cloudy, or a cloud edge based on multiple factors.

In C6, there were several changes to the CSR logic (Platnick et al., 2018):

- Unlike C5, cloudy pixels that were put through the logic and determined to be either partly cloudy and not cloudy scenes were restored to clear-sky values, in C6 only not cloudy scenes were restored to clear-sky. Partly cloudy pixels (PCL) were then stored in separate scientific data sets or retrieved failure metrics scientific data sets depending on whether or not optical and physical property retrievals were successful.

- The altitude indicator test, previously based on the tri-spectral IR thermodynamic (TIR) phase test, which as will be discussed later in Section 1.2.3 may falsely classify thin cirrus cloud edges as liquid water phase over warm surfaces, now uses the IRW and CO_2 slicing methods to determine cloud top altitude allowing thin cirrus clouds to be more accurately handled.

However, several problems still remain. Thin cirrus clouds are still failing to be detected by the CSR algorithm in C6, and broken cloud edges may still be classified as clear-sky or vice-versa. However, overall as discussed by Platnick et al. (2018), the C6 CloudMask is still generally clear-sky conservative.

1.2.3 Cloud-Phase

The MODIS phase retrieval algorithm differs in daytime and nighttime. In nighttime retrievals only the TIR phase retrieval is used, which has been significantly updated in C6. In C6, the TIR retrieval utilises a new method including logarithmic cloud emissivity ratios in three pairs of bands, aiming to reduce the influence of the radiation emitted by the surface. The ratio (known as the β ratio) can be derived from the equation for the radiance at the TOA, which is approximated (Menzel et al., 2015):

$$I = (1-\epsilon)[I_{clr} - I_{ac}] + I_{ac} + T_{ac}\epsilon B(T_{eff}) \tag{1.2}$$

where I is the TOA radiance measured by MODIS, I_{clr} the clear-sky TOA radiance, I_{ac}

is the radiance contribution from the above-cloud atmospheric layer, T_{ac} is the above-cloud transmittance, and $B(T_{eff})$ is the blackbody radiation at the effective temperature (T_{eff}) of the cloud derived from the pressure profiles used in the PFAAST model (Menzel et al., 2015). The impact of the surface radiance on the measured TOA radiance is taken into account through the difference of the measured intensity I and the PFAAST calculated clear-sky intensity I_{clr}. Rearranging Eqn. 1.2 leads to an equation for emissivity of:

$$\epsilon = \frac{(I - I_{clr})}{[I_{ac} + T_{ac}B(T_{eff}) - I_{clr}]}. \tag{1.3}$$

Using Eqn. 1.3 ϵ values may be calculated from measured I values and B values derived from Planck's law assuming that cloud-top $BT = T_{eff}$ (Pavolonis, 2010). Utilising the Parol et al. (1991) β parameter the measured emissivities of two bands (x,y) may be related logarithmically:

$$\beta_{y,x} = \frac{\ln[1 - \epsilon_y]}{\ln[1 - \epsilon_x]}. \tag{1.4}$$

The specific use of the beta parameter and the bands used depend on various thresholds and importantly the underlying surface type (a description of which can be found in Platnick et al. (2018)); however, the benefit is that it allows the impact of the surface radiance to be taken into account and therefore the influence of the surface is decreased in comparison to the C5 technique, which just relied on the BT differences. In application, the inclusion of the emissivity ratio in C6 uses three particular band combinations (7.3 $\mu m/11$ μm, 11 $\mu m/12$ μm and 8.5 $\mu m/11$ μm) in conjunction with BT differences (Menzel et al., 2015), applying thresholds to determine phase that vary based on surface type.

According to the literature, these changes to the TIR method show improved results for broken clouds and optically thin ice clouds (previously mis-classified as liquid phase). However, the phase success rate when compared to CALIOP still struggles with optically thin clouds, and while false ice phase discrimination is rarer in low maritime broken liquid cloud scenes, it still remains a problem for the algorithm (Platnick et al., 2018). The emissivity ratios also do not seem to greatly improve liquid phase classification according to Platnick et al. (2018), but many of these pixels are now classified as uncertain in C6. Importantly we do expect the influence of surface type to be smaller in C6 due to the inclusion of the beta parameter.

In the daytime (and therefore Arctic polar-day), the C6 cloud-phase tests can be broken up into four categories, the Cloud Top Temperature (CTT) test, the TIR phase test, and two SWIR based test (Platnick et al., 2018):

- Cloud top temperature tests: Utilising MOD06 1 km CTT retrievals, where C5 warm cloud sanity checks that force phase to liquid for $CTT > 270\ K$ were retained when liquid $\tau > 2$.

- TIR phase test: Previously based on the analysis of 8.5 μm and 11 μm BTs, the algorithm was improved by using cloud emissivity ratios (Heidinger & Pavolonis, 2009; Pavolonis, 2010) that account for clear-sky radiance to reduce the influence of the surface emissivity to address one limitation: optically thin cirrus clouds failed to be classed as ice phase. However, this improvement has little impact of addressing the C5 limitation: super-cooled water or mixed-phase cloud identification problems (Baum et al., 2012).

- 1.38 μm test: This test separates high-altitude ice clouds from low-altitude liquid clouds using the 1.38 μm high cloud flag from the MOD35 CloudMask product. It utilises strong water vapour absorption at 1.38 μm effective over snow- and ice-covered surfaces in the Arctic (Gao et al., 1993) and is only applied when sufficient water vapour is present. This vapour band detects little radiance reflected from low-level clouds compared to higher cirrus clouds as it is quickly absorbed by water vapour in its atmospheric path (Platnick et al., 2018).

- Spectral cloud effective radii tests: Replacing the C5 SWIR/NIR reflectance ratio tests with three SWIR wavelength τ and effective radius (r_e) retrievals. As previously discussed in Section 1.1, cloud-phase and τ are strongly related, so succesful τ and r_e retrievals provide information on the phase of the cloud. Three wavelengths are used to reduce the ambiguous phase overlap regions.

In C6 rather than using a linear sequence of tests as in C5, when MODIS performs each of these four separate phase tests each produces a weighted phase vote which combined lead to the Optical Properties (OP) phase retrieval. Hence, in daytime MODIS produces both the TIR phase product (the result of only the TIR method) and the OP method (the result of all four tests). These assigns a cloud as either liquid, ice, mixed phase, or unknown, and are only implemented given a pixel is classified as cloudy by the CloudMask product and the 8.5 μm and 11 μm BTs are available (Menzel et al., 2015). This method was implemented in order to provide better adaptation to different cloud scenes, as the weight of the vote is a measure of each test's certainty. It has been shown (Platnick et al., 2018) that the phase agreement fraction between CALIOP v3 Cloud Layer product and MODIS C6 has improved to 92 % compared to 83 % for the C5 product where CALIOP detected a single phase, in particular the greatest improvement is seen for opaque ($\tau > 3$) clouds over permanent snow/ice surfaces such as Greenland. In this paper, we will be analyzing the TIR retrieval and comparing it to the OP phase retrieval. Since the OP test takes into account three additional more stringent tests, which will not be evaluated directly, we expect the OP phase retrieval to be more accurate and adaptable to different cloud scenes than the TIR method on its own.

1.2.4 Cloud Optical Depth

While we will not be analysing τ directly, its retrieval plays an important and direct role in MODIS cloud-phase retrievals which we will be using to analyse the cloud detection success rate against CALIOP. Microphysical cloud property retrievals, such as τ and r_e, are obtained by MODIS using two techniques. The first utilises a forward radiative transfer model to pre-compute look-up-tables (LUTs) to compare to simultaneous measurements of the reflectance functions in two spectral channels that are not absorbed (VIS/NIR) and absorbed (SWIR) by water vapour.

A forward radiative transfer model is one that calculates TOA radiative fluxes from known inputs such as scattering properties. MODIS uses a model which assumes a horizontally homogeneous atmosphere with radiation that obeys Lambert's law of reflection, where the radiant intensity observed reflecting from a surface is directly proportional to the cosine of the angle between the incident radiation and the surface normal. It is important to distinguish conservative and non-conservative scattering respectively, where conservative scattering means that all incident radiant energy is not converted into other forms of energy (non-conservative scattering is more realistic when dealing with optically thicker atmospheric layers). Importantly, the reflectivity function (R) governing non-conservative scattering (as described by King (1987)) is dependent on both τ and r_e. This is illustrated by Fig. 1.1 from Nakajima and King (1990), which shows the relationship between two reflectivity functions for various τ and r_e values. I highlight that R is also a function of the cosine of the solar zenith angle (μ_0), the absolute value of the cosine of the solar zenith angle (μ), and the relative azimuth angle between the incident and emerging radiation (ϕ), and crucially of cloud-phase as well.

Pre-computed LUT values for R like those seen in Fig. 1.1 are calculated for each τ

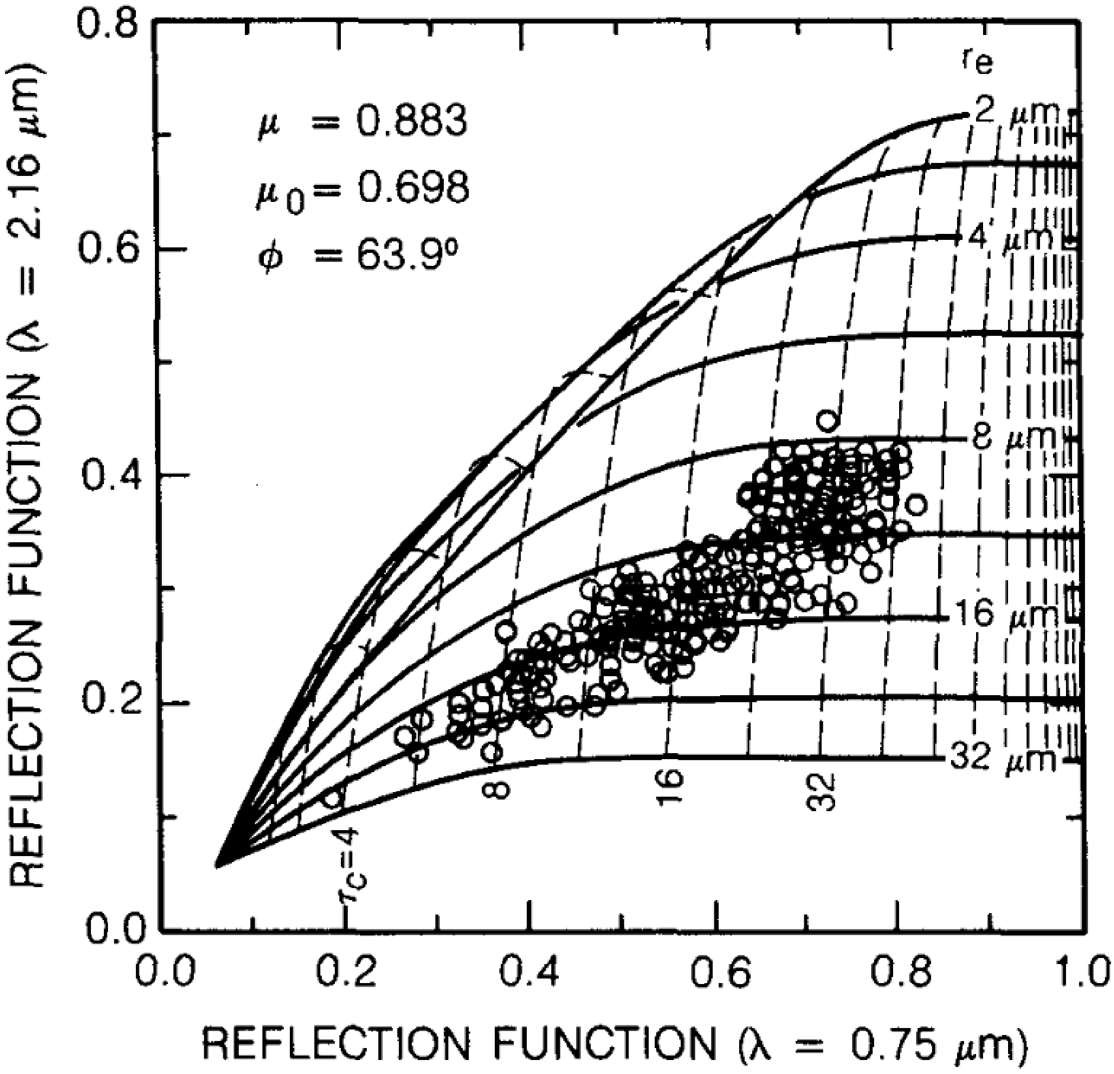

FIGURE 1.1: Theoretical relationship between reflectivity functions at two wavelengths for various values of τ and r_e, with data from the First International Satellite Cloud Climatology Project Regional Experiment superimposed on top. Figure reproduced from Nakajima and King (1990). Published 1990 by the American Meteorological Society.

and r_e value, which are then compared to MODIS reflectance measurements to determine the most viable τ and r_e values. MODIS measures reflectance data is equivalent to radiance data, related to measured radiance (I) such that (Barnes et al., 2019):

$$R = I/F_0 \tag{1.5}$$

where F_0 is the mean extraterrestial solar irradiance (a constant for a give wavelength but dependent on solar zenith angle). MODIS utilises two channels in the VIS and SWIR spectral regions since for any given reflectance measurement in one channel multiple τ and r_e values are possible, however utilising two channels constrains the possible τ and r_e values to one possible value (Platnick et al., 2018). This is known as the bi-spectral approach.

While this approach has been validated with comparisons to airborne data in Nakajima and King (1990), they showed that the greatest sensitivity of R occurs when the underlying surface albedo is small, which is a problem in high sea-ice regions where surface albedo is high. Hence, a second supplementary method was put forward by (Platnick et al., 2018) in C6. Over regions of snow and ice MODIS only utilises channels 2.13 μm and 1.6 μm. This is because surface albedo, which varies depending on the channel used, was low over snow and sea-ice for these channels (Moody et al., 2007) . Hence, the accuracy of τ and r_e retrievals from the LUTs was improved in C6 over snow and ice surfaces.

Moreover, another improvement in C6 is the separation of the τ (cloud optical thickness, COT) (and r_e) retrievals in the 1.6 μm (COT16), 2.1 μm (COT21), and 3.7 μm (COT37) channels. Due to the sometimes largely differing failure patterns of the three channels (Cho et al., 2015) where the reflectance observations may lie outside of the τ-r_e LUT solution space, there can be significantly different pixel populations of τ and r_e for each channel. In C5, the retrievals from 1.6 μm and 3.7 μm channels are reported as differences from the 2.1 μm channel and hence coupled to the latter channel (Platnick et al., 2018). So, when the latter channel failed to retrieve data so did the former. Separating the retrievals ensured that the 1.6 μm and 3.7 μm channels do not necessarily fail when the 2.1 μm channel fails. Therefore, we expect less failed τ retrievals in the C6 pixel population since the coupling has been removed. In particular, this is important for broken liquid water cloud-phase retrievals, often on the edge of cloud distributions such that the heterogeneity scales are on an order of less than 1 km (for the nadir pixels) (Lebsock et al., 2011; Zhang et al., 2012), where the

2.1 μm channel fails often.

1.3 CALIOP Retrieval Algorithms

1.3.1 Cloud Top Height

CALIOP retrieves CTH through the Feature Finding algorithm (Vaughan et al., 2005; Winker et al., 2006). CALIOP measures the attenuated backscatter coefficient from a beam directed towards the surface of the Earth at a wavelength of 532 nm. The beams interact with particles and molecules in the atmosphere and CALIOP measures the strength of the backscatter from these interactions and then determines the backscatter coefficient. The backscatter coefficient is a measure of the reflective strength of a target and contains information about the molecular composition of the target. From here it calculates the attenuated scattering ratio, which is equal to the measured attenuated backscatter coefficient divided by the modelled clear-sky attenuated backscatter coefficient. Clear-sky backscatter coefficients are constructed from molecular and ozone number density profiles derived from meteorological data produced by the NASA's Global Modeling and Assimilation Office (Vaughan et al., 2005). The attenuated scattering ratio is used to mitigate the effects of background noise as it takes into account a clear-sky modelled backscatter coefficient. The normalization by the clear-sky modelled attenuated backscatter coefficient is such that the ratio is close to one when no backscattering feature is present. In contrast, a spike in the attenuated scattering region is seen whenever a feature, such as a cloud or aerosol layer, is detected.

In order to qualify as a feature rather than insignificant noise the attenuated scattering ratios must rise above the local predefined threshold level for a number of consecutive points that exceed the minimum feature distance, which is a measure of the vertical length of the feature. The threshold for the minimum feature distance was determined from the expected geometric depths of features within the vertical region (Vaughan et al., 2005). This retrieval method allows CALIOP to retrieve the height of multiple features throughout the vertical profile of the atmosphere.

1.3.2 Cloud-Phase

In order to determine cloud-phase, CALIOP utilises a combination of the layer integrated attenuated backscatter and the linear depolarization ratio. The 532 nm channel is used because it is linearly depolarized by cloud features, whereas the 1064 nm channel is not.

The lidar beam, when transmitted towards the cloud, is nearly fully linearly polarized, meaning that the oscillation of the electromagnetic waves is confined to a single plane. The depolarization ratio of backscatter (δ) by cloud particles is the ratio of the cross-polarization and the co-polarization component. Past studies (Sassen, 1991) have shown that single-scattering of this transmitted signal from ice crystals results in a measurable signal in the plane perpendicular to the original polarization plane. The magnitude of this depolarization depends on the habit of the ice crystals, but is usually in the range of 30 % $-$ 50 % (Liu et al., 2005). Lower values have been shown for horizontal orientated ice crystals (Sassen & Benson, 2001). In contrast, spherical water droplets do not produce a measurable signal in the cross-polarization component for single-scattering, and so δ is zero since no depolarization occurs (Hu et al., 2009). In this way, δ is dependent on the phase of the cloud.

Importantly, studies have also shown that optically thicker liquid clouds can give rise to multiple scattering which can result in linear depolarization (Liu et al., 2005). Hence, for liquid clouds δ increases with the τ of the cloud. Moreover, as highlighted by Cho et al. (2008) the layer integrated attenuated backscatter is proportional to the τ of the cloud. Therefore δ for liquid clouds increases with increasing layer integrated attenuated backscatter. More generally, Hu et al. (2001) showed that the depolarization threshold values for the phase of the cloud were a function of the layer-integrated backscatter.

Fig. 1.2 shows the thresholds used by CALIOP to determine the phase of a cloud (Hu et al., 2009). As can be seen, clouds dominated by water droplets (denoted as "water phase" from now on) fall close to the black line, which describes the theoretical relationship derived by (Hu, 2007). CALIOP uses these thresholds to distinguish the phase of the cloud by measuring both the linear depolarization ratio and layer integrated attenuated backscatter.

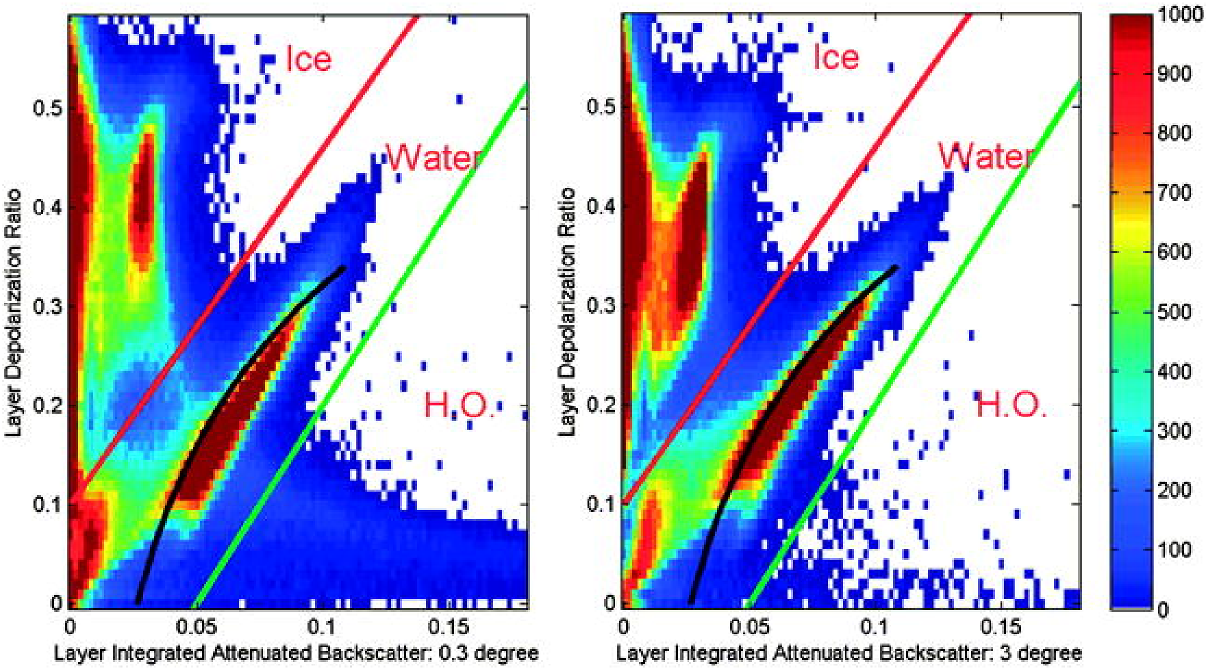

FIGURE 1.2: Density plot showing the frequency of occurrence as a function of depolarization ratio and layer-integrated attenuated backscatter reproduced from Hu et al. (2009) The left figure shows data from January 2007 and the right January 2008. The red line shows the threshold for ice-phase cloud, the threshold for distinguishing layers dominated by liquid water droplets and layers containing horizontally orientated ice crystals is shown in green. ©American Meteorological Society. Used with permission.

Chapter 2

Cloud Top Height Hypotheses

2.1 Hypothesis 1 – Quantification of Biases Arising from Lower-Tropospheric-Stability

Hypothesis 1 states that lower-tropospheric-stability (LTS) plays a role in the strength and sign of the MODIS CTH biases in the presence of low-level ($CTH \leq 2\ km$) single-layer clouds, where the τ of the cloud is small and the influence of the surface is large. This hypothesis only applies to low-level clouds since this bias is applicable when MODIS utilises the IRW CTH retrieval technique rather than the CO_2-slicing technique, which occurs for clouds residing at a pressure altitude smaller than 600 hPa (Platnick et al., 2018).

The MODIS IRW CTH technique struggles in the case of low τ due to the influence of the underlying surface on the TOA measured radiance for a wavelength of 11 μm. Ideally, MODIS would measure the radiance emitted directly from the cloud-top to determine the cloud-top BT. However, as a passive instrument it measures the total vertically integrated radiance at the TOA. Since the atmosphere and surface of the Earth consist of many layers of absorbers and emitters, this TOA radiance is a combination of radiance emitted from all these layers. Hence, the retrieved BT will come from a superposition of radiation emitted from the surface of the Earth and every atmospheric layer between the surface and the TOA. As the 11 μm channel is an atmospheric window channel, we expect most atmospheric layers without a cloud present to be relatively (but not completely) transparent; however, the surface of the Earth can emit strongly in this channel. We therefore expect the MODIS retrieved BT to sit somewhere between the surface-level temperature at 11 μm, which is directly related to the surface and near-surface air temperature, and the temperature of the cloud-top.

The effect of this BT bias on the CTH bias can be understood through analysis of the following CTH equation used in MODIS' algorithm (Menzel et al., 2008):

$$CTH = \frac{BT_{11\ \mu m}(\text{PFAAST}) - BT_{11\ \mu m}(\text{MODIS})}{BTLR}. \tag{2.1}$$

Since the detected radiance at the TOA is a combination of the surface radiance and the cloud-top radiance, particularly for small τ values, the MODIS measured $BT_{11\ \mu m}(\text{MODIS})$ will sit somewhere between the surface BT (represented in Eqn. 2.1 by the modelled $BT_{11\ \mu m}(\text{PFAAST})$) and the actual cloud-top BT. Using Eqn. 2.1, since $BT_{11\ \mu m}(\text{MODIS})$ will take a value closer in magnitude to $BT_{11\ \mu m}(\text{PFAAST})$, the modelled clear-sky BT, the numerator in Eqn. 2.1 will be smaller than the physical BT difference between the cloud-top and the surface, and hence CTH underestimated.

More specifically the impact of the surface will be stronger when the cloud is optically thin. When τ is low the TOA outgoing radiation detected by the passive sensor is heavily influenced by the surface underlying the low-lying clouds, since the emitted radiation from the surface attenuates very little while passing through the cloud-layer. In contrast, when the cloud is optically thick, the surface radiation attenuates more before reaching the TOA according to the equation $I_{\text{out}} = I_{\text{in}}e^{-\tau}$ (Bodhaine et al., 1999), where I_{in} is the radiation incident to the cloud and I_{out} the radiation leaving the cloud after attenuating. Hence, when τ is small the impact of the surface radiation is stronger and therefore the measured BT will be closer to the surface BT rather than the targeted actual cloud-top BT.

More generally, we also expect that the CTH underestimation will be larger when the influence of the surface is larger. The stronger the radiation emitted from the surface in the 11 μm wavelength is, the stronger the influence of the surface on the TOA radiance is. According to Planck's law the strength of emission for a particular wavelength is governed by (Chandrasekhar, 1960):

$$I(\lambda, T) = \frac{c_1}{\lambda^5 [e^{c_2/\lambda T} - 1]}, \tag{2.2}$$

where λ is the relevant wavelength, T is the temperature of the object, $c_1 = 2hc^2$ where c is the speed of light (equal to $299,792,458$ ms^{-1}) and h is the Planck constant ($\sim 6.63 \times 10^{-34}$ $J\ Hz^{-1}$), and $c_2 = \frac{hc}{k_B}$ where k_B is the Boltzmann constant ($\sim 1.38 \times 10^{-23}$ $J\ K^{-1}$). According to Eqn. 2.2, the radiance emitted by an object increases with the temperature of the object, for classical black or grey objects. Since temperature plays a crucial role in the emission strength of an object in Planck's law, we hypothesize CTH biases to be closely tied to the temperature structure between the surface and cloud itself. More specifically we expect the bias to be largest when the temperature of the surface is higher and the temperature of the cloud lower since in this case the radiation emitted by the surface is more intense relative to the radiation emitted by the cloud according to Eqn. 2.2. Importantly, the radiation emitted from the surface may not dominate at the TOA in this example, it will just play a larger role.

We can use the metric LTS as an indicator of the potential temperature structure of the atmosphere, where the 800 hPa LTS was chosen as it is close to the upper 2 km CTH boundary used throughout this thesis. The 800 hPa LTS is defined by the equation

(Slingo, 1987; Wood & Bretherton, 2006):

$$LTS = \theta_{800\ hPa} - \theta_{2\ m} \tag{2.3}$$

where $\theta_{800\ hPa}$ and $\theta_{2\ m}$ are the potential temperatures of 800 hPa and 2 m above the surface respectively. When LTS is equal to 0 K, the lower troposphere is dry neutral (which means conditionally unstable) in terms of static stability. In contrast, a negative LTS would indicate absolutely unstable conditions, which would trigger spontaneous overturning of the air layer, restoring at least dry neutral stability. Therefore, a negative LTS is expected to only occur rarely and for short time periods.

When LTS is high, $\theta_{800\ hPa}$ is much larger than $\theta_{2\ m}$. This generally indicates a high level of stability and the presence of a low-lying temperature inversion (Wood & Bretherton, 2006), which is particularly common in the Arctic in the winter over regions of high sea-ice concentration. In thermal wavelengths there is a continuous loss of heat from the surface of sea-ice through radiant emission, lowering surface temperatures and causing low-lying temperature inversions (Stramler et al., 2011; Uttal et al., 2002). However, when LTS is low this indicates the lack of or a weaker and elevated temperature inversion, usually occurring when the temperature of the surface is higher than the CTT, and is generally favoured in summer and autumn (Graversen & Wang, 2009).

Importantly, note that when LTS is relatively small, $\theta_{2\ m}$ has a more comparable magnitude to $\theta_{800\ hPa}$. Since $\theta_x = T_x \times (\frac{P_0}{P_x})^k$, where x is the pressure level of θ, k is the ratio of R and the specific heat capacity at a constant pressure, equal to 0.286, and P_0 is the reference pressure level equal to 1000 hPa, low LTS indicates that either $P_{2\ m}$ is relatively small, $T_{2\ m}$ is relatively large or that $T_{800\ hPa}$ is relatively small. In the case that $T_{2\ m}$ is larger we can hypothesize that the relative intensity of the radiation emitted from the Arctic surface is larger than if $T_{2\ m}$ were smaller due to Eqn. 2.2, assuming that $T_{2\ m}$ is an indicator of surface temperature. Alternatively, in the case that $T_{800\ hPa}$ is relatively small, the intensity of the radiation emitted from the cloud-top is reduced, if we assume $T_{800\ hPa}$ is an indicator of cloud-top temperature. Hence, the cloud-top emitted radiation would play less of a dominating role at the TOA and the relative influence of the surface would be larger than when $T_{800\ hPa}$ is relatively large.

In both cases, the influence of the surface on the measured $BT_{11\ \mu m}$(MODIS) is large, and so we hypothesize that the magnitude of the underestimation of CTH is greatest when LTS is lower. It is important to highlight again that the impact of the surface emission would be relatively smaller as τ gets larger since the radiation would attenuate more as it passes through the cloud, as previously discussed. Hence, we expect the surface radiance to only play a large role in the determination of the cloud-top BT when the cloud is optically thin.

Moreover, the impact of the surface radiance on the CTH bias could be mitigated since the calculation of apparent BTLR and CTH use the same simplified physics. For instance, if the actual BTLR was conserved between the pre-calculated monthly and zonal BTLR values (using Eqn. 1.1) and the calculation of CTH using Eqn. 2.1, which could be achieved if the cloud-top temperature and surface temperature co-varied similarly between the two calculations, the validity of the CTH estimate would be good. More specifically, since both equations rely directly on $BT_{11\ \mu m}$(MODIS) retrievals, any errors due to influence of the surface on the TOA radiation used to determine cloud-top BT would be accounted for by the apparent BTLR. Therefore, the consistency of the approach between Eqn. 1.1 and Eqn. 2.1 could justify this CTH retrieval method. However, problems could occur if there was any inconsistency in the atmospheric or surface conditions between the calculation of the zonally and monthly averaged apparent BTLR using Eqn. 1.1m and the calculation of CTH using

Eqn. 2.1. For example, if the cloud was near-black (opaque) in the 11 μm wavelength range during the calculation of BTLR, yet not black in the calculation of CTH, the impact of the surface previously discussed could cause a CTH bias. In this case, since the surface radiation would attenuate more as it passed through the optically near-black cloud during the calculation of Eqn. 1.1, the influence of the surface would not impact the MODIS cloud-top retrieved BT used in the calculation of the apparent BTLR, and hence not taken into account by use of the apparent BTLR in the calculation of CTH using Eqn. 2.1. Therefore, while the impact of LTS does not necessarily invalidate the C6 CTH retrieval method, we hypothesize that it will lead to a CTH bias.

In summary, we hypothesize that the size of the CTH underestimation compared to CALIOP is largest when τ is small and LTS is low, however it is possible that other causes could influence the CTH bias, and analysis and discussion of these, along with Hypothesis 1, will be presented in Section 4.2.

2.2 Hypothesis 2 – Importance of Surface Type Emissivity

MODIS makes two simplifying assumptions in its computation of CTH. First, it assumes that the underlying sea-ice fractional coverage is 0 % in its computation of the clear-sky $BT_{11\ \mu m}(\text{PFAAST})$ (Hannon et al., 1996; Strow et al., 2003). Second, MODIS uses zonal and monthly averages of the apparent BTLR in Eq. 1.1 (Baum et al., 2012). These two assumptions directly affect MODIS CTH calculations. More specifically, $BT_{11\ \mu m}(\text{PFAAST})$ is directly used to calculate CTH and the apparent BTLR, so inaccurately classifying the underlying surface emissivity by assuming sea-ice fractional cover is 0 % directly impacts CTH. Moreover, using monthly zonal averages of the BTLRs in Eqn. 2.1, also assuming sea-ice fractional cover is 0 %, neglects longitudinally varying surface emissivity differences. Both these assumptions are unphysical in the Arctic, as large parts of the Arctic ocean are covered in sea-ice and we expect the apparent BTLR to vary longitudinally.

The impact of these assumptions can be understood by understanding how emissivity affects emitted radiance and how BT is derived. Emissivity is the ratio between the energy emitted from a materials surface to that of a perfect emitter (or blackbody), and is wavelength-dependent for real surface types. A higher emissivity value means that the radiance emitted is stronger and closer to that emitted by a blackbody emitter at the same temperature. On the other hand, BT is the temperature a blackbody object would have to emit radiation at the strength measured. According to Planck's law the strength of emission for a particular wavelength is governed by Eqn. 2.2. BT can be expressed in place of the regular temperature (T) in Planck's law, as the equivalent blackbody emission of an object is related to the measured emission $I(\lambda, T)$ such that $I(\lambda, BT) = \epsilon I(\lambda, T)$. Hence a higher ϵ means that a higher BT is derived. Therefore, inaccurate surface emissivity values lead to inaccurate modelling of $BT_{11\ \mu m}(\text{PFAAST})$.

More specifically, assuming 0 % sea-ice fractional cover will raise the modelled $BT_{11\ \mu m}(\text{PFAAST})$. This is because open-ocean has a higher emissivity than ice, approximately 2 % higher in the 11 μm wavelength ($\sim$ 909 cm^{-1} wavenumber), as can be seen in Fig. 2.1. Hence, the modelled TOA clear-sky radiance will be stronger when MODIS assumes 0 % fractional cover than when physically accurate sea-ice cover is used for cloudy pixels that sit over ice-covered surfaces. Therefore, the modelled $BT_{11\ \mu m}(\text{PFAAST})$ is overestimated. Hence the magnitude of the numerator in Eqn. 2.1 would be overestimated or underestimated depending on whether an inversion was present.

The dependence on whether or not an inversion is present can be seen by noting that in the case of a low-level temperature inversion, $BT_{11\ \mu m}(\text{PFAAST}) <$

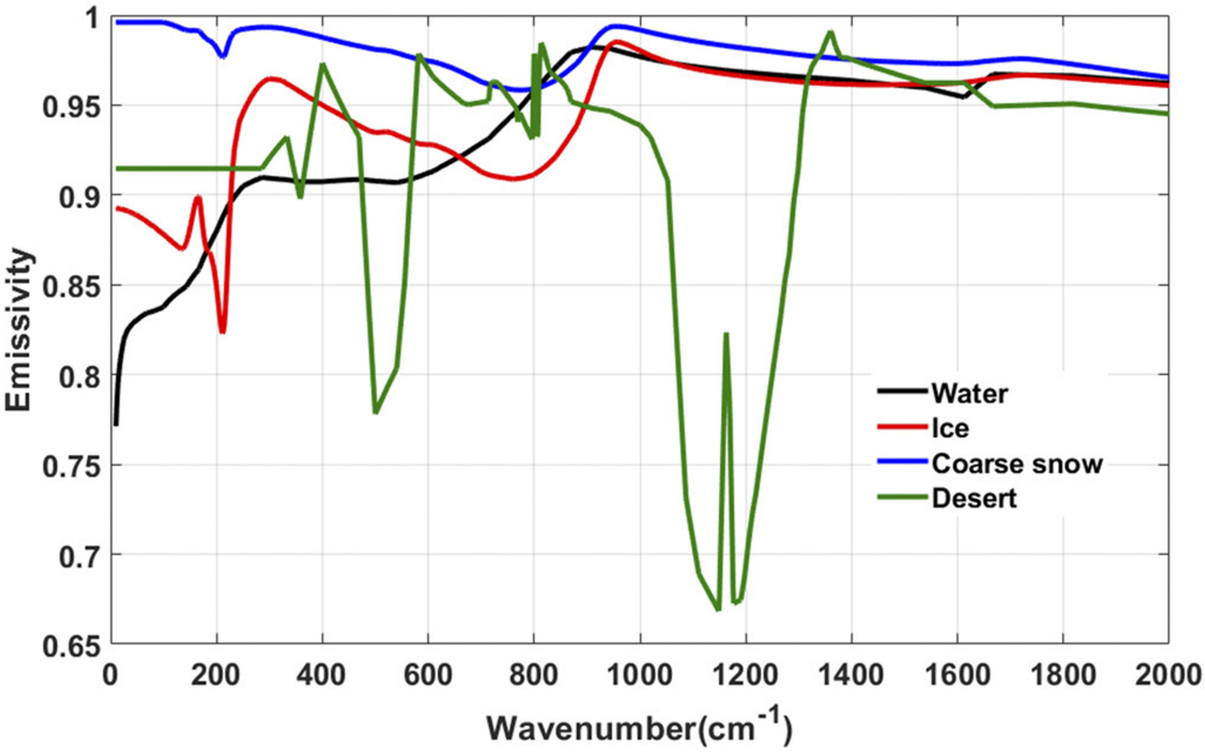

FIGURE 2.1: Surface emissivity by wavenumber broken into water, ice, snow, and desert surface types. Figure reproduced from Huang et al. (2018). ©American Meteorological Society. Used with permission.

$BT_{11\ \mu m}$(MODIS), since temperature increases with altitude in that situation. Therefore using unrealistic 0 % sea-ice fractional cover and hence raising $BT_{11\ \mu m}$(PFAAST) will lead to an smaller numerator in Eqn. 2.1 than if realistic sea-ice fractional cover values were used. When an inversion is not present and $BT_{11\ \mu m}(\text{PFAAST}) > BT_{11\ \mu m}(\text{MODIS})$, the overestimate in $BT_{11\ \mu m}$(PFAAST) when unrealistic 0 % sea-ice fractional cover is used leads to an overestimate in the numerator in Eqn. 2.1 compared to the case when realistic sea-ice fractional cover values were used. In general, in polar-day conditions a low-level temperature inversion is less common or generally weaker and raised in altitude (Graversen & Wang, 2009), so we expect using realistic sea-ice fractional cover in the calculation of clear-sky BT to lead to an average reduction in CTH; although the magnitude of this effect may be small, yet needs to be quantified. It should be noted that it is also possible that $BT_{11\ \mu m}(\text{PFAAST}) < BT_{11\ \mu m}(\text{MODIS})$ occurs because of inconsistency between the PFAAST model and the actual atmospheric profile influencing the retrieved cloud-top BT. For example, errors in PFAAST simulated surface temperature could be particularly relevant for pixels with a small vertical temperature gradient, such that the actual surface and cloud-top BTs are close in magnitude. Hence, a small error in the PFAAST surface temperature could result in the modelled surface BT being smaller than the measured cloud-top BT. In this case, the use of realistic sea-ice values would lead to a larger numerator, even though no temperature inversion is present, since the PFAAST model is simulating the BT as larger than the measured cloud-top BT.

It is worth noting that the new C6 method using the apparent BTLR showed some improvement relative to C5 for CTH biases in comparisons to CALIOP, with the retrieval bias for August 2006 reducing to less than 0.5 *km* (Baum et al., 2012). However, a full comparison of CTH for polar-day single-layer low-level clouds in the Arctic for the C6 algorithm has not yet been performed. In particular, the Arctic is a challenging landscape since sea-ice covers much of the ocean, and has a low thermal contrast with low-lying clouds in the thermal-infrared.

Given the relatively small differences in surface emissivity between water and sea-ice, it is possible that the impact of correctly assigning surface emissivity in the PFAAST model on both the CTH (Eqn. 2.1) and BTLR (Eqn. 1.1) MODIS calculations is small, and therefore that these calculations are impacted by influences other than surface emissivity changes. Analysis and discussion of these, along with analysis of Hypothesis 2, will be presented in Section 4.3. Hypothesis 1 and 2 simply motivate the initial analysis of the dataset and might point to other sources of uncertainty in the MODIS CTH determination.

Chapter 3

Methodology

3.1 Structure of Satellite Data

MODIS satellite data can generally be split into five product levels. Level 0 is raw satellite feeds with no processing, Level 1 come from radiometrically calibrating the Level 0 data to calculate physical properties such as spectral radiance allowing satellite data to be compared (Price, 1987). This data can generally be broken up into different geometric resolutions, in the case of MODIS 1 km, 500 m, 250 m resolutions as measured at the surface level. Level 2 data is atmospherically corrected Level 1 data yielding surface reflectance products (Roger et al., 2015), taking into account scattering or absorption effects in each of the spectral bands. Level 3 data has been temporally averaged or composited and has been gridded onto a map projection. Finally, Level 4 data, usually saved for data assimilation products, has been additionally processed.

Throughout this thesis I will be using data obtained during the 2015 polar-day to analyse the validity of the cloud property retrieval algorithm. MODIS data can be split into different collections, which differ in the algorithm specifics used to obtain Level 2 atmospheric properties from Level 1 data. This paper will focus on C6 reprocessed from C5 to improve calibration, upstream products and algorithm refinements (Roger et al., 2015). More specifically, the satellite data we are using is described in Table 3.1, and the reanalysis data is described in Table 3.2.

TABLE 3.1: Listing of MODIS and CALIOP dataset versions and specific variables used in this work. Latitude and longitude coordinates are geodetic.

Reference Name	Full Variable Name; Processing Level; Version Number; Spatial Resolution; Product Name; Reference
MODIS CTH	Cloud_top_height_1km; Level 2; Collection 6.1; 1 km ; MYD06; Platnick et al., 2015
MODIS TIR cloud-phase	Cloud_Phase_Infrared_1km; Level 2; Collection 6.1; 1 km; MYD06; Platnick et al., 2015
MODIS OP cloud-phase	Cloud_Phase_Optical_Properties; Level 2; Collection 6.1 1 km; MYD06; Platnick et al., 2015
MODIS COT21	Cloud_Optical_Thickness; Level 2; Collection 6.1; 1 km; MYD06; Platnick et al., 2015
MODIS multi-layer flag	Cloud_Multi_Layer_Flag; Level 2; Collection 6.1; 1 km; MYD06; Platnick et al., 2015
MODIS $BT_{11\ \mu m}$	Band 31; Level 1B; Collection 6.1; 1 km; MYD02; MODIS Characterization Support Team, 2017a
MODIS latitude	Latitude; Level 1A; Collection 6.1; 1 km; MYD03; MODIS Characterization Support Team, 2017b
MODIS longitude	Longitude; Level 1A; Collection 6.1; 1 km; MYD03; MODIS Characterization Support Team, 2017b
CALIOP CTH	Layer_Top_Altitude; Level 2; V4.20; 1 km; Lidar Level 2 Cloud, Aerosol, and Merged Layer V4.20 Products; Winker et al., 2023
CALIOP cloud-phase	Feature_Classification_Flags; Level 2; V4.20; 1 km; Lidar Level 2 Cloud, Aerosol, and Merged Layer V4.20 Products ; Winker et al., 2023
CALIOP 523 nm τ	Column_Optical_Depth_Cloud_532; Level 2; V4.20; 5 km; Lidar Level 2 Cloud, Aerosol, and Merged Layer V4.20 ; Winker et al., 2023
CALIOP latitude	Latitude; Level 2; V4.20; 1 km; Lidar Level 2 Cloud, Aerosol, and Merged Layer V4.20 Products ; Winker et al., 2023
CALIOP longitude	Longitude; Level 2; V4.20; 1 km; Lidar Level 2 Cloud, Aerosol, and Merged Layer V4.20 Products ; Winker et al., 2023
AUX CloudMask	Cloud_Mask_1km; Level 2; Collection 6.1; 1 km; MODIS-AUX P_R05; Heather and Partain, 2017
AUX latitude	MODIS_Latitude; Level 2; Collection 6.1; 1 km; MODIS-AUX P_R05; Heather and Partain, 2017
AUX longitude	MODIS_Longitude; Level 2; Collection 6.1; 1 km; MODIS-AUX P_R05; Heather and Partain, 2017
2B layertop	LayerTop; Level 2 ; Version 1; 1 km; 2B-GEOPROF-LIDAR P2_R05_E06; Mace et al., 2007
2B cloudfraction	CloudFraction; Level 2 ; Version 1; 1 km; 2B-GEOPROF-LIDAR P2_R05_E06; Mace et al., 2007
2B latitude	Latitude; Level 2 ; Version 1; 1 km; 2B-GEOPROF-LIDAR P2_R05_E06; Mace et al., 2007
2B longitude	Longitude; Level 2 ; Version 1; 1 km; 2B-GEOPROF-LIDAR P2_R05_E06; Mace et al., 2007

[1]The MODIS and CALIOP variables were collocated and provided by an external collaborator (Dr. Wang), with the exception of the AUX CloudMask and 2B variables that were collocated by Henry Carr.

TABLE 3.2: Listing of AMSR-E, MERRA2, and ERA5 reanalysis dataset versions used and the specific variables used in this work and collocated with the satellite retrievals.

Reference Name	Full Variable Name; Version Number; Spatial Resolution; Product Name; Reference
MERRA2 surface pressure, atmospheric temperature, and atmospheric pressure levels	surface_pressure, air_temperature, vertical level; V5.12.4; 0.5° $\times$ 0.625 ° latitude $\times$ longitude; M2I3NPASM; Global Modeling and Assimilation Office, 2015a
MERRA2 surface temperature	surface_skin_temperature; V5.12.4; 0.5° $\times$ 0.625 ° latitude $\times$ longitude; M2T1NXSLV; Global Modeling and Assimilation Office, 2015b
ERA5 atmospheric temperature	Temperature; 0.25 ° $\times$ 0.25 ° latitude $\times$ longitude; ECMWF ERA5; Hersbach et al., 2023b
ERA5 surface pressure	Surface pressure; 0.25 ° $\times$ 0.25 ° latitude $\times$ longitude; ECMWF ERA5; Hersbach et al., 2023a
AMSR-E sea-ice concentration	Sea ice product; Version 3; 12.5 km; AE_SI12 (Level 3); Cavalieri and Comiso., 2014

More specifically, to analyse CTH and cloud-phase we must first collocate cloud property retrievals from the two separate CALIOP and MODIS instruments using the nearest great circle (a circle that lies in the plane of Earth's centre) distance method highlighted by Holz et al. (2008) and performed by Dr. Chenxi Wang, as described below.

To analyse MODIS cloud detection success, we will use the MODIS Aqua Level 2, 1 *km* CloudMask (referred to as CloudMask) product from the MODIS-AUX subset of data (Heather & Partain, 2017), and we will be comparing to the 2B-GEOPROF-LIDAR P2_R05_E06 layertop and cloudfraction products (Mace et al., 2007) (referred to as LayerTop and CloudFraction respectively).

First, i will describe the collocation technique used to collocate CALIOP and MODIS data. Then, once I have described the collocation technique implemented by Dr. Chenxi Wang, I will discuss the analysis methods for the MODIS CTH retrieval algorithm, CloudMask cloud detection retrievals and the MODIS cloud-phase retrievals.

3.2 Pixel by Pixel Collocation

We must define the coordinate system in use. We assume that the MODIS scan line coordinates are in the form of geodetic MODIS latitude, MODIS longitude and time. This assumes that Earth's surface is approximated as an ellipsoid and the horizontal location on the Earth's surface is measured using a horizontal datum, in this case geodetic latitude and longitude. In contrast to geocentric latitude, which is defined as the angle between the equatorial plane and a radial line connecting the surface and ellipsoid's center, geodetic latitude is defined as the angle between the equatorial plane and the surface at a point where the line intersects the surface at a perpendicular angle. Figure 3.1 illustrates this. The conversion between the two uses the following relation (Holz et al., 2008):

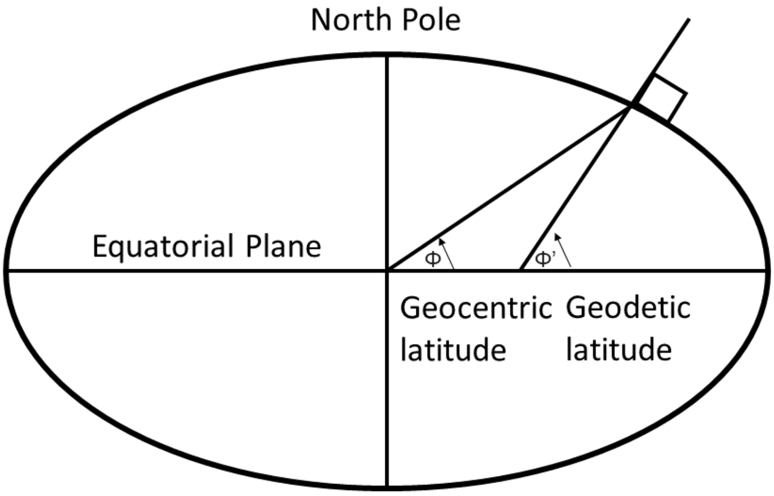

FIGURE 3.1: Geodetic vs geocentric latitudinal coordinates.

$$b^2 \tan(D) = \tan(C) \tag{3.1}$$

where $b^2 = 0.99327730$ and D and C are the geodetic and geocentric latitudes respectively.

We aim to know which CALIOP Ground Instantaneous Field of View (GIFOV) intersects the MODIS scan line. A MODIS scan path takes about 0.5 s (Holz et al., 2008) and contains 1354 pixels. Since the Earth rotates during this scan, the motion of the satellite and its scan line do not perfectly describe a great circle, however the approximation can be made given the movement of the Earth is much smaller than the length of the scan line. The time (t_1) that CALIOP is over a point (such as a MODIS field-of-view, FOV) can be found using a technique that relies on a 4th order polynomial solving technique developed by Froberg (1965). Given the satellite has an arc distance of $A(t)$ from the starting position at time t_0 the solution is (Holz et al., 2008):

$$t_1 = t_0 - \frac{A(t)}{A'(t)}. \tag{3.2}$$

Now that we have the time that the satellite will be abeam of a given MODIS FOV, we can know which CALIOP observation is approximately closest to the given MODIS FOV. It is worth noting that the technique must be adjusted by two factors. One, the Earth's eastward rotation during the scan creates an apparent westward movement for the satellite. We can find the approximate CALIOP's trace on the Earth's surface using the following three equations (Holz et al., 2008):

$$M = A \times B \tag{3.3}$$

$$V_t = V_s - E\cos(l)U_e \tag{3.4}$$

$$P = R \times V_t \tag{3.5}$$

where A and B are the initial and final positions of the MODIS scan position vectors measured in the geodetic coordinate system, V_s is the velocity of the CALIPSO satellite through space (adjusted by the ratio of the Earth's radius to the satellite radius vector), U_e is the unit vector pointing East at the particular FOV at latitude l, E is a scalar of the eastward speed of rotation at the Earth's equator measured in the same units as V_s, and R is the terrestrial position vector of the particular FOV. The cross product between P and M points to the position of the intersection between the CALIOP trace and the MODIS scan line. Though the initial CALIOP FOV may be far from this new adjusted intersection, using the Eqn. 3.2 we can find the time when CALIOP is over this point using the new intersection position vector in Eqn. 3.2.

The second adjustment is due to the fact that MODIS does not only take nadir readings (Wang et al., 2011), and is called the parallax effect. The impact of this can

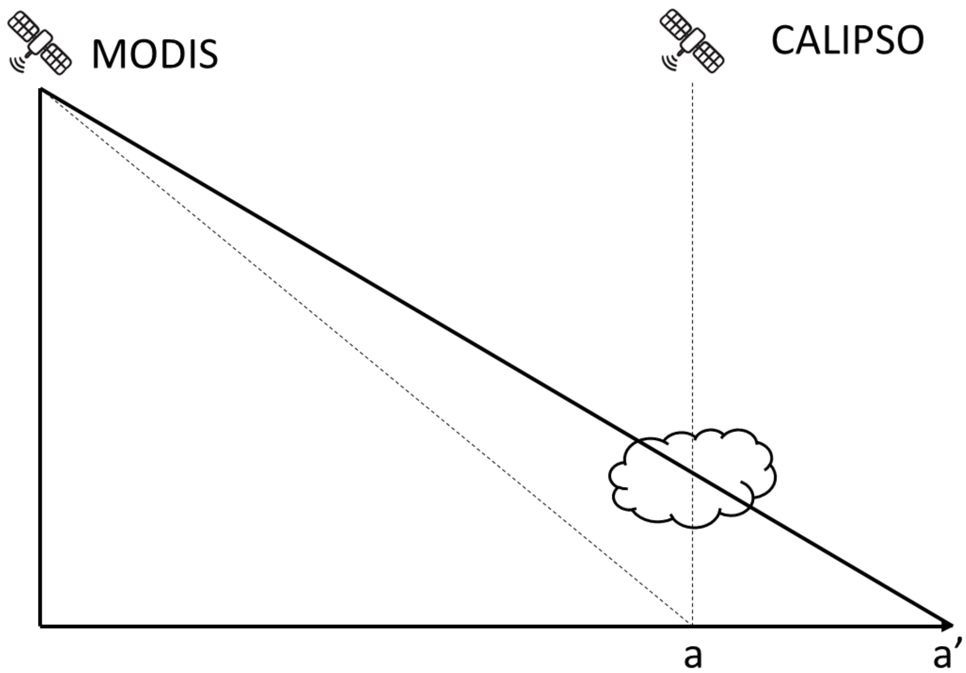

FIGURE 3.2: Schematic detailing the impact of the parallax effect on the collocation of MODIS and CALIOP.

be seen in Figure 3.2. The ground footprint of MODIS is not directly below the cloud, whereas for CALIOP it is. Hence, if the parallax effect is not taken into account the cloud CALIPSO detects at point a will be projected onto point a' by MODIS, and hence the surface projection of the two detectors will be out of alignment. The collocation method therefore adjusts the reading by using CALIOP's CTH and MODIS' solar zenith and azimuth angles to determine the cloud displacement vector. It uses this to adjust the MODIS pixel location to the correct position on the Earth's surface. The importance of this is lessened for lower clouds.

It is worth noting that an alternative collocation method involves creating a table of CALIOP points on the Earth's surface and interpolating the distance of each from the MODIS FOV, however this is computationally heavy so is not preferred.

3.3 Hypothesis 1

To investigate Hypothesis 1, I first filtered the MODIS and CALIOP data to only include single-layer clouds. To select pixels where both instruments agreed that a single-layer cloud is being detected, I used the MODIS multi-layer cloud flag variable and CALIOP's CTH product, which breaks the atmosphere up into 10 layers allowing us to select only those pixels where a CTH value is present in only one of the 10 vertical layers. Finally, I also selected points where CTH, according to both MODIS and CALIOP, was between 0 km and 2 km (including $2km$) to filter for low-level clouds. We also filtered the data such that only pixels where a successful COT21 τ retrieval occurred were included, and that this COT21 τ retrieval had a value of less than or equal to 20, so that the influence of the surface could be analysed for optically thinner clouds. τ is determined by the MODIS COT21 1 km variable since CALIOP attenuates quickly and so fails to retrieve larger τ values for optically thicker clouds.

First, for these single-layer low-level pixels, I plot a representation of a 2D probability density function calculated using the python function guassian kernel-density estimate described in "SciPy Gaussian KDE Function - v1.11.2 Manual", 2023 (from module scipy-stack/2020b) (Virtanen et al., 2020). I also calculated the mean bias error and absolute average error for MODIS CTH compared to CALIOP CTH. This analysis prompted a further filter to be applied to the CALIOP data to allow for a less biased limit, which will be discussed more in Section 4.2. All data for the rest of Section 3.3 was subsequently filtered to only include pixels where CALIOP CTH was less than 1.2 km. For these composites of single-layer low-level cloud CTH retrievals we aggregated the data into 100 $\times$ 100 collocated τ–LTS bins. This aggregation takes all the collocated MODIS and CALIOP CTH values where the corresponding τ and LTS values are between the two extreme values for each τ–LTS bin, and then calculates the mean CTH difference ($CTH_{MODIS} - CTH_{CALIOP}$) in each bin. Then I plot the bins in a 2D histogram plot with τ on the y-axis and LTS on the x-axis, where the color bar shows the mean CTH difference. A statistical limit of 50 points was used in the aggregation to remove bins with too few data to be of statistical significance. We also aggregated the mean CTH difference into 30 $\times$ 360 latitude $\times$ longitude bins for polar-day 2015, April 2015, and August 2015. These aggregated bins were then projected onto an Arctic map plot.

To compare the MODIS CTH bias to LTS, I first needed to construct temporally and geospatially accurate LTS readings collocated with our satellite retrievals, since it is not a variable retrieved by MODIS or CALIOP.

3.3.1 LTS Grid

LTS is a measure of thermodynamic stability and indicator of the temperature structure of the atmosphere, as is defined by the Eqn. 2.3. To obtain the LTS values, I created a LTS grid with a spatial resolution of 0.625 $^\circ$ longitude $\times$ 0.5 $^\circ$ latitude and a temporal resolution of 3 hours from the Modern Era Retrospective Analysis for Research and Applications version 2 (MERRA2) atmospheric pressure and temperature reanalysis data (Gelaro et al., 2017).

MERRA2 is reanalysis data which aims to provide a consistent reprocessing of meteorological observations (Gelaro et al., 2017). By using a forecast model to combine physical observations reanalysis data produces physically consistent gridded datasets for a given variable. The MERRA2 dataset is produced using the Goddard Earth Observing System (GEOS) version 5.12.4 (Gelaro et al., 2017) data assimilation system based on the GEOS atmospheric model (Reinecker et al., 2008). This model is able to resolve both troposphere and stratosphere structures to run uncoupled and coupled climate simulations and predictions based on four types of physical processes: moist, radiation, turbulent mixing and surface processes.

Using the hypsometric equation I calculated the 2 m pressure ($P_{2\ m}$) (Wallace & Hobbs, 1977):

$$P_{2\ m} = P_s \times e^{-g \times h/(R \times \bar{T})}, \tag{3.6}$$

where h is the altitude above the surface equal to 2 m, g is the gravitational constant equal to 9.8 $m\ s^{-1}$ and R is the specific gas constant for dry air equal to 287 $J\ kg^{-1}\ K^{-1}$. I approximated the virtual temperature of the $surface - 2\ m$ layer as the mean air temperature ($\bar{T}$) between the two largest pressure levels given since I did not have access to the virtual temperature of the $surface - 2\ m$ layer in the MERRA2 dataset. I used 3-hourly surface pressure (P_s), atmospheric pressure and atmospheric temperature (T) data from the MERRA2 dataset to calculate $P_{2\ m}$ and $\bar{T}$ at a 3-hourly resolution, where T is provided at 42 pressure levels. Then I calculated LTS (as previously defined in Section 2.1) at a resolution of 0.625 ° longitude × 0.5 ° latitude using the following equation (Wood & Bretherton, 2006):

$$LTS = T_{P_1} \times (\frac{P_0}{P_1})^k - T_{2\ m} \times (\frac{P_0}{P_{2\ m}})^k, \tag{3.7}$$

where $T_{2\ m}$ then comes from taking the nearest above surface pressure layer to $P_{2\ m}$ in the MERRA2 dataset and selecting the corresponding T value. P_0 is the reference pressure value (1000 hPa), P_1 is 800 hPa, and k is the ratio of R and the specific heat capacity at a constant pressure equal to 0.286. The MERRA2 dataset provides T_{P_1}, the temperature at 800 hPa.

We will also use the MERRA2 dataset to create an estimate of the 900 hPa temperature lapse rate at the same resolution as the LTS grid. To do this, we will take the temperature at 900 hPa and difference this with the temperature of the lowest atmospheric level at that latitude and longitude. Then, we will use the hypsometric equation to calculate the geometric thickness between the surface and 900 hPa, approximating virtual temperature as the mean temperature between the surface and the 900 hPa level. Points where the surfaces sits near the 900 hPa pressure level, and hence the first atmospheric temperature assignment in the MERRA2 dataset is at 900 hPa, are removed. We then divide the temperature difference between the surface and 900 hPa by the geometric thickness to get an estimate of the atmospheric temperature lapse rate.

We also reconstructed LTS using the European Environment Agency (ERA5) reanalysis data-set from the European Centre for Medium-Range Weather Forecasts (ECMWF) to test the robustness of our results. We used 3-hourly P_s and atmospheric T values as a function of 37 atmospheric P levels to produce $P_{2\ m}$ and $T_{2\ m}$ values using Eqn. 3.6. $T_{2\ m}$ is obtained from selecting the T value for the nearest ERA5 pressure level to $P_{2\ m}$. LTS is then constructed using Eqn. 3.7 for a grid resolution of 0.75 $^\circ$ longitude $\times$ 0.5 $^\circ$ latitude. This was done by selecting every other latitudinal data point in the ERA5 grid and every third longitudinal data point.

After creating the global LTS grid at a 3-hourly resolution for both datasets, I collocated the LTS readings with the MODIS CTH and τ retrievals by selecting the LTS value with the nearest latitude, longitude and temporal coordinates. Here, nearest LTS latitude (or longitude or time) is the latitude where the absolute difference with the MODIS CTH latitude is smallest for the entire LTS grid. The temperature lapse rate grid will also be collocated with the MODIS pixels using the same technique.

3.4 Hypothesis 2

To investigate Hypothesis 2, I will be filtering the data to only include single-layer low-level clouds ($0 - 2\ km$) in our analysis for polar-day for 2015 using the same technique described in Section 3.3. Then I will use the Community Radiative Transfer Model (CRTM) to calculate TOA clear-sky BTs for Channel 31 of MODIS at a wavelength of 11 μm ($BT_{11\ \mu m}$(CRTM)). Then, I will use $BT_{11\ \mu m}$(CRTM) in conjunction with collocated measured MODIS Channel 31 TOA BT readings for cloudy pixels ($BT_{11\ \mu m}$(MODIS)) to reconstruct the shared numerator in Eqn. 2.1 and Eqn. 1.1. I am using the CRTM model in place of the PFAAST model that MODIS actually uses since I do not have access to the latter, and collocated Advanced Microwave Scanning Radiometer for the Earth Observing System (AMSR-E) fractional sea-ice coverage data.

First, I will describe the CRTM model and our implementation of it to obtain clear-sky BTs. Then I will describe the AMSR-E sea-ice concentration dataset that will be used in our analysis technique of Hypothesis 2. After, I will describe our analysis techniques for analyzing the zonal averaging of the apparent BTLR and the use of unrealistic fractional sea-ice values in the MODIS CTH algorithm.

3.4.1 CRTM

To analyse Hypothesis 2, I will use the CRTM to replicate the process used by MODIS to calculate the clear-sky $BT_{11\ \mu m}$ in place of the PFAAST model. The CRTM model is a radiative transfer model that uses inputs such as surface emissivity and vertical atmospheric structure (obtained from MERRA2 data) to calculate outputs such as TOA radiance for sensors such as MODIS Aqua. The model uses the inputted atmospheric, surface, sensor structure, and a gaseous absorption model in a radiative transfer component to calculate forward radiance outputs at the TOA. The gaseous absorption model interpolates LUTs of optical properties such as scattering albedos and extinction coefficients to calculate the impact of aerosols and clouds on the transmittance of radiance (Delst et al., 2020).

Two radiative models are used by CRTM. First is the advanced doubling adding (ADA) method which is chosen as a baseline, an accurate tool for multiple-scattering calculations (Liu & Weng, 2006). The principle of the double-adding method was first put forward by Stokes (1862), which describes the intensity of light transmitted through a layer with the additional intensity from internal reflection within the layer taken into account. It assumes that the reflection and transmission of a layer twice as thick as a single thin homogeneous layer (for which transmission and reflection properties are assumed to be known) is obtained by summing the contributions of two identical juxtaposing slabs. In strongly scattering profiles, the successive order of interaction (SOI) has also been implemented as described by Heidinger et al. (2006).

3.4.2 AMSR-E Sea-Ice Concentration

To analyze Hypothesis 2, I will also need collocated sea-ice fractional cover values. These were collocated with the CALIOP retrievals by selecting the nearest pixel to each CALIOP retrieval. I will use the AMSR-E sea ice concentration product that makes use of the polarization and spectral gradient ratios in two polarized channels (19 GHz and 89 GHz) (Markus et al., 2012). A polarization ratio is a fucntion of the BT in the horizontal and vertical components in two channels, obtained using passive microwave data from the Special Sensor Microwave Imager (SSMI) on the U.S. Defense Meteorological Satellite Program satellites. In contrast, spectral gradient ratios are a function of the BTs in both channels for a particular polarization (horizontal or vertical) (Markus & Cavaleri, 2009).

Theoretical values of the polarization and spectral gradient ratios are calculated using the NASA Team algorithm described by Markus and Cavaleri (2009) for all frequency, polarization, ice concentration and weather combinations to create a LUT. This highlights that the ratios are functions of weather and ice concentration values, and hence for a given polarization and frequency measurement by the SSMI instrument the nearest ice concentration–weather combination can be found where the three-dimensional distance between the measured and pre-computed values is smallest.

3.4.3 BTLR Replication

In MODIS, the BTLR measurements are constructed using Eqn. 1.1 where $BT_{11\ \mu m}(\text{PFAAST})$ is obtained from the PFAAST model and then zonally averaged for each month (Baum et al., 2012), and CTH_{CALIOP} are collocated CALIOP CTH values. Our reconstruction of Eqn. 1.1 is in contrast to the actual method MODIS uses which uses the PFAAST model for the clear-sky model readings in the 11 μm channel, where instead I will be using CRTM.

For each low-lying single-layer cloud detected not over land or open-ocean (defined as the points where the sea-ice fractional coverage is greater than 0 % according to AMSR-E) in the Arctic in polar-day in 2015, I will be assigning a vertical temperature structure obtained from collocated MERRA2 atmospheric temperature and pressure values. I will also assign the CRTM surface temperature to be equal to the collocated MERRA2 surface temperature. I will then run the CRTM model, which outputs TOA BT at 11 μm in clear-sky conditions ($BT_{11\ \mu m}(\text{CRTM})$) as would be detected by the MODIS Aqua satellite, for two scenarios: first using underlying sea-ice fractional cover value set to 0 % to replicate MODIS (which I will refer to as the unrealistic scenario), and then again setting the underlying sea-ice fractional cover value equal to collocated sea-ice fractional values from AMSR-E data (which I will refer to as the realistic scenario).

For each scenario I will replicate Eqn. 1.1 with $BT_{11\ \mu m}(\text{PFAAST})$ replaced with $BT_{11\ \mu m}(\text{CRTM})$, collocated MODIS BT readings in the 11 μm channel as $BT_{11\ \mu m}(\text{MODIS})$, and collocated CALIOP CTH readings as CTH_{CALIOP}. Then I will aggregate BTLR data for 2015 polar-day into 6 $^\circ$ longitude $\times$ 0.371 $^\circ$ latitude bins (centred on $-177\ ^\circ E$, $-171\ ^\circ E$ etc longitude and 61.186 $^\circ N$, 60.557 $^\circ N$ etc latitude), then take the mean of each bin. I will plot these means in a 2D histogram to evaluate the longitudinal variation of Arctic BTLR and test the validity of zonally averaging

BTLR in the MODIS CTH algorithm.

Next, I will zonally average all the BTLR readings into 22 latitudinal bins (centred on 60.5 $^{\circ}N$, 61.5 $^{\circ}N$ etc latitude), and plot the results against the latitudinal bin centres for both scenarios. Then I will calculate the mean of these zonal averages for both scenarios. This will allow us to quantify how the use of realistic sea-ice values affects the longitudinally averaged BTLR readings that MODIS uses in its CTH calculations.

I will also run the CRTM model to output $BT_{11\ \mu m}(\text{CRTM})$ collocated with surface temperature obtained from the MERRA2 dataset and $BT_{11\ \mu m}(\text{MODIS})$ retrievals under clear-sky conditions. These will be pixels where neither MODIS nor CALIOP detects any cloud. This will be done to verify the relationship between our replicated CRTM BT values and those directly measured by MODIS in the 11 μm channel.

3.4.4 CTH Replication

As with the apparent BTLR replication (Section 3.4.3), I will run the CRTM model using MERRA2 atmospheric temperature, surface temperature, and pressure values for each single-layer low-level cloud not overlying land or open-ocean (defined as the points where the sea-ice fractional coverage is greater than 0 % according to AMSR-E) in the Arctic to output clear-sky BT for two scenarios: first I will set the underlying surface to 0 % sea-ice cover (which I will refer to as the unrealistic scenario), second I will set the underlying surface to AMSR-E collocated sea-ice fractional cover values (which I will refer to as the realistic scenario).

To analyse the effect of assuming that there is no sea-ice underlying the cloud on CTH I will first reconstruct the zonally averaged BTLR readings used by MODIS. I am using the same BTLR readings used by MODIS, rather than our own replicated BTLR readings from Section 3.4.3, so that the only difference between the two scenarios is the surface emissivity value used by CRTM in calculating the clear-sky BT in the numerator in Eqn. 2.1. The MODIS BTLR readings ($BTLR_{Baum}$) can be reconstructed using the fourth order polynomial coefficients found in Baum et al. (2012), substituting them into:

$$BTLR_{\text{Baum}} = a_0 + a_1 lat + a_2 lat^2 + a_3 lat^3 + a_4 lat^4 \tag{3.8}$$

where lat is the latitude of our collocated MODIS measurements, and a_1, a_2, a_3, a_4 are the polynomial coefficients given in Baum et al. (2012). For each month there are different coefficients and latitude ranges described in Table 3.3. Once this has been done successfully, these reproduced $BTLR_{Baum}$ readings will be used in the denominator in Eqn. 2.1.

TABLE 3.3: List of coefficients describing the fourth-order polynomial parameterization of apparent BTLR for Eqn. 3.8, from Baum et al., 2012, and the latitude range in which they apply.

month	coefficients [a_0, a_1, a_2, a_3, a_4]	latitude range
03	[3.1251275, -0.1214572, 0.0146488, -0.0003188, 0.00000210]	10.7 °N – 90 °N
04	[13.3931707, -1.2206948, 0.0560381, -0.0009874, 0.00000598]	29.4 °N – 90 °N
05	[1.6432070, 0.1151207, 0.0033131, -0.0001458, 0.00000129]	14.9 °N – 90 °N
06	[-5.2366360, 1.0105575, -0.0355440, 0.0005188, -0.00000262]	16.8 °N – 90 °N
07	[-4.7396481, 0.9625734, -0.0355847, 0.0005522, -0.00000300]	15.0 °N – 90 °N
08	[-1.4424843, 0.4769307, -0.0139027, 0.0001759, -0.00000080]	19.5 °N – 90 °N
09	[-3.7140186, 0.6720954, -0.0210550, 0.0002974, -0.00000150]	17.4 °N – 90 °N

For each scenario I will replicate Eqn. 2.1 with $BT_{11\ \mu m}$(PFAAST) replaced with $BT_{11\ \mu m}$(CRTM), collocated MODIS BT readings in the 11 μm channel as $BT_{11\ \mu m}$(MODIS), and reconstructed $BTLR_{Baum}$ as the BTLR values. I will then plot a 2D density plot of our replicated MODIS CTH against actual MODIS CTH readings for both the scenarios. This will first allow us to verify the validity of using the CRTM model by comparing the 0 % fractional sea-ice calculations to MODIS measurements. Then I will analyze the impact of using realistic sea-ice values by calculating the mean of the difference between the replicated MODIS CTH and measured MODIS CTH in both scenarios.

3.5 Cloud Detection

3.5.1 CloudMask and Cloud Fractional Agreement

To analyse the success of the MODIS cloud detection algorithm I will first analyse the performance of the MODIS CloudMask. As highlighted in Section 1.2.2, the MODIS CloudMask produces a 48 bit output that gives four classifications for each pixel: cloudy, uncertain clear, probably clear, and confident clear. The MODIS-AUX product, as described by Heather and Partain (2017), is a subset of MODIS C6 radiance and CloudMask data that overlaps each CloudSat cloud profiling radar (CPR) footprint from MODIS data fields at a 1 km resolution. It uses the great-circle nearest-neighbor scheme to locate each MODIS pixel to the nearest CloudSat pixel, storing the 3 nearest across-track MODIS pixels and 5 nearest along-track MODIS pixels for each CloudSat pixel. We will only analyse the 2^{nd} across-track and 3^{rd} along-track CloudMask pixel.

The 2B-GEOPROF-LIDAR data product is a combination of the CPR and CALIOP CloudMask products aiming to provide a complete picture of aerosol and cloud occurrence (Mace et al., 2007). Unlike CALIOP which struggles with optically thick cloud layers due to attenuation problems, CPR has an accurate ability to analyse optically thick cloud layers and large-particle layers due to its longer wavelength. It utilises a 94 GHz frequency that is better able to penetrate further into optically thicker clouds (Marchand et al., 2008). The method for combing CPR and CALIOP is described in Mace et al. (2007). It is worth highlighting however that 2B-GEOPROF-LIDAR has its own limitations, including a difficulty in viewing cloud fraction in the bottom 1 km of the atmosphere in comparisons to surface based observations (Liu et al., 2017).

The aim is to analyse the performance of MODIS in terms of fractional coverage of clouds for single-layer, low-level clouds. For these products the active observations will be taken to be the truth for the multi-layer and CTH detection. Hence, I will be filtering for single-layer low-level clouds using the 2B-GEOPROF-LIDAR LayerTop variable to indicate points where a single cloud was detected in the $0 - 2\ km$ range as the MODIS AUX product does not contain the multi-layer flag.

To analyse the performance of the MODIS-AUX CloudMask, which does not directly give cloud fractional coverage, I will calculate the fractional coverage parameter for each of the 10 $^\circ$ longitude $\times$ 3 $^\circ$ latitude bins in the Arctic, where the bins are centred at 5 $^\circ E$, 15 $^\circ E$, etc. longitude and 61.5 $^\circ N$, 64.5 $^\circ N$, etc. latitude, respectively. The MODIS-AUX fractional coverage parameter is defined as $CF_{AUX} = \frac{C}{T}$ where C and T are the number of pixels classified as cloudy and the total number of pixels (including uncertain, clear, and cloudy points) respectively in each bin. To analyse the success of the CF_{AUX} approximation these bins will be calculated for September in 2015. I will also calculate the mean cloud fractional coverage (CF_{2B}) from the collocated 2B-GEOPROF-LIDAR dataset in the same 10 $^\circ$ longitude $\times$ 3 $^\circ$ latitude bins for the same month. I will then plot the monthly mean CF_{AUX} and CF_{2B} against the longitude bin centres for a latitude of 85.5 $^\circ N$. This will allow us to investigate the performance of the CF_{AUX} approximation of cloud fraction compared to CF_{2B} cloud fraction for a 10 $^\circ$ longitude $\times$ 3 $^\circ$ latitude resolution.

Once this technique has been validated, I will plot daily-averaged CF_{AUX} and CF_{2B} in all latitude and longitude bins north of 60 $^\circ N$ during the 2015 polar-day in a 2D density plot. This will be done by taking every pixel in a given day within each 10 $^\circ$ longitude $\times$ 3 $^\circ$ latitude bin and calculating CF_{AUX} and CF_{2B} for these aggregates. The x-axis will be the average AMSR-E sea-ice concentration in the respective latitude and longitude bin and the y-axis the daily-average CF_{AUX} or CF_{2B} within the respective bin. The AMSR-E average sea-ice concentration will be determined by aggregating all sea-ice fractional coverage values within each latitude and longitude bin for each day and then taking the mean of this fractional coverage. I will then difference the daily-average CF_{AUX} and CF_{2B} values and produce a density plot of the results with the y-axis representing the $CF_{AUX} - CF_{2B}$ difference and the x-axis the daily-average AMSR-E sea-ice concentration within each latitude and longitude bin, aiming to analyse the surface-type sensitivity of the success rate of the MODIS CloudMask cloud detection algorithm compared to the 2B-GEOPROF-LIDAR dataset.

3.5.2 Cloud-Phase Hitrate

Once I have analysed the MODIS CloudMask detection performance, I will move on to investigating the success of the MODIS cloud-phase detection algorithm. The cloud-optical properties phase algorithm, which is made up of 4 separate tests (see Section 1.2.3), is only implemented if the CloudMask returns the pixel as 'cloudy' or 'probably cloudy', or if the CSR returns the pixel as "not cloudy" (Marchant et al., 2016). The TIR and OP phase retrievals provide four options for each pixel. The pixel is classified as clear-sky, liquid phase, ice phase, or uncertain. The OP retrieval also has an additional classification of 'no-data'. Likewise, the CALIOP phase retrieval mechanism produces four classifications for each pixel: no-data/unknown, liquid phase, ice phase, and horizontally orientated ice crystals. Using TIR and OP phase retrievals collocated with CALIOP's cloud-phase retrieval mechanism at the pixel level, I will analyse the phase detection success rate against CALIOP for low-level single-layer clouds, filtered for using the same technique described in Section 3.3.

To analyse the phase detection success rate for liquid and ice clouds, I will define a metric called phase hitrate:

$$hitrate(phase\ x) = \frac{A}{P} \tag{3.9}$$

where A is the total number of pixels where MODIS and CALIOP agree that the phase of the cloud is *phase x* (liquid or ice) plus the number of pixels where they agree no cloud is detected. P is the total number of agreement pixels plus the number of pixels where either MODIS or CALIOP detect a cloud of *phase x* and the other detects no cloud. I will partition these points into pixels where the underlying sea-ice fraction is between two extreme values of 10 separate sea-ice bins (ranging from 0 to 1.0 fractional coverage centred on 0.5, 0.15 etc.) using collocated AMSR-E sea-ice fractional coverage data. I will plot the hitrate against the sea-ice bins along with the number of points analysed. I will also calculate the average hitrate for every month in the Arctic 2015 polar-day for both TIR and OP, also plotting the number of points analysed. For the seasonal analysis, *phase x* can be either liquid or ice, and the data will be filtered such that the pixels sit over ocean regions only. Similarly, I will also plot the seasonal hitrate over ocean regions again, but this time with pixels that the two instruments agree no cloud is detected in removed.

Our investigation differs from previous investigations into the C5 pixel-to-pixel phase detection rate in several ways (Liu et al., 2010). First, I have removed uncertain pixels from the denominator in Eqn. 3.9 while using the updated C6 algorithm. Moreover, Liu et al. (2010) analysed polar-night cases between July 2007 and June 2008, breaking up the analysis into sea-ice vs open-ocean cases when plotting a seasonal hitrate analysis. Instead I will be breaking up our analysis into sea-ice bins and, separately, monthly hitrates for 2015 polar-day.

Generally, we might expect the OP hitrate to perform better than the TIR hitrate since it is the result of a weighted vote from the TIR test and three additional more stringent tests, allowing greater adaptability to different cloud scenes. Moreover, we might expect the MODIS hitrate to perform worse for liquid phase clouds based on the literature, since liquid phase clouds are often mis-classifed as ice phase, particularly for low-lying maritime broken cloud scenes (Platnick et al., 2018). It should be noted however that in the summer there are many stratiform Arctic clouds and so broken cloudy scenes should be less of an issue (Curry et al., 1996). Finally, as with CTH we might expect high sea-ice coverage pixels to cause MODIS to struggle with phase discrimination due to the low thermal contrast between the cloud and the underlying surface. However, the inclusion of the β parameter may go someway to resolving this bias.

Chapter 4

Results and Discussion

4.1 Low-Level, Single-Layer Clouds

In this study I will be evaluating low-level, single-layer cloud-top properties for the MODIS instrument. The collocation methodology, described in Section 3.2, was first verified to make sure the data points from the two satellites were aligned. This check was done throughout the project by computing the maximum absolute latitudinal and longitudinal differences between the MODIS and CALIOP geolocations to confirm that the difference was small. Once this was done, we calculated the total number (T) of single-layer low-lying (CALIOP CTH $\leq$ 2 km and MODIS CTH $\leq$ 2 km) clouds according to each instrument and technique independently, and the percentage of these that are classified as liquid and ice-phase respectively. The key statistics describing these data points can be seen in Table 4.1. Note that the percentages do not add up to 100 % because some pixels are classified as uncertain.

In Table 4.1, it can be seen that out of the low-level, single-layer clouds detected by MODIS the TIR retrieval technique detects much fewer liquid clouds compared to the OP retrieval mechanism. As will be discussed in more detail in Section 4.5 and already outlined in Section 1.2.3, it is known that the TIR technique struggles classifying liquid-phase clouds. However of particular interest is that CALIOP detects many more single-layer, low-level clouds than MODIS does. This is likely due to the attenuation of the CALIOP beam through optically thicker clouds. It is

TABLE 4.1: Statistics of 2015 polar-day single-layer, low-level clouds as determined by the MODIS TIR 1 *km* and OP 1 *km* phase retrieval mechanisms and CALIOP's own retrieval mechanism separately. A total of 1.385×10^7 collocated retrieval points were analysed. The detection of single-layer and low-level clouds utilises the same technique described in Section 3.3 for each instrument, however in this instance does not require that the two instruments agree that a single-layer low-level cloud is detected. Rather, T is the total detected single-layer low-level clouds according to each instrument and retrieval method independently.

	T	Liquid [%]	Ice [%]
MODIS TIR	1,944,294	66.1	10.1
MODIS OP	1,944,294	91.3	7.1
CALIOP	3,942,895	92.3	3.4

known that the CALIOP beam attenuates quickly after larger τ values. Generally, a cloud is considered opaque by CALIOP when backscatter signals below the layer are determined to be absent, and generally occurs after a detected τ value of ~ 4 for daytime retrievals (Young et al., 2018). This would mean that layers below the opaque cloud are not detected by the lidar instrument, and could mean that the pixel actually contains multiple cloud layers.

To avoid issues of attenuation, I filtered the data (as described in Section 3.3) such that the instruments agreed that they were detecting a single-layer cloud in the 0–2 *km* range. I was able to evaluate over 1,265,000 data points in the Arctic during 2015 polar-day for which the instruments MODIS and CALIOP agreed that low-level, single-layer clouds were detected.

4.2 Hypothesis 1 Results

Hypothesis 1 states that MODIS underestimates CTH when τ is small and LTS is low. First, Fig. 4.1a shows a comparison of MODIS and CALIOP CTH, for points where the two instruments agree that a single-layer low-level cloud is detected, by plotting a representation of a probability density function of this 2-dimensional space calculated using the python function Gaussian kernel-density estimate described in

"SciPy Gaussian KDE Function - v1.11.2 Manual", 2023. The dashed regression line B is calculated for all data points in the 0–2 *km* range (orange) and is described by $y = 0.790 \times x$, where x is the x-axis coordinate [km] (CALIOP CTH) and y is the y-axis [km] (MODIS CTH), calculated using a curve fit python function ("SciPy Curve Fit Function - v1.11.2", 2023) and forced through $y = 0$, $x = 0$, since we have filtered our data to agree that a cloud is detected. Similarly, the regression line A is calculated for data points restricted to the 0–1.2 *km* range according to CALIOP CTH, described by $y = 1.016 \times x$. Line A is shown because restricting CALIOP CTH to less than 1.2 *km* gives MODIS room to overestimate as well as underestimate CALIOP CTH. Since we have filtered the data such that the two instruments agree that a cloud is detected between 0–2 *km*, the regression calculation for line B does not take into account data points where CALIOP detects CTH to be near 2 *km* but MODIS detects CTH greater than 2 *km*. Hence, line A is considered to provide a more accurate assessment of the true relationship between CALIOP and MODIS CTH.

MODIS generally underestimates CALIOP CTH when we analyse regression fit B, where CALIOP has a mean CTH of 0.934 *km*, with the mean CTH difference (MODIS − CALIOP) equal to −0.116 *km*. This is particularly interesting to note since MODIS CTH in C5 was found to have a overall positive bias in the Arctic of 0.3 *km* and 0.1 *km* for August 2006 and February 2007 in comparison to CALIPSO according to Holz et al. (2008). Our initial results suggest that the inclusion of the apparent BTLR in the C6 CTH retrieval method has lead to a decreased magnitude of the absolute difference compared to CALIOP, but MODIS now seems to have a low bias if we analyse regression fit B. This aligns with previous research by Baum et al., 2012 that showed that the inclusion of the apparent BTLR reduced global positive overestimates (as discussed in Section 4.2).

However, at low CALIOP CTH values (less than 1.2 *km*) MODIS generally performs slightly better according to the linear regression fit, with many points showing

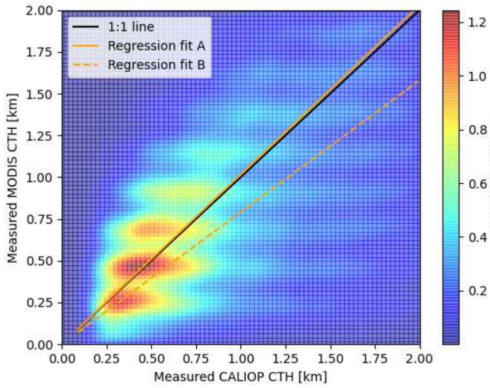

(A) MODIS and CALIOP CTH probability density function plot. The black line represents the 1:1 markers, the orange line a linear regression fit only taking into account points where CALIOP CTH is less than or equal to 1.2 km (and MODIS CTH $\leq$ 2 km) described by $y = 1.016 \times x$, and the dashed orange line a linear regression fit for all data (CALIOP CTH $\leq$ 2 km and MODIS CTH $\leq$ 2 km) described by $y = 0.790 \times x$. The plot is split into 80 $\times$ 80 bins centred on 0.0125 km, 0.0375 km, etc. CTH.

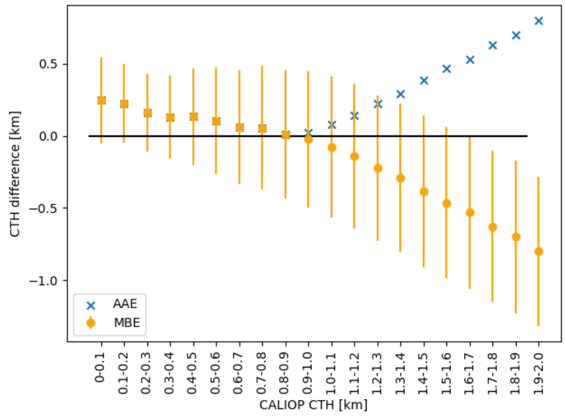

(B) CTH mean bias error (MBE) and absolute average error (AAE) for all single-layer, low-level clouds in polar-day 2015. MBE is calculated by taking the mean CTH difference (MODIS - CALIOP) in each bin, centred on 0.05 km, 0.15 km, etc. CALIOP CTH, and AMBE by taking the absolute value of the MBE values. The bars on MBE represent the standard deviation of the CTH difference in each bin.

FIGURE 4.1

that MODIS actually slightly overestimates the CALIOP CTH values. This is supported by regression line A that is slightly steeper than the 1:1 line. This is reflected in a mean CTH difference (MODIS $-$ CALIOP) for data points where CALIOP CTH $\leq$ 1.2 km with a positive value of 0.049 km and a standard deviation of 0.412 km. Moreover, the magnitude of the error seems to increase with CTH between the 1–2 km level according to Fig. 4.1b. This might simply be because at larger CTH values there is more room for error (in either direction). However, we propose that it is a result of our data filtering that restricts all retrievals to having a MODIS CTH smaller than 2 km. As mentioned earlier, this filtering could neglect many points that overestimate CALIOP CTH at values closer to 2 km and therefore skew the mean bias error (MBE) to larger negative values. Hence, we consider regression line A to be a more accurate representation of the CTH comparison. Therefore, we will filter the rest of the results in Section 4.2 such that CALIOP CTH is less than 1.2 km. All data points and figures evaluated in this section therefore now contain single-layer clouds according to both

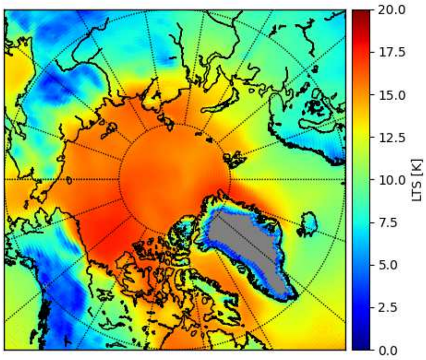

(A) MERRA2 LTS

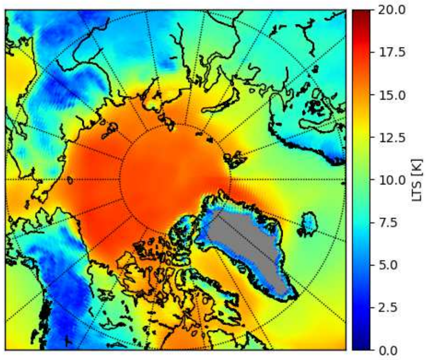

(B) ERA5 LTS

FIGURE 4.2: Polar projections of average LTS in 2015 polar-day, where LTS is constructed at a 3-hourly temporal resolution and at a spatial resolution of 0.625 ° longitude ×0.5 ° latitude from the MERRA2 dataset, and at a resolution of 0.75 ° longitude × 0.5 ° latitude from the ERA5 datasets.

instruments and a cloud top height in agreement with the determined MODIS CTH less than 2 km and the CALIOP CTH less than 1.2 km.

Fig. 4.2 shows our MERRA2 and ERA5 constructed LTS averaged over 2015 polar-day and polar-projected. It is worth highlighting that no LTS values are seen in areas where the surface sits at a pressure level smaller than 800 hPa, such as the Greenland ice-sheets. In general, the result shows the hypothesised pattern of higher LTS over regions that generally contain higher sea-ice values (as discussed in Section 2.1), and lower over land. Figure 4.2a and 4.2b show similar spatial patterns for the climatological 2015 polar-day average of LTS, validating the consistency of my technique used to construct the LTS grid across both datasets as described in Section 3.3.1. It is important to highlight that since I are using the 800 hPa LTS, small LTS values may indicate that surface altitude is close to 800 hPa, rather than that the lower troposphere has a low stability.

Figure 4.3 shows the CTH climatology in the LTS-τ space for MODIS and CALIOP, where LTS is constructed using MERRA2 data. One observation is that the mean MODIS CTH (Fig. 4.3b) in low LTS and higher τ bins is noticeably higher that

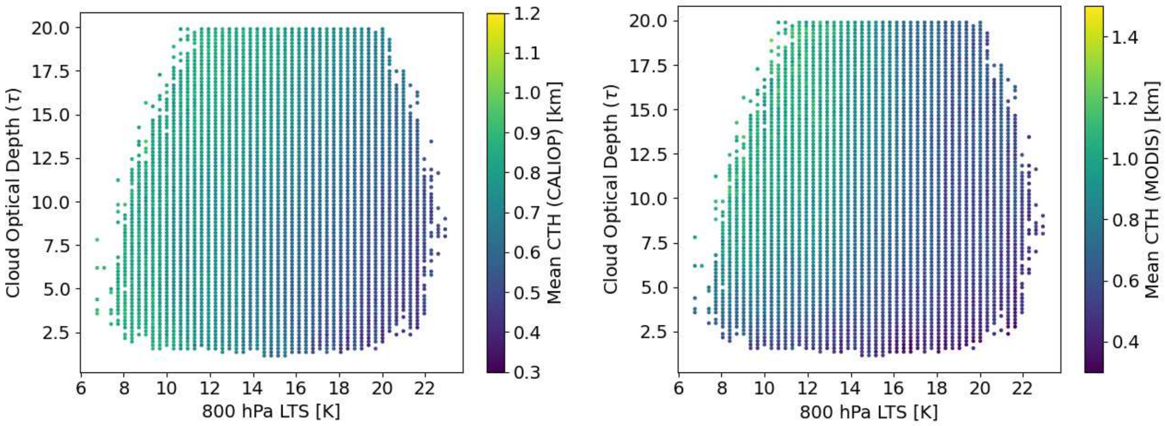

(A) CALIOP mean CTH.

(B) MODIS mean CTH.

FIGURE 4.3: Mean MODIS and CALIOP CTH [km] retrievals in the LTS-τ retrieval space for 2015 polar-day, where LTS is constructed at a 3-hourly temporal resolution and at a spatial resolution of 0.625 ° longitude ×0.5 ° latitude from the MERRA2 datasets. All pixels included contain single-layer clouds according to both instruments such that MODIS CTH is less than 2 km and CALIOP CTH is less than 1.2 km.

the mean CALIOP CTH (Fig. 4.3a) in those same bins. It also seems like CALIOP overestimates MODIS for low τ and low LTS bins. Otherwise, MODIS and CALIOP show broadly similar CTH climatologies in the LTS-τ retrieval space. To investigate the differences further, I calculated the mean CTH difference (MODIS − CALIOP) between the two plots.

The results quantifying the effect of τ and LTS on the mean CTH difference are shown in Fig. 4.4a using the MERRA2 dataset to create LTS and replicated in Fig. 4.5a using ERA5 to create LTS. Importantly, the CTH bias climatology in the LTS-τ space does not seem to depend on our choice of reanalysis dataset. Fig. 4.4b and 4.5b show the distribution of the total number of points used in the two respective graphs. Bins containing less than 50 points are not shown. There are two key features to notice in Fig. 4.4a. First, the CTH underestimation is largest when τ is small, and this underestimation seems to be slightly skewed towards low LTS values also. Second, there is a group of positive biases located in the upper left corner of the plot that extends to an LTS value of about 16 K before more negative bins are seen as LTS

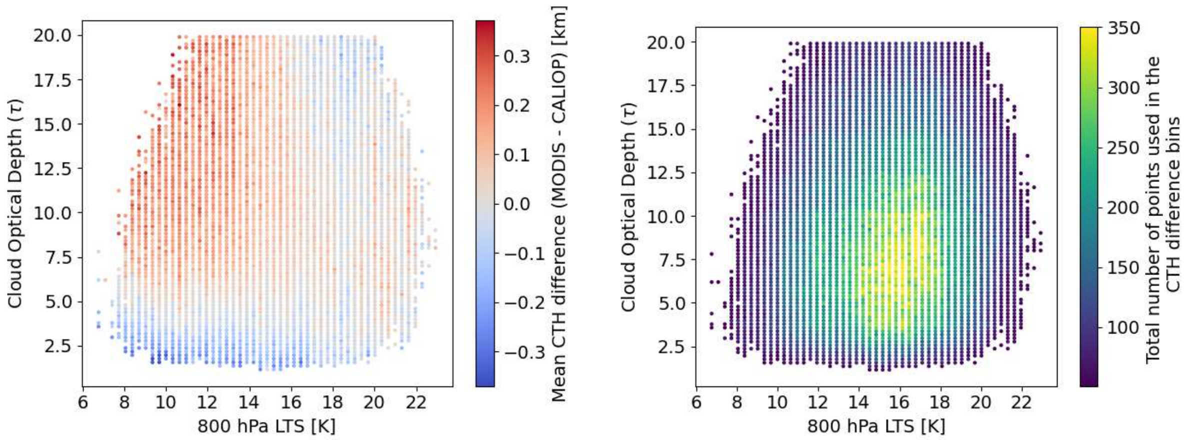

(A) Mean CTH difference in each bin. Bins centred on 0.10, 0.30 etc.τ and 1.15 K, 1.48 K etc. LTS.

(B) Total number of points in each bin. Bins centred on 0.10, 0.30 etc.τ and 1.15 K, 1.48 K etc. LTS.

FIGURE 4.4: Mean CTH difference and total number of points used grouped into 100×100 LTS–τ bins, where LTS is created with the reanalysis dataset MERRA2 and τ comes from the MODIS 1 km COT21 variable. A statistical limit is placed on each 2D bin such that the bins must contain a minimum of $n \geq 50$ points to be plotted, aiming to remove statistically insignificant bins. All pixels included contain single-layer clouds according to both instruments such that MODIS CTH is less than 2 km and CALIOP CTH is less than 1.2 km.

increases.

As per Hypothesis 1 (Section 2.1), a low τ value allows more radiation from the surface to reach the passive sensor. Meanwhile, a small LTS is an indicator that either none or a weaker temperature inversion is present, meaning that the TOA radiative influence by the surface is strong relative to the radiation emitted from the cloud. Hence underestimation increasing as τ decreases to smaller values and as LTS decreases to smaller values might be explained by our hypothesis described in Section 2.1. My results are corroborated by Fig. 4.5a, which also shows that the strength of underestimation is larger for low τ and LTS values using an alternative dataset (ERA5) to calculate 800 hPa LTS values. Importantly, it is worth highlighting that even for low τ and LTS the radiation from the surface does not necessarily dominate compared to the radiation from the cloud-top, but just that it has a larger influence. It is also worth highlighting that the cloud τ at the 2.1 μm wavelength is generally of a greater magnitude than that at the 11 μm wavelength (Wylie et al.,

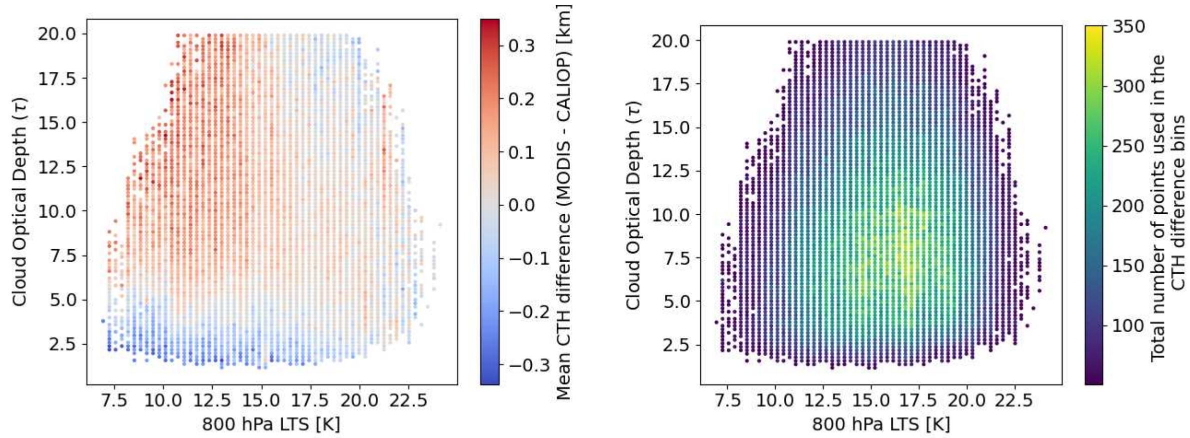

(A) Mean CTH difference in each bin. Bins centred on 0.10, 0.30 etc.τ and 0.27 K, 0.60 K etc. LTS.

(B) Total number of points in each bin. Bins centred on 0.10, 0.30 etc.τ and 0.27 K, 0.60 K etc. LTS.

FIGURE 4.5: Mean CTH difference and total number of points used, as in Fig. 4.4, but using ERA5 reanalysis data instead of MERRA2 to calculate LTS.

1995). However, the general pattern that underestimation of CTH by MODIS increases for low τ remains. More generally, the mean CTH difference (MODIS − CALIOP) for all data points included in Fig. 4.4 is 0.049 km with a standard deviation of 0.412 km, so in general MODIS overestimates CALIOP when CALIOP CTH is less than 1.2 km. However, the standard deviation around the mean overestimation is significant, and therefore includes many pixels where CTH is underestimated. This is suggests a significant improvement in MODIS C6 retrieved CTH compared to C5 where the CTH difference with CALIOP in the Arctic was 0.3 $\pm$ 1.2 km in August 2006 and 0.1 $\pm$ 1.7 km in February 2007 (Holz et al., 2008).

Interestingly, as can be seen in both Fig. 4.4b and 4.5b, most of the data points arise from more central LTS and τ values. Comparing this observation with Fig. 4.4a and 4.5a, this indicates that most data points occur in bins where a slight average overestimation occurs of a few tens to a few hundreds of metres. The mean value of the CTH difference (MODIS − CALIOP) for all data points is 0.049 km, so in general a slight average overestimation does occur. Importantly this mean difference is much smaller than the extreme values in the bottom left and upper left corners of Fig. 4.4 and Fig. 4.5, which could be explained given the relatively few data points that occur for low LTS values.

Fig. 4.6a and 4.6b show the standard deviation of the mean CTH difference values in each bin for Fig. 4.4a and 4.5a respectively. There is a larger spread in the biases for low LTS and higher τ compared to elsewhere. These are also the bins where MODIS tends to overestimate CTH. This could be because, as highlighted by Scott et al., 2020 (though this study did not include the Arctic region), strong inversions favour greater cloud opacity of low-level cloud cover by trapping moisture in the marine boundary layer. These thicker clouds may be easier for MODIS to identify and to detect the CTH of due to the decreased influence of radiation not arising from the cloud-top. It is important to note that the high standard deviation values of 0.55 km are not unique to our study, as Holz et al., 2008 found that MODIS C5 had a mean bias $\pm$ standard deviation compared to CALIOP (MODIS $-$ CALIOP) of 0.3 $\pm$ 1.2 km in August 2006 and of 0.1 $\pm$ 1.7 km in February 2007.

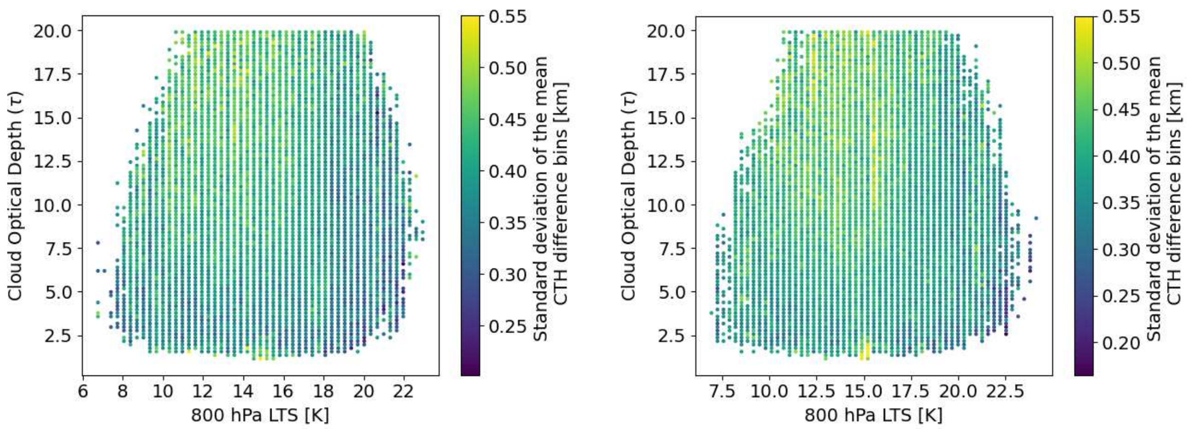

(A) Standard deviation of CTH difference values in each bin for Fig. 4.4a. Bins centred on 0.10, 0.30 etc.τ and 1.15 K, 1.48 K etc. LTS calculated from MERRA2.

(B) Standard deviation of CTH difference values in each bin for Fig. 4.5a. Bins centred on 0.10, 0.30 etc.τ and 1.15 K, 1.48 K etc. LTS calculated from ERA5.

FIGURE 4.6: Standard deviation of the mean CTH difference [km] (MODIS - CALIOP) per bin with the dataset grouped into 100 $\times$ 100 LTS–τ bins, where LTS is created with the reanalysis dataset ERA5 and MERRA2 and τ comes from the MODIS 1 km COT21 variable. Filtering as in Fig. 4.4.

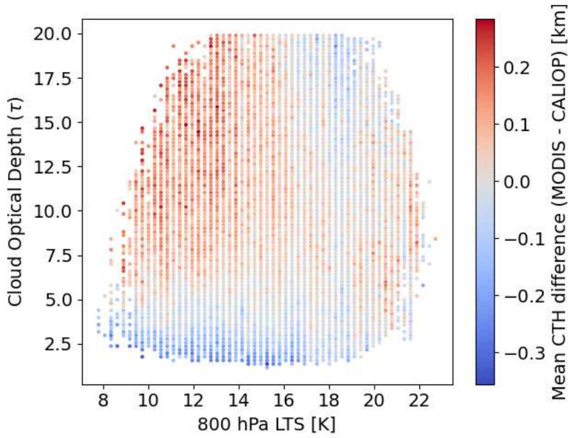

(A) Mean CTH difference in each bin. Bins centred on 0.10, 0.30 etc.τ and 1.15 K, 1.48 K etc. LTS according to MERRA2.

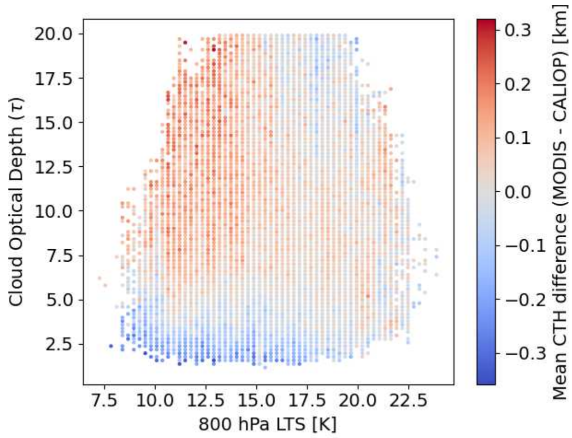

(B) Mean CTH difference in each bin. Bins centred on 0.10, 0.30 etc.τ and 1.15 K, 1.48 K etc. LTS according to ERA5.

FIGURE 4.7: Mean CTH difference (MODIS - CALIOP) per bin with the dataset grouped into 100×100 LTS–τ bins, where LTS is created with the reanalysis dataset ERA5 and MERRA2 and τ comes from the MODIS 1 km COT21 variable. Filtering as in Fig. 4.4 with pixels situated over land according to the AMSR-E sea-ice mask removed.

Regarding the bins where MODIS overestimates CALIOP as seen in both Fig. 4.4a and Fig. 4.5a, they seem to occur when τ is larger. Hence the underestimation effect of the surface could be masked since the surface radiation would be more attenuated as it passes through the cloud. Hence, as τ increases competing impacts could begin to dominate over the impact of the surface radiation. For example, at larger τ values the impact outlined by Hypothesis 2 (Section 2.2) could begin to dominate, since the effect of Hypothesis 1 becomes weaker. The lack of realistic sea-ice values in the modelled clear-sky BT could theoretically result in an overestimate of CTH when no inversion is present, which a low LTS would generally indicate. This hypothesis will be investigated further in Section. 4.3. However first, to further investigate those points for which an overestimate occurs, I recreated Figs. 4.4a and 4.5a again but removed pixels situated over land. Figure 4.7 shows the results of this surface-type-selective data processing.

As shown in Fig. 4.7, the visual pattern in the LTS-τ space does not change substantially when land points are removed. The widespread overestimation by MODIS seen at high τ and low LTS remains, and the generally higher underestimation at low LTS and low τ remains. This suggests that the cause of this overestimation (and also underestimation) is at least in part linked to LTS. However, the mean CTH difference (MODIS - CALIOP) decreased to 0.027 km with a standard deviation of 0.394 km when land points were removed (compared to 0.049km km with a standard deviation of 0.412 km with land points included) suggesting that MODIS underestimates more over ocean regions in the Arctic (although not everywhere, as is evident from Fig. 4.7). To investigate the positive vs. negative biases further, I plotted the aggregated mean CTH difference projection for 2015 polar-day for low-level, single-layer clouds in the Arctic (Fig. 4.8).

Figure 4.8 shows that for regions at higher latitudes and over ocean, MODIS tends to underestimate CALIOP by a few tens to a few hundred meters. In contrast, there is larger overestimation for points overlying ocean locations at lower latitudes, and over land surfaces. This could be because the higher latitude regions over ocean tend to have a higher LTS according to Fig. 4.2, suggesting that the geographic shift in the Barents sea, from a general overestimate to a more neutral or even underestimate as latitude increases, might be tied to an increased LTS. Figure 4.7 also shows that overestimation at τ greater than 5.0 decreases as LTS increases. However, it should be noted that these ocean regions of higher LTS might generally be expected to have higher sea-ice coverage that is associated with a larger LTS. Sea-ice surfaces generally have lower surface temperatures due to the continuous loss of heat through radiant emission, and the sea-ice acts as a thermal insulator limiting heat conduction from the underlying ocean water, causing low-lying temperature inversions and leading to higher LTS (Stramler et al., 2011; Uttal et al., 2002). The increased sea-ice coverage could therefore be the cause of the increased underestimation of MODIS CTH at higher latitudes over ocean regions. Sea-ice generally has a higher surface reflectance compared to open ocean surfaces (Warren & Brandt, 2008), which would lead to an increase in the reflected downwelling radiation. This could increase the

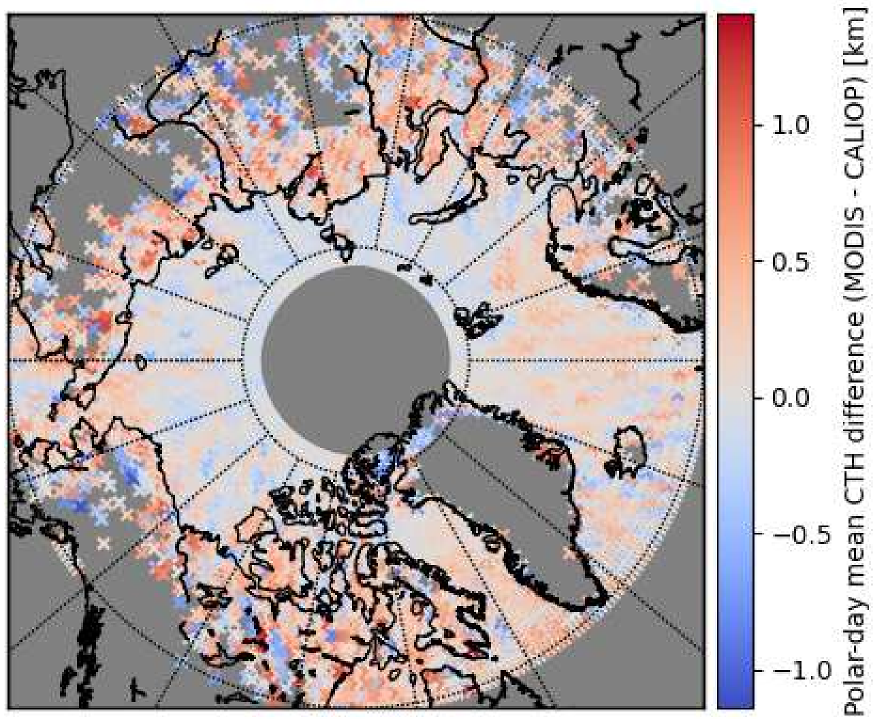

FIGURE 4.8: Aggregated mean CTH difference (MODIS - CALIOP) projected onto the Arctic region (latitudes greater that 60 $^\circ N$), calculated over 2015 polar-day. There are 30 latitude × 360 longitude bins. Bins are centred on $-177.5\ ^\circ E$, $-176.5\ ^\circ E$ etc. longitude and 60.5 $^\circ N$, 61.5 $^\circ N$ etc. latitude. Data points filtered as for Fig. 4.4.

intensity of the radiation detected at the TOA and therefore increase the measured cloud-top $BT_{11\ \mu m}$. This in turn could reduce the $BT_{11\ \mu m}$ difference between the PFAAST modelled clear-sky scenario and MODIS measured cloud-top BT assuming no low-level temperature inversion was present, leading to an underestimate in the MODIS CTH retrieval. Interestingly, Holz et al., 2008 showed that in Arctic regions the overestimation of CTH by MODIS compared to CALIOP was less in February 2007 than in August 2006 for a resolution of 1 km. This could corroborate our finding that MODIS tends to underestimate more over sea-ice surfaces, since February would generally imply a higher sea-ice regional coverage than August. Though, it is important to note that the study by Holz et al., 2008 compared the MODIS C5

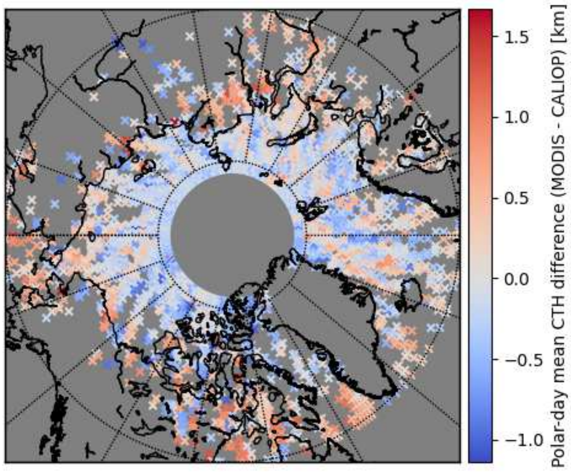

(A) April 2015.

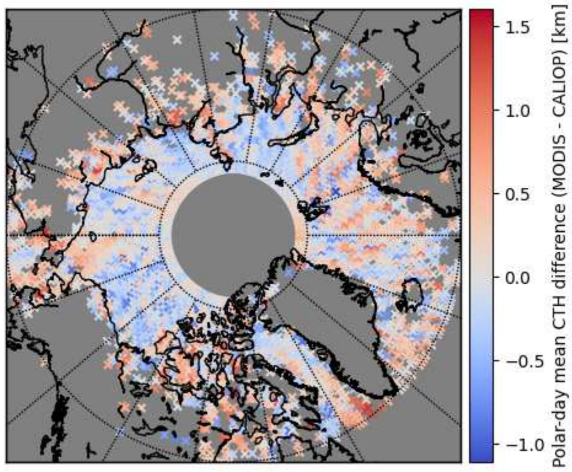

(B) August 2015.

FIGURE 4.9: Aggregated mean CTH difference (MODIS - CALIOP) for two distinct months projected onto the Arctic region (latitudes greater that 60 $^\circ N$), calculated for (A) April and (B) August 2015. There are 30 latitude $\times$ 360 longitude bins. Bins are centred on $-177.5\ ^\circ E$, $-176.5\ ^\circ E$ etc.longitude and 60.5 $^\circ N$, 61.5 $^\circ N$ etc.latitude. Data filtered as for Fig. 4.4.

product to CALIOP, whereas I am analysing MODIS C6, for which the CTH retrieval technique has been changed from C5, as discussed in Section . However, both C5 and C6 rely on measured $BT_{11\ \mu m}$, which could explain the correlation.

To compare more closely to results from Holz et al., 2008 we projected the mean CTH difference for April and August 2015 (since we did not have access to data from February or 2007). The results can be seen in Fig. 4.9. As can be seen, the negative mean biases extend to much lower latitudes in the month of April compared to the month of August. This could be due to sea-ice concentration being higher at lower latitudes in April than in August. The increase in points with an average underestimation might also align with results by Holz et al., 2008 that show that MODIS overestimates CTH less compared to CALIOP in winter months than in summer months. Moreover, August 2015 has a mean CTH difference (MODIS - CALIOP) 0.036 $\pm$ 0.424km, whereas for April 2015 this difference decreases to $-0.006 \pm 0.428km$.

Our projections suggest that CTH bias could be tied to sea-ice fractional coverage underlying the cloud since underestimation seems to increase in the winter months. However, it should again be highlighted that the spatial pattern of Fig. 4.8 is similar to the spatial pattern of the mean aggregated LTS in Fig. 4.2. In the Barents sea, we see a clear increase in LTS as latitude increases which is visually similar to the line between blue and red points in Fig. 4.8. This suggests that high LTS is more associated with an increased underestimate. However there are also some differences in the spatial patterns between the Fig. 4.2 and Fig. 4.8, such as Baffin Bay which shows neutral to positive CTH bias but a generally higher LTS. These discrepancies might be explained since for strong non-linear temperature changes in the atmosphere, inversion strength was not directly tied to LTS (Wood & Bretherton, 2006). Hence, there may be some points where non-linear θ gradients impact the temperature of the cloud-top in a way that is not adequately represented by LTS. For example, I have calculated LTS using an elevated altitude pressure level of 800 hPa, however the cloud may sit at a higher pressure level, and hence have a different potential temperature difference with the 2 m level than indicated by LTS. Therefore, while the cloud may sit within a pixel with a higher LTS, the cloud-top temperature could be much lower or higher than $T_{800\ hPa}$ and therefore the relative influence of the surface much higher or lower, respectively. Therefore, these discrepancies between Fig. 4.8 and Fig. 4.2 might further support our findings that while CTH bias is tied to LTS it also seems to depend on other factors such as sea-ice coverage.

In general, our findings suggest that the combination of low LTS and low τ plays a role in causing MODIS CTH to be underestimated, while low LTS and higher τ seems to be associated with an overestimation. However the higher standard deviation seen in Fig. 4.6b and Fig. 4.6a suggest that the mean CTH errors result from an averaging of much larger errors in individual retrievals. Moreover Fig. 4.8 suggests that the MODIS CTH bias has a high surface type dependence (for example open-ocean vs. sea-ice surfaces), which could explain any CTH bias patterns seen in the LTS-τ

space since Fig. 4.2 shows that LTS also has a high geographic dependence. More specifically, Fig. 4.8 shows that underestimated points generally come from regions that would generally have higher sea-ice concentration. This observation is further verified by Fig. 4.9 which shows that underestimation increases in winter months compared to summer months.

4.3 Hypothesis 2 Results

4.3.1 CTH Replication

Fig. 4.10 shows the results of my CTH replication where I used Eqn. 2.1 to replicate the MODIS CTH algorithm, for pixels where a single-layer and low-lying (CTH $\leq$ 2 km) cloud, according to both instruments, is detected over ocean, using the CRTM model in place of the PFAAST model to calculate clear-sky BT. From Fig. 4.10a and 4.10b, the mean calculated CTH (i.e. y axis) is 0.731 km and 0.652 km respectively.

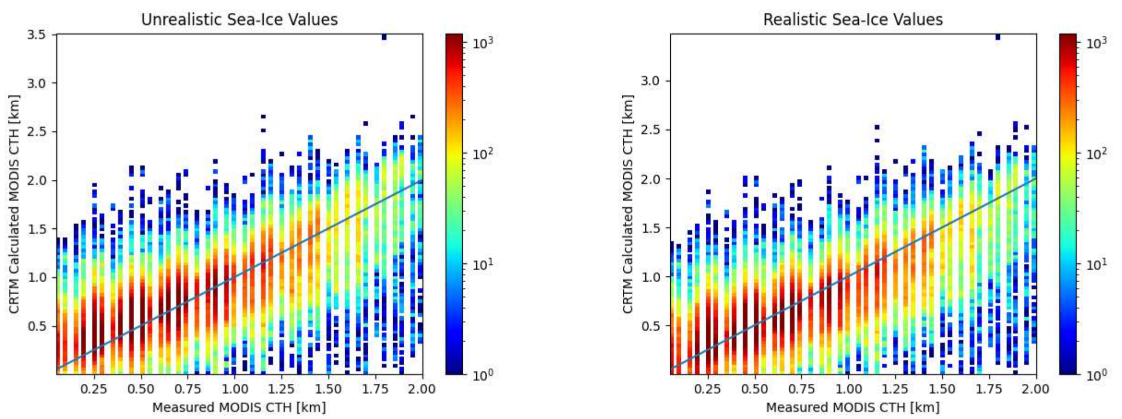

(A) Unrealistic sea-ice fractional cover values (0 %).

(B) Realistic sea-ice fractional cover values from the collocated AMSR-E sea-ice product.

FIGURE 4.10: Density plot of MODIS measured CTH and CTH calculated using the CRTM model (in place of the PFAAST model) to calculate clear-sky BT, where the blue lines represent the 1:1 markers and the color bar the density of points. Data is filtered to only include single-layer low-level ($0-2$ km) clouds north of 60 $^\circ N$ for points where fractional sea-ice cover is greater than 0 % for polar-day 2015.

TABLE 4.2: Mean difference (CRTM CTH - Measured CTH) [km] statistics for clouds in different altitude layers according to the MODIS CTH retrieval method for Fig. 4.10. Δ represents: column 3 − column 2.

	Unrealistic sea-ice value	AMSR-E sea-ice value	Δ
All 0–2 *km* clouds	0.04	-0.04	-0.08
0–1 *km* clouds	0.09	0.01	-0.08
1–2 *km* clouds	-0.13	-0.22	-0.09

First, the CRTM method is replicating MODIS CTH retrievals well, however there is a spread from a 1:1 match (blue line). This could be explained since I am using a different radiative transfer model and atmospheric property values to calculate $BT_{11\ \mu m}$(CRTM) values than MODIS uses. Interestingly, my replication of CTH underestimates compared to the measured values more for points higher than 1 *km*. For clouds within the 0–1 *km* range the CRTM model slightly overestimates the measured values, whereas for clouds within the 1–2 *km* range the CRTM model seems to underestimate the measured values more. This distinction between the upper and lower levels of the 0–2 *km* range for CTH biases can be seen in Table 4.2, which lists the mean difference between my replicated CTH algorithm and MODIS' measured CTH. It should be highlighted that there are more points in the 0–1 *km* range, so in general the model slightly overestimates the measured values. One potential future improvement in the CTH replication could be the use of more realistic H_2O concentration and O_3 concentration values, which were kept constant throughout my CTH calculations in the CRTM model. This would more accurately represent the atmospheric conditions of each cloudy pixel and the PFAAST model itself, which uses water vapour and ozone profiles from GDAS (Baum et al., 2012).

Table 4.2 also shows that the 1–2 *km* level shows a greater decrease in CTH between the unrealistic and realistic scenario, represented by Δ. This indicates that the use of realistic sea-ice values lowers (compared to the unrealistic scenario) $BT_{11\ \mu m}$(CRTM) more for higher clouds. The difference in the two layers could be because the higher clouds are more likely to sit over higher sea-ice values. Open oceans tend to have higher surface temperatures, stronger evaporation, and more lower tropospheric moisture in the warmer summer months, promoting more low-level cloud amount since the surface is more coupled to the cloud layer enhancing surface turbulent moisture fluxes to the atmosphere (Yu et al., 2019). It is therefore possible that many of the pixels falling in the 0–1 km range exist over lower fractional sea-ice cover surfaces than the 1–2 km pixels. This would mean that the difference in surface emissivity between the two scenarios would be lower for the 1–2 km layer and therefore the magnitude of the impact on $BT_{11\ \mu m}$(CRTM) lower. However it should be noted that the magnitude of Δ is relatively similar for the two layers so the difference could be insignificant.

Second, the use of realistic sea-ice values (Fig. 4.10b) lowers the average replicated CTH values by 0.079 km compared to Fig. 4.10a. This aligns with the hypothesis as described in Section 2.2, particularly given that during polar-day temperature inversions are generally either weaker, at an elevated altitude, or do not exit (Graversen & Wang, 2009) such that the temperature of the cloud-top is generally cooler than the surface. In the unrealistic scenario 0 % sea-ice surface cover is used in the CRTM model underlying the cloud, leading to an overestimate of the calculated $BT_{11\ \mu m}$(CRTM) and hence an average overestimate in the numerator of Eqn. 2.1, as discussed in Section 2.2. This suggests that the use of unrealistic sea-ice coverage values in the Arctic leads to a positive CTH bias, and that replacing these values with locally accurate sea-ice values could reduce the MODIS measured CTH. However, it is worth highlighting that the difference of 0.079 km is relatively small compared to the average CTH (unrealsitic scenario) of 0.731 km, suggesting that the impact of emissivity differences between open-ocean and sea-ice is relatively small. This could be explained given the relatively small difference in emissivity between the two surface types, as illustrated in Fig. 2.1.

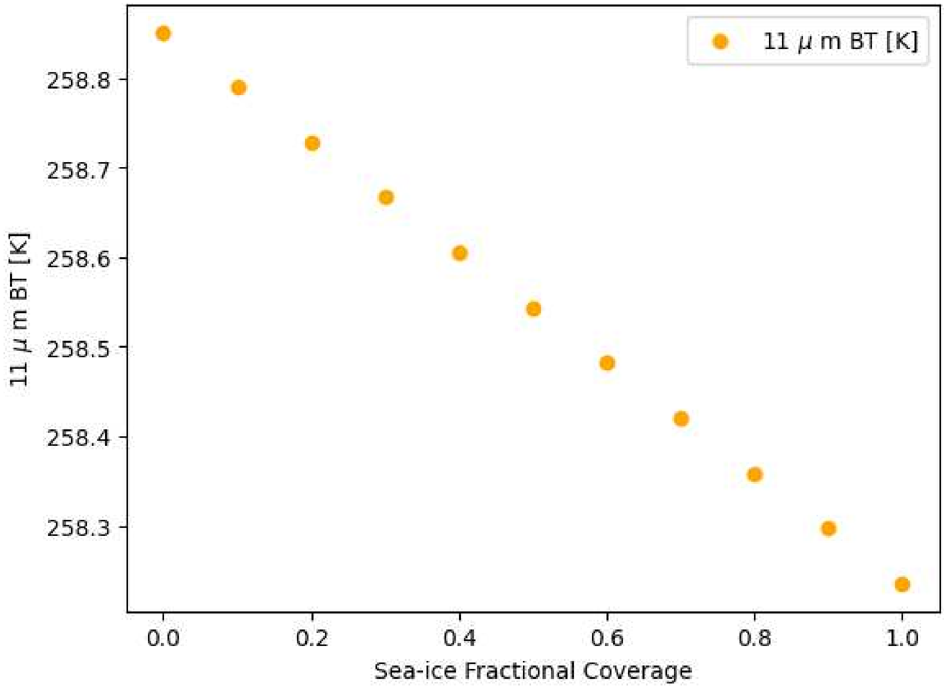

FIGURE 4.11: CRTM simulated variation of $BT_{11\ \mu m}$ with sea-ice fractional coverage. Atmospheric conditions obtained from MERRA2 data for 5^{th} March 2015 at approximately 20:00 UTC, at a longitude of $-116.83\ ^\circ\ E$ and latitude of $69.22\ ^\circ\ N$. Note, there is a small temperature range on the y-axis of approximately 0.62 K.

To verify this expectation that surface emissivity changes should have a small impact on CTH retrievals, I plot the variation of $BT_{11\ \mu m}$ with sea-ice fractional coverage as simulated by the CRTM model. Figure 4.11 shows the results. The surface temperature was kept constant at 260 K and the CRTM model was run for clear-sky conditions over open-ocean in the Arctic at a longitude of $-116.83\ ^\circ E$ and latitude of $69.22\ ^\circ N$, where the atmospheric conditions (such as atmospheric temperature) were obtained from MERRA2 and kept constant throughout the run. The atmospheric conditions were obtained from MERRA2 data for 5^{th} March 2015. As can be seen $BT_{11\ \mu m}$ decreases linearly with a corresponding increase in sea-ice fractional coverage. As discussed in Section 2.2 this is expected due to the decreased emissivity of sea-ice compared to open-ocean. However, it is important to note that the magnitude of the change is relatively small at approximately 0.62 K between 0 % and 100 % fractional coverage. This is expected due to the relatively small emissivity difference between sea-ice and open-ocean as illustrated in Fig. 2.1. Moreover, given the attenuation of radiation emitted from the surface as it passes through the atmosphere and the reflection of downwelling radiation at the surface, the impact of surface emissivity could be reduced even further. This likely explains the small change in mean CRTM calculated CTH seen in Fig. 4.10.

4.3.2 BTLR Replication

The results for the replicated BTLR computation are shown in Fig. 4.12. Since I am only running the CRTM model for data points where the underlying surface has a sea-ice fractional coverage greater than 0 %, there are few data points at latitudes lower than 70 $^{\circ}N$, and none over land. However, it is clear that there is a strong longitudinal variance of the average apparent BTLR readings even in the unrealistic sea-ice scenario. This suggests that accurate local apparent BTLR values largely depend on properties other than surface emissivity. This is likely explained given that factors other than surface emissivity can affect the temperature structure of the atmosphere, which can also vary longitudinally. For example, in the CRTM model I used local atmospheric temperature and pressure values from the MERRA2 dataset, which would likely have a direct impact on the calculated BTLR values. However, importantly what Fig. 4.12 shows is that the zonal averaging of apparent BTLR values is not accurate in the Arctic.

Interestingly, when zonally averaging these apparent BTLR values and plotting these average values against latitudinal coordinates on the x-axis, the unrealistic and realistic sea-ice fractional cover runs produce similar visual patterns, as is shown in Fig. 4.13a and 4.13b respectively. This is likely because the BTLR is dominated by the vertical temperature structure of the atmosphere which was kept constant between the two runs. However, the average latitudinal apparent BTLR value drops from 7.62 $K\ km^{-1}$ to 6.75 $K\ km^{-1}$ between unrealistic (Fig. 4.13a) and realistic sea-ice

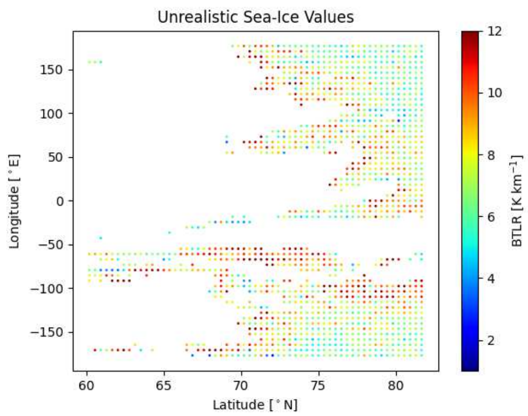

(A) Unrealistic sea-ice fractional cover values (0 %).

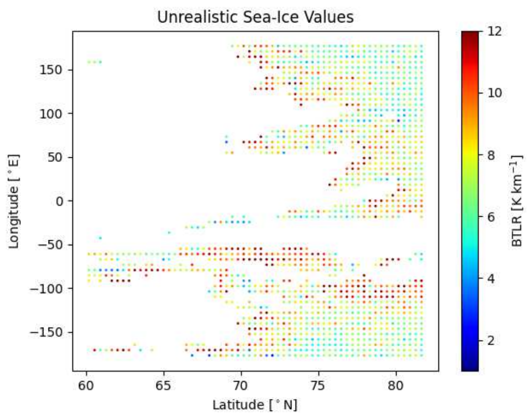

(B) Realistic sea-ice fractional cover values from the collocated AMSR-E sea-ice product.

FIGURE 4.12: A distribution of CRTM replicated BTLR values averaged into 60 latitude $\times$ 60 longitude bins. Bins are centred on $-177.00\ ^\circ E$, $-171.00\ ^\circ E$ etc.longitude and $60.19\ ^\circ N$, $60.56\ ^\circ N$ etc.latitude. Data filtered to only include single-layer low-level (CTH $\leq 2\ km$) clouds north of $60\ ^\circ N$ for points where fractional sea-ice cover is greater than 0 % for polar-day 2015.

(Fig. 4.13b) values respectively. Like the CTH plots (see Fig. 4.10), the only change between the runs was that realistic sea-ice fractional cover values have been used in the calculation of $BT_{11\ \mu m}$(CRTM). As discussed in Section 2.2, this decrease is likely explained by the impact of emissivity differences between open-ocean and sea-ice on $BT_{11\ \mu m}$(CRTM).

It should be noted that for lower latitudes there are fewer points to analyze. This makes physical sense since I am evaluating points where sea-ice fraction is greater than 0 % to analyse the effect of using non-zero, physically realistic sea-ice fractional cover values. However, the general pattern that using realistic sea-ice fractional cover values over sea-ice points lowers the CRTM calculated apparent BTLR remains. This suggests that the use of unrealistic sea-ice coverage values in the Arctic leads to a positive BTLR bias, and that replacing these values with locally accurate sea-ice values could reduce the magnitude of the apparent BTLR values used in the denominator of Eqn. 2.1. It should be noted that the magnitude of the effect of the surface emissivity change on the zonal average of apparent BTLR is small compared to the geographic

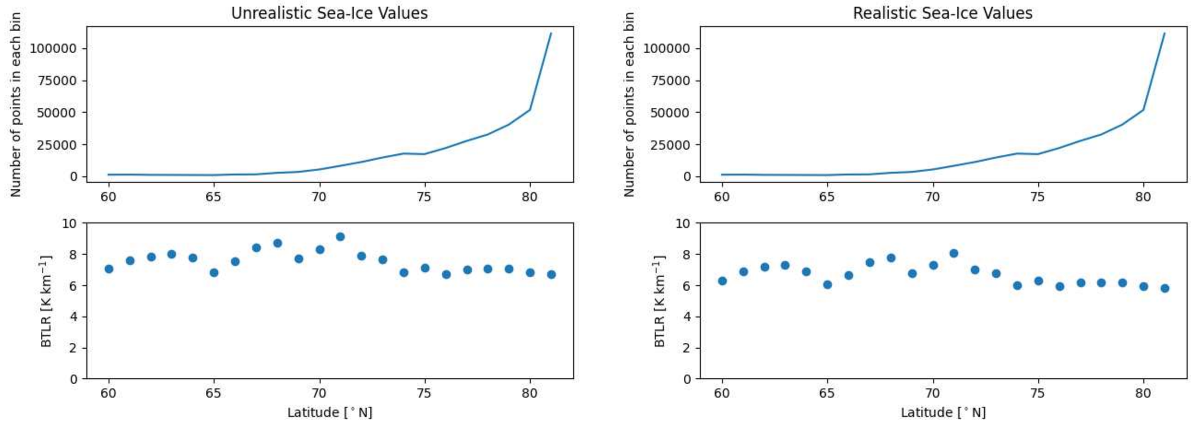

(A) Unrealistic sea-ice fractional cover values (0 %).

(B) Realistic sea-ice fractional cover values from the collocated AMSR-E sea-ice product.

FIGURE 4.13: A distribution of the CRTM replicated BTLR values averaged into 22 latitude bins. Bins are centred on 60.5 $^\circ N$, 61.5 $^\circ N$ etc.latitude. Data filtered to only include single-layer low-level clouds north of 60 $^\circ N$ for points where fractional sea-ice cover is greater than 0 % for polar-day 2015.

variation shown in Fig. 4.12. As with the CTH replication (discussed in Section 4.3.1), this is likely due to the small emissivity difference between open-ocean and sea-ice in the 11 μm wavelength.

Importantly, further validation was warranted to evaluate if the CRTM calculated apparent BTLR values were physical, particularly for values greater than the dry adiabatic temperature lapse rate ($\sim$ 9.8 $K\ km^{-1}$) as seen in Fig. 4.12. To verify the relationship between the apparent BTLR and temperature lapse rate, I first plot the temperature lapse rate against our CRTM calculated BTLR values, shown in Fig. 4.14. The temperature lapse rate was calculated against the 900 hPa level as it is approximately near the mean CTH level in the $0-2$ km range of 0.934 km according to CALIOP. For example, using an example mean temperature between the 1000 hPa to 900 hPa levels in the Arctic obtained from the MERRA2 dataset, equal to 269 K, as an approximation for the virtual temperature of the level, we can use the hypsometric equation to calculate a surface-900 hPa thickness of approximately 1000 m, which is approximately the same as the mean CALIOP CTH. Since MODIS restricts the

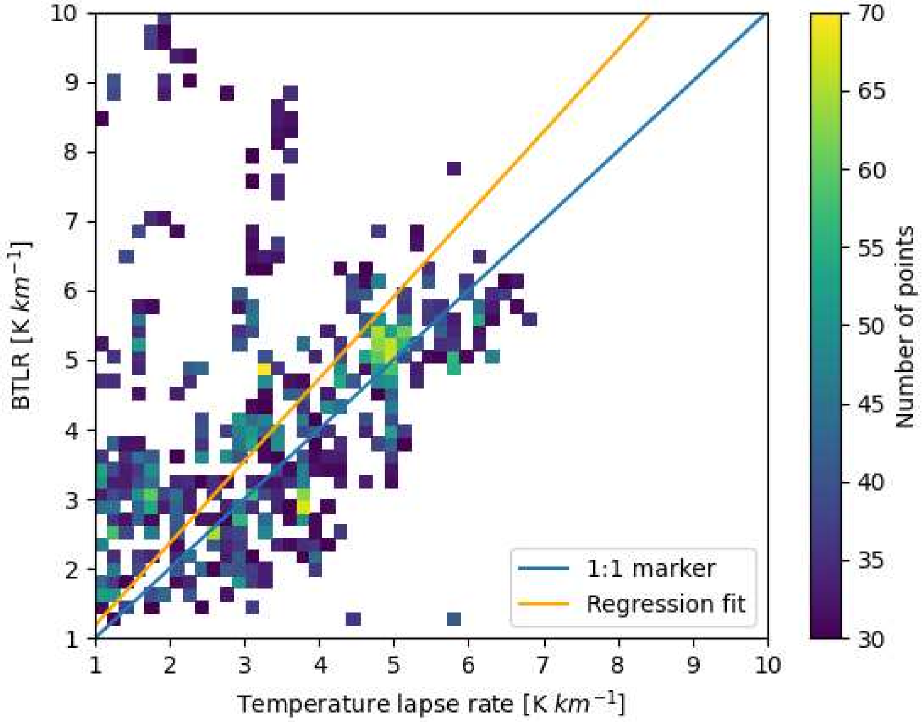

FIGURE 4.14: 2D histogram of lapse rate, calculated between the surface temperature and 900 hPa atmospheric temperature, against CRTM calculated BTLR lapse rate. There are 50 $\times$ 50 histogram bins between 1 K and 10 K, centred on 1.09 $K\ km^{-1}$, 1.27 $K\ km^{-1}$ etc. BTLR and temperature lapse rate, with bins that contain less than 30 points not shown. The orange line shows the regression fit and the blue the 1:1 marker. Data were selected such that only every 6^{th} day (starting from 1^{st} March 2015) of 2015 polar-day was included.

apparent BTLR values a maximum of 10 $K\ km^{-1}$ post-processing (Baum et al., 2012), I also restricted our replication of BTLR to the same values. A minimum statistical limit of 30 was placed such that bins with less points are not shown to remove statistically insignificant bins. The data was selected such that only every 6^{th} day (starting from 1^{st} March 2015) of the 2015 polar-day was included. A regression fit calculated using the same technique as Fig. 4.1a is shown in orange. The equation governing that fit is $y = 1.18 \times x$ where y is the y-axis (BTLR [$K\ km^{-1}$]) and x is the x-axis (temperature lapse rate [$K\ km^{-1}$]). As can be seen through the regression fit, the two generally increase together at a gradient steeper than a 1:1 relationship. This is consistent with our earlier findings as it suggests that some BTLR values seem to be overestimated. It should also be noted that the mean lapse rate of 3.8 $K\ km^{-1}$ is slightly below literature values of the lapse rate in the Arctic of 4.5 $K\ km^{-1}$ (Mokhov & Akperov, 2006). In the Arctic, particularly over sea-ice surfaces, temperature inversions near the surface are common and could lead to a lower lapse rate near the surface since the 900 hPa temperature would be closer to the surface temperature in these cases. This could explain the lower temperature lapse rate, and therefore lower apparent BTLR, values seen in Fig. 4.14.

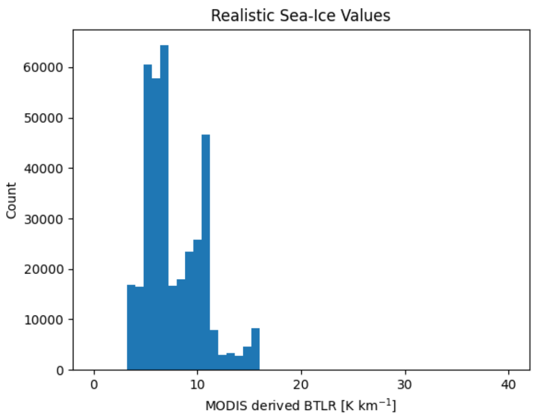

(A) A distribution of BTLR values calculated using the polynomial parametization and associated coefficients obtained from Baum et al., 2012, and calculated utilising MODIS latitude values for cloudy-sky pixels not over land for polar-day 2015.

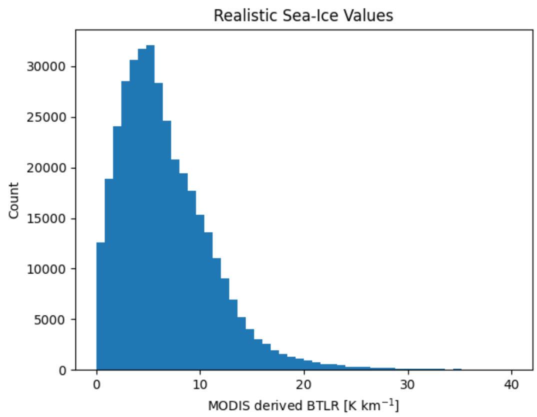

(B) A distribution of BTLR values calculated using our CRTM replication of Eqn. 1.1 for cloudy-sky pixels not over land for polar-day 2015.

FIGURE 4.15

However, in general there seem to be a significant number of overestimated BTLR values that need to be explained. To investigate these overestimates further, we first needed to compare the validity of the zonally averaged BTLR values calculated from CRTM to those obtained from the literature. To do this, I took the BTLR values calculated with Eqn. 1.1 using the CRTM model with inputs of MODIS retrieved BT, MERRA2 data, and CALIOP CTH using realistic sea-ice values. I then used the latitude of each MODIS pixel used in the CRTM replication of BTLR, along with the coefficient values and polynomial parametization for each month obtained from Baum et al., 2012, to calculate the apparent BTLR according to the literature (and actually used by the MODIS CTH algorithm). The distribution of the BTLR values obtained from the CRTM replication and the literature can be seen in Fig. 4.15. As with Fig. 4.12, this was only done for cloudy pixels (single-layer and low-level according to both instruments) not over land.

The mean of Fig. 4.15b is 6.68 $K\ km^{-1}$ and of Fig. 4.15a is 7.69 $K\ km^{-1}$. Therefore, it seems that the magnitude of the literature values is approximately equivalent to our CRTM calculated values, if not slightly higher. This could be because we used realistic sea-ice values in our CRTM computation of BTLR seen in Fig. 4.15b. Moreover, for our CRTM replication of BTLR, 19.8 % of points are over 10 $K\ km^{-1}$, whereas for the literature values 23.8 % of points are over 10 $K\ km^{-1}$, which is greater than the post-processing cut-off used by the MODIS instrument (Baum et al., 2012). Importantly, both plots use Eqn. 1.1 to calculate BTLR, though Fig. 4.15a has both zonally and monthly averaged its values (Baum et al., 2012), and also uses the PFAAST model in place of the CRTM model. This suggests that the methodology used to calculate BTLR by MODIS needs to be investigated further, since both our replication of BTLR and the literature BTLR values seem to be significantly higher than the actual temperature lapse rate in the Arctic according to MERRA2 (see Fig. 4.14).

To verify our extraction of the apparent BTLR values from the literature, I used the coefficients from Table 3.3 and polynomial parametization from Baum et al., 2012 to show the zonal variation of BTLR for August, and also for all months in the polar-day using the coefficients from Baum et al., 2012. The results for August are shown in Fig. 4.16 as the brown line and match the expected literature plot. More interestingly, however, is that the higher BTLR values seem to be coming from March, April, and May at higher latitudes. This suggests that the methodology and instruments used in Eqn. 1.1 might overestimate the apparent BTLR (compared to the typical temperature lapse rate values seen in Fig. 4.14) more in winter months than in summer months, and at higher latitudes. There could be several reasons for this. First, the methodology

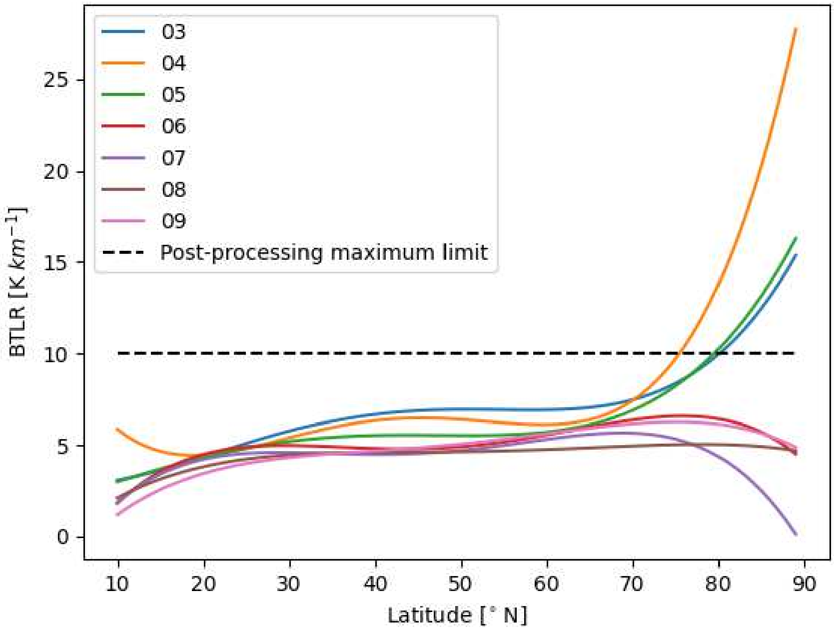

FIGURE 4.16: Zonal averages of BTLR polar-day months calculated and plotted using polynomial parameterization (described in Eqn. 3.8) and associated coefficients by Baum et al., 2012. The legend contains the months of the year (i.e. 03 = March, 04 = April). The dashed line represents the maximum limit applied in post-processing to BTLR by MODIS (Baum et al., 2012).

could overestimate in the presence of low-lying temperature inversions, which are particularly common in the winter (Graversen & Wang, 2009). Alternatively, it could be that the methodology struggles over sea-ice surfaces.

To investigate the apparent BTLR calculations further, we broke down the components of Eqn. 1.1 further. Throughout this thesis we are taking CALIOP as the truth, so we assume that the error is likely arising within the numerator of Eqn. 1.1. We verified our CRTM calculation of $BT_{11\ \mu m}$(CRTM) by plotting a probability distribution function of it against the collocated surface temperature used as the surface temperature input into the CRTM model (obtained from the MERRA2 dataset). Then, we repeated the process comparing our CRTM calculation of $BT_{11\ \mu m}$(CRTM) with collocated MODIS $BT_{11\ \mu m}$(MODIS) retrievals. These two plots were done for every 10^{th} clear-sky pixel for every 12^{th} day of the polar-day year starting at 1^{st} March to save computation time. The probability distribution functions, and the corresponding linear regression lines, were calculated as for Fig. 4.1a. The results are shown in Fig. 4.17a and Fig. 4.17b, respectively.

Two observations are clear. First, the CRTM model is replicating clear-sky conditions well in comparison to the inputted surface temperature. The orange line in Fig. 4.17a shows the regression fit, calculated using the same technique as for Fig. 4.1a, described by $y = 1.02 \times x - 6.77$, and the black line the 1:1 identity line. As can be seen, the two show a similar gradient, suggesting that the CRTM clear-sky BT is closely tied to the surface temperature inputted into the model – as we would expect. The gradient of the regression line also confirms that there appears to be a linear relationship between surface temperature and CRTM determined surface BT, with the values of roughly the correct magnitude. The non-zero y-intercept due to the fact that the gradient is slightly larger than 1.0. This suggests that the clear-sky BT variable in our replication of Eqn. 1.1 is functioning correctly.

Second, the CRTM modelled clear-sky BTs are generally larger than the MODIS measured clear-sky BTs. The slope of regression fit A in Fig. 4.17b, described by $y = 0.81 \times x + 52.57$, is shallower than the 1:1 line shown in black. If we force the regression fit to have a gradient of 1.0, it is described by regression fit B. This dashed orange line is described by the equation $y = x + 4.17$. These two lines indicate that discrepancy between the MODIS retrieved BT and the CRTM model gets worse for smaller MODIS measured BT values, and generally increases at a gradient slightly smaller than that of a linear relationship. More generally, it suggests that our CRTM model is overestimating BT retrievals in comparison to MODIS retrievals. This could explain the overestimation seen in our replication of BTLR compared to temperature lapse rate (Fig. 4.14). If the modelled clear-sky BT was too large when we replicated Eqn. 1.1, it could lead to an overestimated BT difference from the MODIS measured cloud-top BT, if a temperature inversion was not present. Since the CRTM model

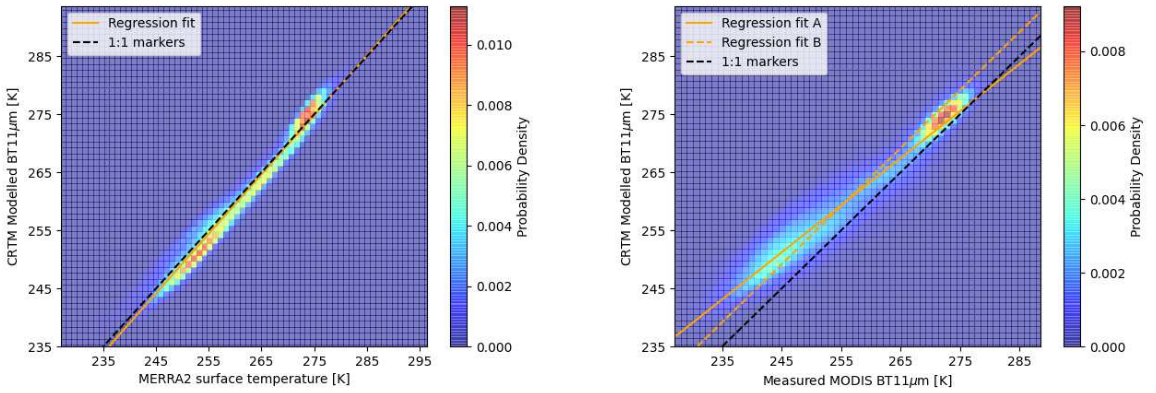

(A) Clear-sky CRTM BT compared to MERRA2 surface temperature. The probability distribution calculation was calculated using 70 $\times$ 70 bins centred on 224.5 K, 225.5 K etc. MERRA2 surface temperature and $BT_{11\ \mu m}$(CRTM).

(B) Clear-sky CRTM BT compared to pertaining MODIS retrieved BT. The probability distribution calculation was calculated for 70 $\times$ 70 bins centred on 227.5 K, 227.5 K etc. $BT_{11\ \mu m}$(MODIS) and $BT_{11\ \mu m}$(CRTM).

FIGURE 4.17: Clear-sky $BT_{11\ \mu m}$(CRTM) compared to collocated MERRA2 surface temperature and collocated MODIS retrieved $BT_{11\ \mu m}$(MODIS) for every 10^{th} pixel of every 12^{th} day of the polar-day, starting at 1^{st} March 2015. Data were also filtered such that a pixel was clear-sky according to both MODIS and CALIOP, and that the pixel was located over sea-ice surfaces according to the collocated AMSR-E data.

seems to be performing as expected in relation to the inputted surface temperature, this suggests that the discrepancy is due to discrepancies between MERRA2 surface temperature and the actual surface temperature impacting the satellite radiance measurement, or, less likely, a MODIS calibration issue.

The literature suggests that surface temperatures need to be atmospherically corrected in the model to be used in MODIS CTH calculations (Menzel et al., 2008), and we could speculate that such a correction to our CRTM model input could reduce the BT bias shown in Fig. 4.17. Moreover, the literature suggests that a radiance bias adjustment needs to be incorporated to correct for differences between model-derived and measured TOA radiances (Baum et al., 2012). Though the literature suggests this adjustment was applied to radiances used in the CO_2-slicing height retrieval method, it is not clear how such adjustments affect the computation of apparent BTLR in Eqn. 1.1 or if they also might need to be implemented for low-level clouds.

In general, our results suggest that a deeper investigation into the accuracy of MODIS retrieved BT in the Arctic is needed to further improve the apparent BTLR and CTH algorithms and to reduce number of unphysical BTLR values. One such avenue could be investigating more specifically where the high BTLR and low lapse rate points seen in Fig. 4.14 are arising from. For instance, Fig. 4.16 suggests that such instances could be occurring over particular surface types such as sea-ice, which would explain why they seem to primarily arise in March, April, and May, according to the literature. Alternatively, they could be arising in the presence of low-level temperature inversions, which may occur more frequently over sea-ice conditions in the winter months (while my analysis is restricted to the polar-day season).

A limitation of our analysis is that it was beyond the scope of this thesis to analyse the performance of the CRTM model in cloudy-sky conditions in comparison to MODIS retrieved BT due to substantial computational costs and limited time available. To do this, one could use the CALIOP cloud profile to determine cloud-top height and cloud-base height, therefore obtaining a measure of cloud physical thickness. Then, this could be used in conjunction with CALIOP's cloud optical depth retrievals to obtain the liquid water path of the cloud, as described by the relationship in Brenguier et al., 2011. One might also need an estimate of the total cloud droplet number concentration. This liquid water path could then be used to obtain the liquid water content of the cloud. Alongside a measure of effective radius, that could be obtained from the MYD06 MODIS product (described in Table 3.1), this liquid water content could then be input into the CRTM model as the cloud structure component (Delst et al., 2020). Alongside MERRA2 temperature data, CRTM could then be used to simulate TOA radiances in the 11 μm range, which would then support a realistic estimate of the cloud-top BT as measured by MODIS. These simulated cloudy-sky BTs could then be compared to actual MODIS retrieved BTs, which would allow us to analyse any biases in the MODIS cloud-top BT compared to the CRTM model. Moreover, such simulations could be run over various realistic low-level clouds situated at different heights and over different surfaces. This would provide information on the expected variability in TOA radiances. Due to computational constraints it was beyond the scope of the thesis to investigate this cloudy-sky scenario via extensive simulation experiments, but such an investigation would be a valid addition to this research. It would also be useful to use an observing system simulation experiment (OSSE) to better constrain the uncertainties of MODIS BT retrievals and therefore MODIS and CALIOP observed BTLR according to Eqn. 1.1. Such a technique will be discussed further in Section 5.2.

4.4 CloudMask Cloud Fractional Agreement Results

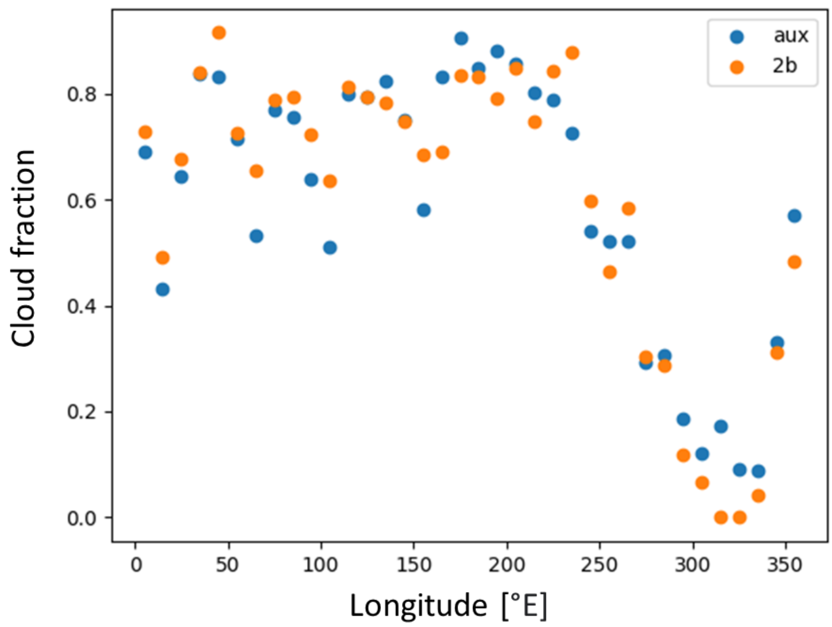

FIGURE 4.18: Monthly average MODIS AUX CF_{AUX} (aux) and CF_{2B} (2b) cloud fraction for 2015 September in each 10 ° longitude bin for a latitude of 85.5 °N. The longitude bins are centred at -175 °E, -165 °E etc.

The results comparing the MODIS AUX CloudMask CF_{AUX} calculation to CF_{2B} can be seen in Fig. 4.18 and Fig. 4.19. Figure 4.18 shows a comparison of the monthly average cloud fraction in 10 ° longitude × 3 ° latitude bins for 2015 September for a

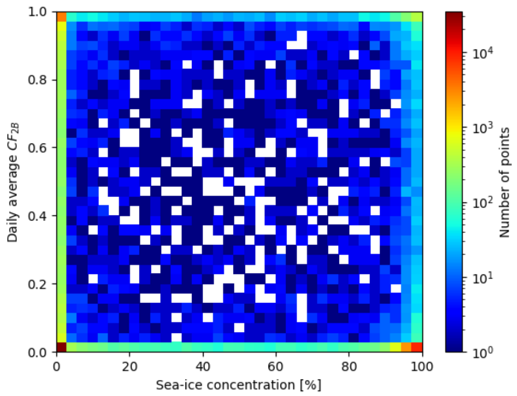

(A) CF_{2B} (cloud fraction) obtained from the 2B CloudFraction product.

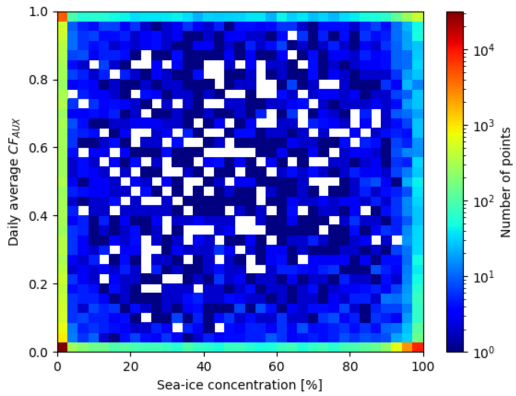

(B) CF (cloud fraction) obtained from the MODIS AUX CloudMask product.

FIGURE 4.19: Daily average CF_{AUX} (A) or CF_{2B} (B) cloud fraction and AMSR-E fractional sea-ice coverage plotted in a 2D density plot for 2015 polar-day. There are 35 CF_{AUX} (A) or 35 CF_{2B} (B) bins (centred on 0.0143, 0.0286 etc. cloud fraction), and 35 sea-ice bins (centred on 1.43 %, 2.86 % etc.sea-ice fractional coverage).

latitude of 85.5 $^\circ N$. While there are some differences between the CF_{2B} and CF_{AUX} values, in general there is good agreement between the two instruments for cloud fraction. This suggests that the technique described in Section 3.5.1 for approximating CloudMask cloud fractional coverage as CF_{AUX} in a coarse resolution latitude and longitude grid generally replicates the average CF_{2B} well.

Moving forward onto a 2015 polar-day and Arctic comparison of the two products, Fig. 4.19 shows 2D density plots of the daily average CF_{AUX} and CF_{2B} values aggregated into collocated AMSR-E fractional sea-ice cover bins. Examining Fig. 4.19, it is clear that there is broad agreement between the two techniques. The concentration of points in the largest sea-ice bin is likely because there is a large amount of full sea-ice coverage in the Arctic. Likewise, the concentration of points in the smallest sea-ice bin is likely because in the polar-day there are many open-ocean points with sea-ice fractional coverage values of 0 %. It is clear from both Fig. 4.19a and Fig. 4.19b that there are more cloudy pixels over open-ocean than over higher sea-ice points. This is likely explained since open-ocean tends to favour low-level cloud formation

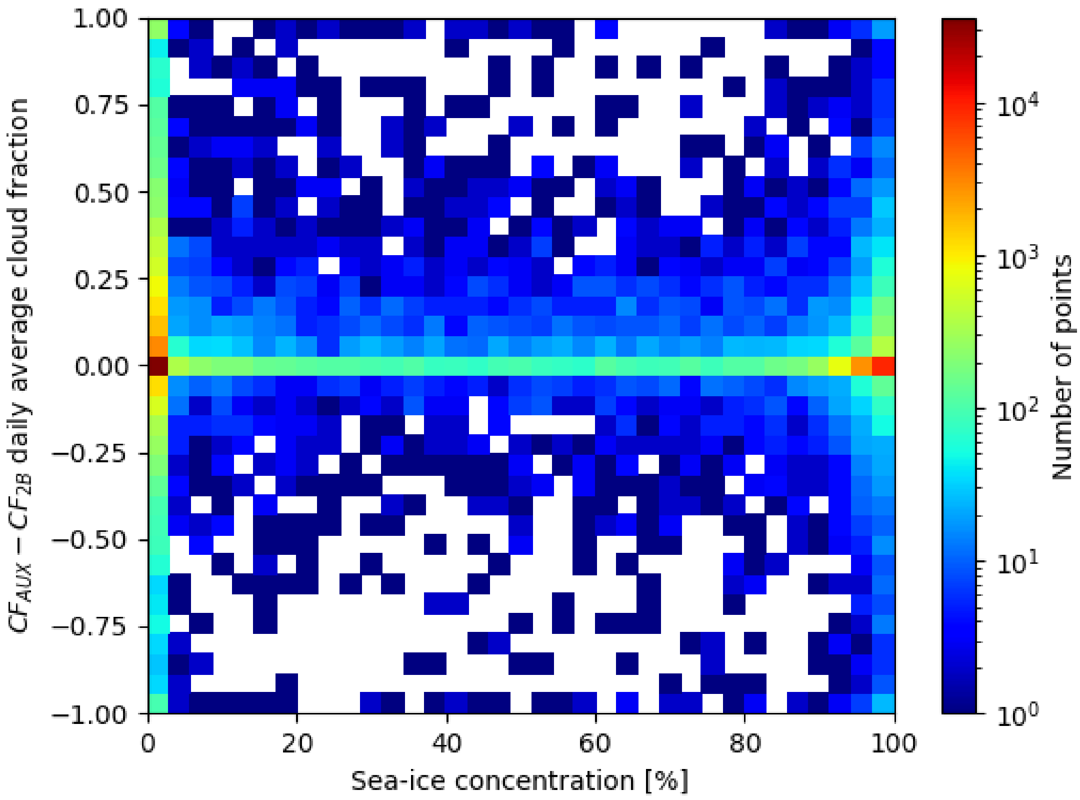

FIGURE 4.20: Daily average CF_{AUX} - CF_{2B} cloud fraction difference and AMSR-E fractional sea-ice coverage plotted in a 2D density plot for 2015 polar-day. There are 35 CF_{AUX} - CF_{2B} bins (centred on −0.0572, −0.0286, 0.0286, 0.0572 etc. cloud fraction), and 35 sea-ice bins (centred on 1.43 %, 2.86 % etc.sea-ice fractional coverage).

(Sato et al., 2012; Yu et al., 2019) in the Arctic. One potential issue is that the latitude and longitude centres of these bins vary, and so factors other than sea-ice could be affecting the cloud fraction retrieval. Keeping the latitude and longitude coordinates constant could therefore be a warranted avenue of future work.

Figure 4.20 shows a density plot of the difference between Fig. 4.19b and Fig. 4.19a. As can be seen, there is a vertical spread in the data points, particularly for low and high sea-ice values. More specifically, it looks like CF_{AUX} overestimates CF_{2B} more frequently than underestimates. This could be explained by a combination of two reasons. First, the CloudMask product is known to be clear-sky conservative

(Platnick et al., 2018). Therefore, it is possible that many clear-sky pixels are being classified as cloudy in the AUX product, shifting the CF_{AUX} grid box daily average higher. It is important to highlight that Holz et al. (2008) found in the Arctic winter period that the CloudMask is clear-sky biased in regions of high sea-ice for C5. This is reflected in Fig. 4.20 where there is a small spread below the 0.00 $CF_{AUX} - CF_{2B}$ line in the 90–100 % sea-ice concentration bins. However, even at these higher sea-ice concentration bins more points are overestimated by CF_{AUX}.

The second explanation is tied to the technique used to approximate the grid level cloud fraction cover (as described in Section 3.5.1). The CF_{AUX} calculation utilises a binary Boolean approach for the N values: cloudy pixels are given a weight of 1.0 and all others are given a weight of 0.0. In contrast, the cloudy pixels used in CF_{2B} can take a value in the range 0.0–1.0, since the 2B-GEOPROF-LIDAR product gives cloud fraction values of less than 1.0 when a pixel is only partly covered by clouds. Therefore, pixels which are partly cloudy will contribute to the daily average CF_{2B} with a value of less than 1.0 but to the daily average CF_{AUX} with a value equal to 1.0. This would lead to an overestimate of CF_{AUX} compared to CF_{2B} in the case of high fractional coverage grid bins.

While the overestimation is seen for all sea-ice concentration bins, there is specifically a large CF_{AUX} overestimation compared to CF_{2B} for the lowest sea-ice concentration bin. The increase in points seen in the lowest sea-ice bin might be partially explained since there are simply more retrievals over open-ocean than high sea-ice concentration points. However, low sea-ice cover also generally favours more low-level cloud cover as previously discussed. This could lead to more CF_{AUX} and CF_{2B} values greater than 0.0 which might explain why more points are seen further away from the 0.00 $CF_{AUX} - CF_{2B}$ line than for higher sea-ice cover values. In particular, there are many points in this bin where $CF_{AUX} - CF_{2B}$ is near to 1.00, suggesting that there are points where MODIS detects a cloud that the 2B-GEOPROF-LIDAR product fails to detect. I know the CloudMask is clear-sky conservative as discussed in Section 1.2.2, which may explain this disagreement.

Overall the CF_{AUX} calculation seems to replicate CF_{2B} well at the 10 $^{\circ}$ longitude $\times$ 3 $^{\circ}$ latitude resolution since most points sit near the 0.00 $CF_{AUX} - CF_{2B}$ line. However, Fig. 4.20 seems to show a surface dependence for the CloudMask cloud-detection success rate compared to 2B-GEOPROF-LIDAR. Given the lack of thermal contrast between sea-ice and clouds as discussed by Liu et al. (2010), this dependence on sea-ice concentration could be explained (note that Liu et al. (2010) investigated C5 not C6), however it could also be partially explained by the difference in the number of retrievals in each bin. Therefore, further investigation is warranted. I suggest reducing the coarseness of the grid resolution as there could be large sea-ice concentration variability within a 10 $^{\circ}$ longitude $\times$ 3 $^{\circ}$ latitude bin, and evaluating how changes to sea-ice concentration impact low-level cloud cover detection at a constant latitude and longitude coordinate.

4.5 Phase Hitrate Results

4.5.1 Low-Level, Single-Layer Cloud Phase Distribution

The statistics for the pixels where MODIS and CALIOP agree that a low-level (CTH $\leq$ 2 km) single-layer cloud is detected can be broken up into thin ($\tau_{CALIOP} < 2$) and thick clouds ($\tau_{CALIOP} \geq 2$) respectively, with τ_{CALIOP} being determined by the CALIOP 532 nm 5 km τ product. The CALIOP 532 nm 5 km product was used since I did not have access to the 1 km product, and since CALIOP is known to be accurate for low τ retrievals (Young et al., 2018). The results are listed in Table 4.3. The small percentage of ice-phase clouds is likely explained since I am analysing low-level clouds in the Arctic polar-day period, during which temperatures are warmer than in the polar-night and for higher altitudes.

TABLE 4.3: Statistics of agreement between MODIS TIR/OP 1 *km* and CALIOP phase retrieval techniques, broken up into thin ($\tau < 2$) and thick ($\tau \geq 2$) clouds, where 275,956 thin single-layer low-lying clouds were detected by the CALIOP 532 *nm* 5 *km* τ retrieval mechanism and 989,483 thick single-layer low-lying clouds were detected. The table does not include data where the CALIOP phase retrieval mechanism failed, which makes up 0.23 % and 0.5 % of the data for thick and thin clouds, respectively. The percentages are in terms of the number of total single-layer low-lying clouds as agreed upon by MODIS and CALIOP (1,265,439 retrievals).

	CALIOP liquid [%] thin	**CALIOP liquid [%] thick**	**CALIOP ice [%] thin**	**CALIOP ice [%] thick**
TIR liquid	14.39	56.76	0.30	0.40
TIR ice	1.41	1.06	0.20	0.06
TIR uncertain	4.58	19.45	0.43	0.23
OP liquid	19.18	76.56	0.56	0.58
OP ice	0.86	0.33	0.32	0.09
OP uncertain	0.34	0.39	0.05	0.01

Three key features stand out in Table 4.3. First, there are a large number of points classified as ice by the TIR method that CALIOP classifies as liquid (a total of 2.47 % of all pixels). It is known from the literature (Platnick et al., 2018) that MODIS C6 still struggles with mis-classifying low-lying liquid clouds as ice-phase (though this is expected to have improved since C5); however, I hypothesize this number to be larger for optically thin clouds or broken cloud scenes due to the increased influence of surface radiance at the TOA. This is reflected in Table 4.3, which lists that the share of mis-classified liquid-phase clouds decreases for thicker clouds. However, as expected from the literature (Platnick et al., 2018) the use of emissivity ratios in the TIR method do not seem to lead to a consistent liquid-phase classification when compared to the CALIOP instrument or even the OP method. Instead, as expected many of the liquid-phase pixels (according to CALIOP) are now classified as uncertain according to the TIR method (Platnick et al., 2018).

This leads us to the second observation, that the TIR method classifies a large proportion of pixels where a cloud is detected as uncertain, with a total of 24.69 % across all single-layer low-level clouds. In C6, it is known that many of the pixels previously classified as liquid are now classified as uncertain in C6 by the TIR method (Platnick et al., 2018). This is reflected in Table 4.3 where 24.03 % of the pixels were classified as uncertain according to the TIR method but liquid by the CALIOP method. In contrast, the percentage of points classified as uncertain by the OP retrieval mechanism is much smaller, a total 0.79 % of the total cloudy points. This could be explained by the additional more stringent tests included in the OP test on top of the TIR test itself.

Third, the retrievals are dominated by thick clouds (78.2 % of retrievals), and the agreement for thicker clouds is generally better. For example, for both the TIR and OP methods the agreement with CALIOP that a liquid cloud is detected is higher for thicker clouds, making up 72.59 % and 97.91 % of the 989, 483 thick clouds detected (for TIR and OP respectively). For thin clouds, out of a total of 275, 956 retrievals these percentages drop to 66.00 % and 87.95 % for the TIR and OP methods, respectively. This suggests two interpretations. First, MODIS phase classification performs better for liquid-phase clouds when the clouds are optically thicker. Second, since the majority of points are liquid according to CALIOP (97.66 % of the total thin and thick clouds) and most are thick liquid clouds (77.27 % of the total thin and thick clouds), the phase hitrate analysis outlined in Section 4.5.2 and 4.5.3 will be dominated by the success of liquid, thick cloud retrievals.

4.5.2 Influence of Sea-Ice Fractional Cover on Phase Hitrate

Liquid Clouds

Fig. 4.21 shows the phase hitrate for the TIR and OP retrieval methods averaged into 10 sea-ice bins from collocated AMSR-E data for 2015 polar-day. First, the OP method has a higher average hitrate than the TIR method for liquid clouds, likely

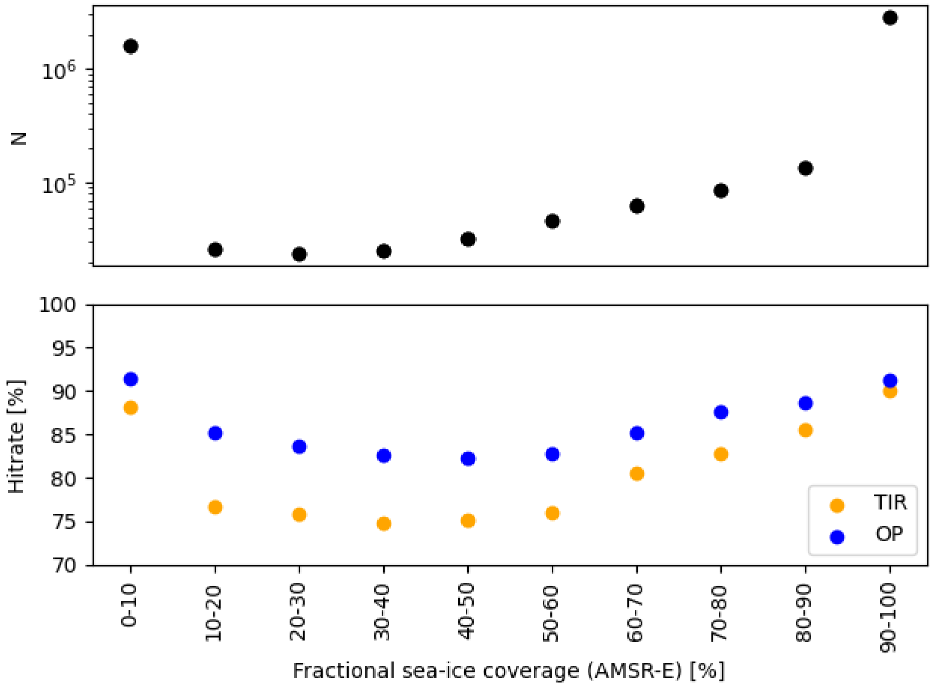

FIGURE 4.21: MODIS (TIR and OP retrieval methods) and CALIOP hitrate agreement for Arctic polar-day in 2015 broken into 10 collocated AMSR-E sea-ice bins for liquid-phase clouds. N is the total number of retrievals in each sea-ice bin.

due to the inclusion of the additional more stringent tests in OP. More specifically, the hitrate drops largely after the first sea-ice bin for both methods, but the drop is larger for the TIR method. The TIR and OP hitrates show an initial decrease between sea-ice fractional coverage bins 0–10 % to 10–20 % of 11.45 % and 6.31 % for TIR and OP respectively. This suggests that the TIR method is more affected by surface fractional ice-coverage than the OP method. Given that the OP retrieval method relies on additional phase votes by three additional tests which might provide greater adaptability to difference surface types, this smaller drop when sea-ice fractional cover increases above 0 % might be expected. For example, the 1.38 μm test is known to be useful over snow and ice covered surfaces in the Arctic (Gao et al., 1993), so may be reducing the impact of the sea-ice on phase retrievals.

Interestingly, it appears that as sea-ice coverage increases further the hitrate rises again. Figure 4.22a shows the percentage of points that are classified as not cloudy and cloudy by both CALIOP and MODIS for each retrieval technique respectively. As can be seen, for higher sea-ice fractional cover bins the percentage of points classified as not-cloudy by both instruments increases, and the percentage of cloudy points is generally consistent, though has a slight dip at the end. This correlates with the increase in hitrate for both instruments as sea-ice cover increases. Given the literature suggests that many of the issues for the TIR technique lie with broken or optically thin clouds (see Section 1.2.3), a higher percentage of cloud-free pixels in the analysed datset could explain the increase in hitrate since MODIS would not have to extract phase from optically thin clouds. However an investigation into the distribution of cloud τ against sea-ice fractional coverage would be necessary to confirm this hypothesis.

To analyse the hitrates further, I broke up the hitrates into fractional disagreement that a cloud was detected and that no cloud was detected, and the results can be seen in Fig. 4.22b. These percentages show the percentage of points where MODIS and CALIOP disagreed that a liquid cloud was detected, where D1 indicates that CALIOP detects clear-sky and D2 indicates that MODIS detects clear-sky. It is clear that as fractional sea-ice cover increases past the 40–50 % bin the amount of D1 disagreement decreases, and D2 increases slightly. The D1 decrease is further corroborated by looking back at Fig. 4.22a, as there is a corresponding increase in the agreement that a clear-sky pixel is detected. This suggests that as sea-ice fractional cover increases towards 100 % MODIS performs better in terms of classifying clear-sky pixels correctly, but slightly worse in terms of mis-classifying liquid cloud pixels as clear-sky. This could suggest that a partly sea-ice covered surface has more similar thermal properties in the 8.5 μm, 11 μm, and 12 μm channels to a liquid cloud than a fully covered sea-ice surface. Importantly, the former improvement seems to dominate and make up a larger fraction of the pixels, and hence seems to explain the corresponding increase in hitrate at higher sea-ice fractional cover bins.

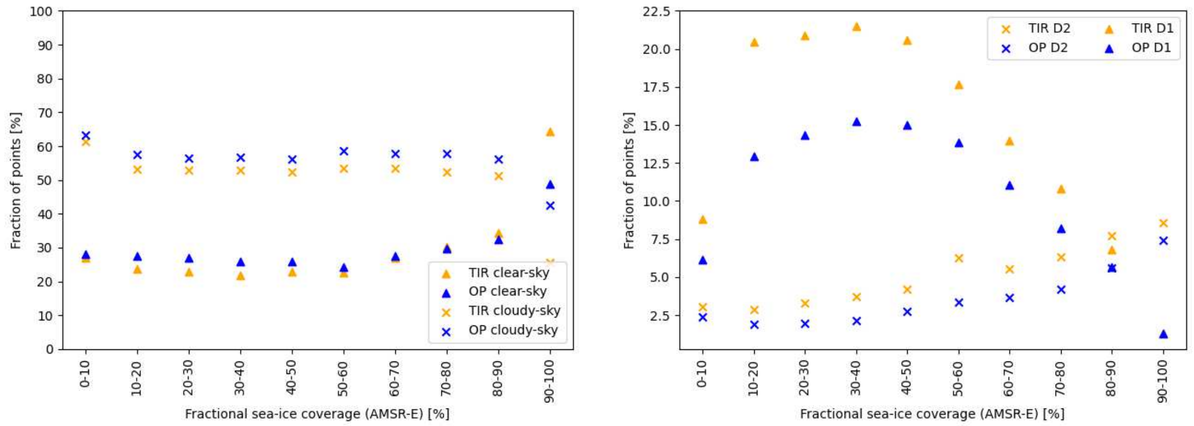

(A) MODIS TIR/OP phase retrieval method and CALIOP hitrate agreement that a clear-sky or cloudy pixel (where the phase of the cloud is liquid) is detected as a fraction of the total points used in Fig. 4.21 for Arctic polar-day in 2015 broken into 10 collocated AMSR-E sea-ice bins for liquid-phase clouds.

(B) MODIS and CALIOP hitrate disagreement for Arctic polar-day in 2015 broken into 10 collocated AMSR-E sea-ice bins for liquid-phase clouds. D1 denotes all points where CALIOP detects a clear-sky pixel and MODIS detects a liquid-phase pixel, and D2 indicates all points where CALIOP detects a liquid-phase pixel and MODIS detects a clear-sky pixel.

FIGURE 4.22

Interestingly, the increase in D1 between the first two sea-ice fractional coverage bins also correlates to the decrease in hitrate discussed earlier. This, in conjunction with the correlation between D1 and hitrate in higher sea-ice bins, suggests that the liquid-phase hitrate is driven primarily by the success of MODIS in detecting clear-sky pixels correctly. Once again, OP seems to perform better at this than the TIR method.

Ice Clouds

Figure 4.23 shows the hitrate agreement for ice-phase clouds. The first thing to notice is that the hitrate percentages are higher than the liquid counterparts. This is likely due to the fact that there are very few ice-phase pixels in the Arctic in polar-day for low-lying, single-layer clouds, as can also be seen in Table 4.3. As can be seen in Fig. 4.24a, for both retrieval techniques clear-sky pixels dominate the hitrate. The percentage of ice-phase pixels increases in the largest sea-ice bin, which makes sense given the likely corresponding temperature drop over cooler sea-ice surfaces, however, even then non-cloudy pixels make up around 95 % of the pixels.

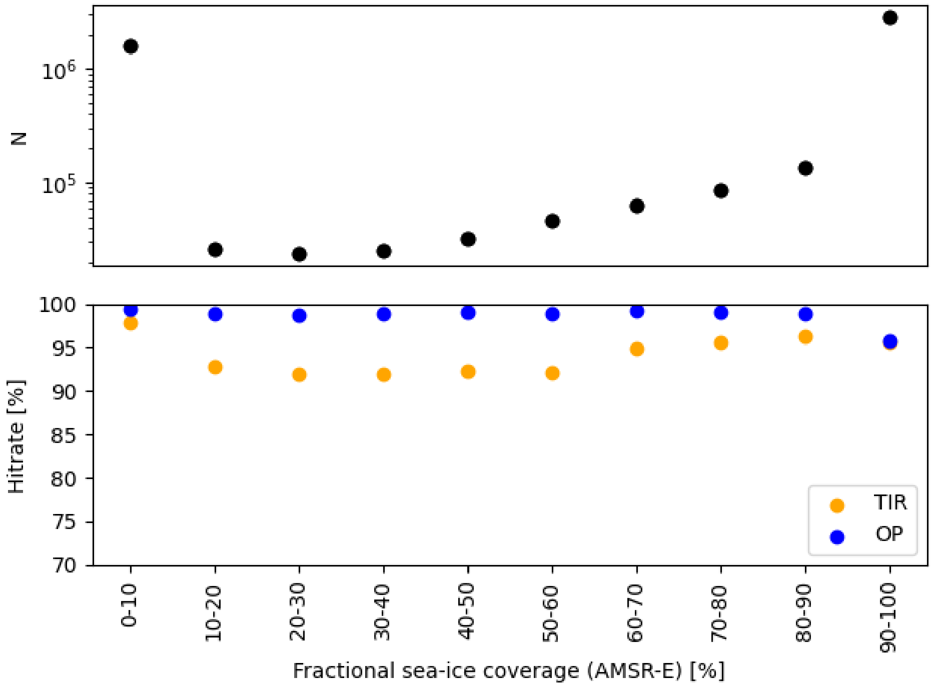

FIGURE 4.23: MODIS TIR/OP phase retrieval method and CALIOP hitrate agreement for Arctic polar-day in 2015 broken into 10 collocated AMSR-E sea-ice bins for ice-phase clouds. N is the total number of retrievals in each sea-ice bin.

The next striking observation is that there is more variability in the TIR hitrate compared to the OP method, with standard deviations of 2.05 % and 1.00 % respectively. This is likely due to the fact that the TIR method classifies more pixels as ice compared to OP, as is reflected in the lower fractional amount of clear-sky pixels classified by the TIR method compared to the OP method (Fig. 4.24a). Moreover, Fig. 4.24b shows that the TIR method struggles much more with D1 disagreement where CALIOP detects a clear-sky pixel and MODIS detects a cloudy (in this case ice-phase) pixel. This suggests that the decrease in agreement of clear-sky pixels is explained by the TIR method mis-classifying clear-sky as ice-phase. In contrast, this occurs for much fewer pixels for the OP method, suggesting that the additional stringent tests go some way to improving clear-sky classification. Once again, mis-classifying clear-sky pixels as cloudy seems to drive the disagreement with the CALIOP phase retrievals.

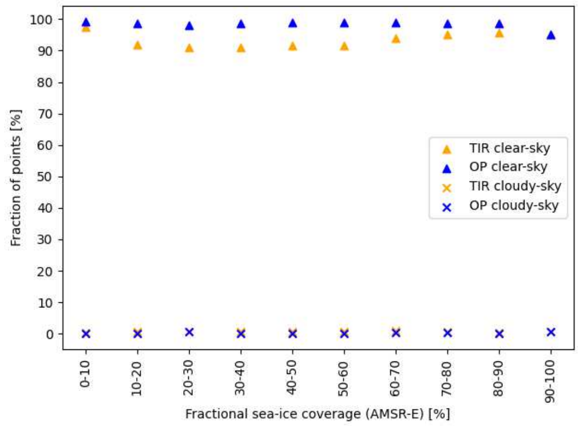

(A) MODIS TIR/OP phase retrieval method and CALIOP hitrate agreement that a clear-sky or cloudy pixel (where the phase must be ice) is detected as a fraction of the total points used in Fig. 4.23 for Arctic polar-day in 2015 broken into 10 collocated AMSR-E sea-ice bins for ice-phase clouds.

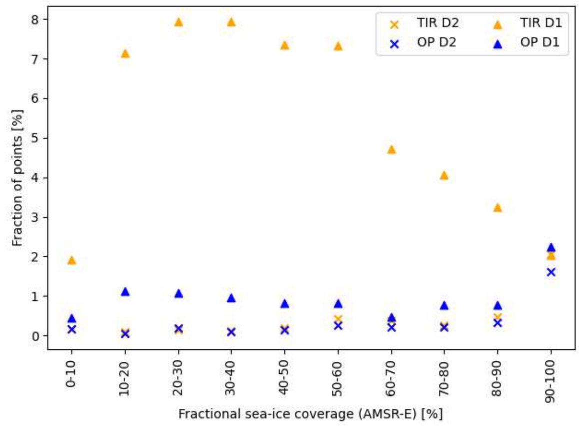

(B) MODIS and CALIOP hitrate disagreement for Arctic polar-day in 2015 broken into 10 collocated AMSR-E sea-ice bins for ice-phase clouds. D1 included all points where CALIOP detects a clear-sky pixel and MODIS detects an ice-phase pixel, and D2 included all points where CALIOP detects an ice-phase pixel and MODIS detects a clear-sky pixel.

FIGURE 4.24

4.5.3 Seasonal variability of phase hitrate

Fig. 4.25b shows hitrate plots partitioned into monthly averages for all 2015 polar-day pixels not over land, where the phase of the agreement (or disagreement) in Eqn. 3.9 can be either liquid or ice. Fig. 4.25a shows the same plot, except this time with pixels where MODIS and CALIOP agree that no-cloud is detected not included in the calculation so that those pixels do not dominate the hitrate values. Two observations are clear. First, the OP method performs better on average in comparison to CALIOP than the TIR method. Second, the seasonal variability in hitrate is larger for TIR than for OP. The standard deviation of the monthly hitrate values in Fig. 4.25b for each method are 2.83 % and 0.81 % for TIR and OP phase retrieval methods respectively.

Interestingly, Fig. 4.25a shows a much decreased overall hitrate in the winter months, a decrease that is much smaller in Fig. 4.25b. To analyse this hitrate further, I repeated the diagnostic breakdown in Section 4.5.2 on Fig. 4.25b. Figure 4.26a shows that in those winter months the agreement that a cloud is detected drops but that there

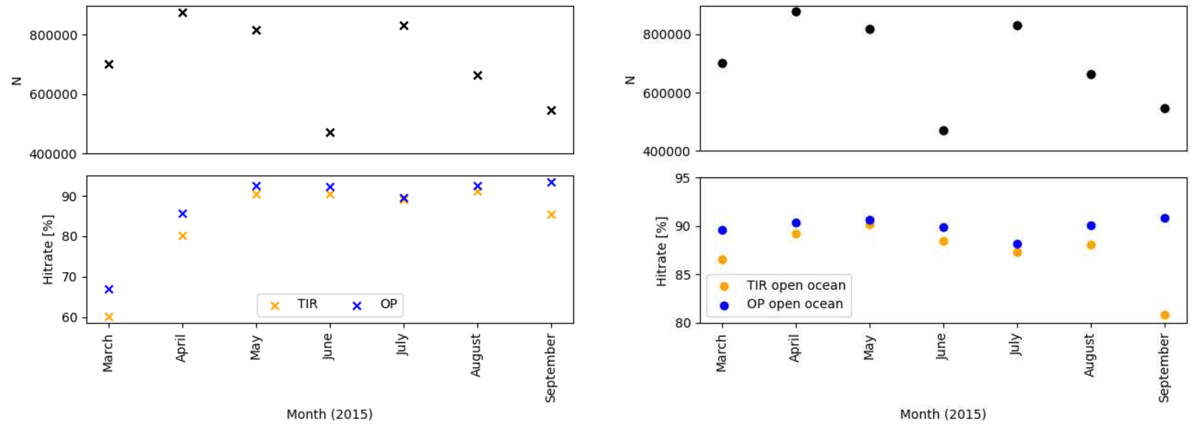

(A) MODIS TIR/OP phase retrieval method and CALIOP hitrate agreement for all single-layer low-level pixels not over land in the Arctic for polar-day in 2015. Dataset broken into monthly aggregated hitrate averages. Pixels where the two instruments agree that no cloud is detected have been removed fron Eqn. 3.9. N is the total number of retrievals in each month.

(B) MODIS TIR/OP phase retrieval method and CALIOP hitrate agreement for all single-layer low-level pixels in Arctic polar-day in 2015 not over land surfaces, broken into monthly aggregated hitrate averages. Unlike (A), no-cloud pixels were counted in the hitrate here. N is the total number of retrievals in each month.

FIGURE 4.25

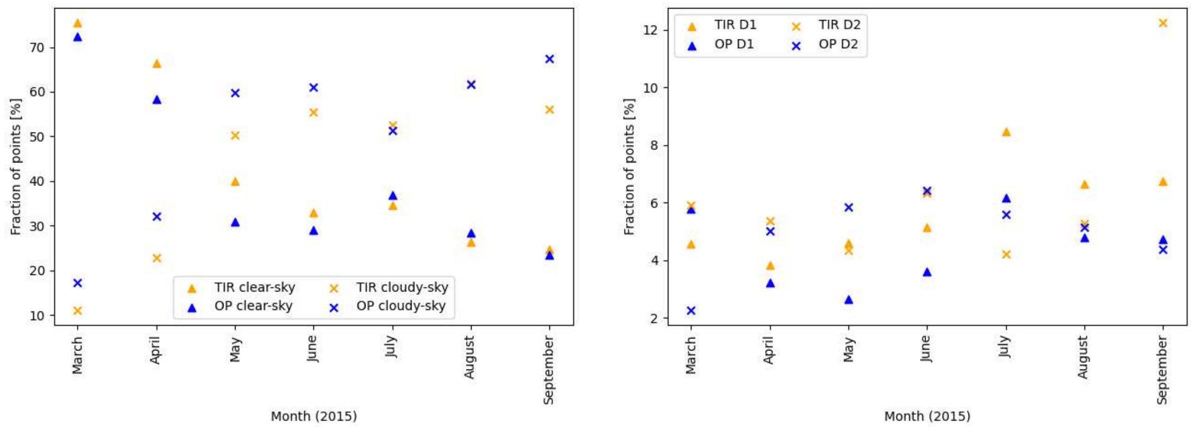

(A) MODIS TIR/OP phase retrieval method and CALIOP hitrate agreement that a clear-sky or cloudy pixel (where the phase of the cloud can be anything) is detected as a fraction of the total points used in Fig. 4.25b for all single-layer low-level pixels in the Arctic polar-day in 2015 not over land surfaces, broken into monthly averages.

(B) MODIS and CALIOP hitrate disagreement (as a fraction of the total points used in Fig. 4.25b) for all single-layer low-level pixels in the Arctic polar-day in 2015 not over land surfaces. The disagreement is broken into monthly aggregated hitrate averages, where D1 denotes all points where CALIOP detects a clear-sky pixel and MODIS detects a cloudy pixel. Whereas, D2 labels all points where CALIOP detects a liquid cloud and MODIS detects a clear-sky pixel.

FIGURE 4.26

is a corresponding increase in the agreement that a clear-sky is detected. The impact of the drop in Fig. 4.26a on Fig. 4.25b therefore might be lessened due to the domination of pixels where the two instruments agree that a clear-sky is detected. It is therefore likely that this drop in cloudy pixels being detected explains the corresponding drop in hitrate in the first three months of Fig. 4.25a and the much smaller drop in Fig. 4.25b.

Figure 4.26b shows the seasonal percentage disagreement between the two instruments for two different scenarios for the TIR and OP method respectively: first (D1) where CALIOP detects a clear-sky pixel and MODIS detects a cloudy pixel, second (D2) where CALIOP detects a liquid cloud and MODIS detects a clear-sky pixel. Generally, these values are consistent for all four options. However, D2 increases in September for the TIR method, where it is also the case that cloudy pixels (as agreed by each instrument) make up approximately 60–70 % of pixels, a percentage which increases into the summer months (see Fig. 4.26a). The increase in low-level cloud amount is also verified in the literature where past studies have seen large amounts of low-level clouds in the summer (Curry & Ebert, 1992). Both the increase in D2 disagreement and low-level cloud amount in September also correspond with a drop in hitrate to about 80 % in September for the TIR method.

This sudden increase in the mis-classification of liquid clouds as clear-sky by the TIR method could be due to a variety of reasons, however it does not seem to be replicated by the OP method. The increase in the fraction of pixels that are cloudy could play a large role, particularly if this lead to a corresponding increase in the number of pixels observing thin low-lying liquid clouds over open-ocean. I know from Table 4.3 that TIR struggles with liquid pixels, which is also seen in the literature which specifies that this is a particular problem over open-ocean (Platnick et al., 2018). The impact of surface type could be particularly relevant if there was an increase in the number of thin low-lying liquid clouds over open-ocean so that the radiative influence from the surface is higher at the TOA. In September, sea-ice extent is generally at a minimum, so the number of thin low-lying liquid clouds over open-ocean could reasonably be hypothesised to be higher, perhaps explaining the general tend in Fig. 4.26b that TIR D2 increases into the summer months.

Moreover, the strong seasonal variability in cloud type could have an impact on the hitrate values. This variability could be due to a variety of factors, for example variations in sea-ice coverage can impact cloud type (see Tan et al. (2021) for more discussion on factors influencing Arctic mixed-phase cloud type, or Scott et al. (2020) for a discussion on how cloud-type is linked to LTS and surface type). It is therefore likely that factors controlling cloud-type are also indirectly affecting the monthly average hitrate. This may effect the TIR method more since the additional tests used by OP in its voting method could provide better adaptability to different cloud scenes.

Chapter 5

Conclusions and Future Work

5.1 Conclusions

Focusing on single-layer, low-level clouds north of 60 $^{\circ}N$ in polar-day 2015, this study has quantified the effects of local variations in τ and LTS on MODIS's CTH bias relative to the CALIOP instrument. Reanalysis data was utilised to construct local LTS variations, in particular the results were replicated using the ERA5 and MERRA2 datasets for the vertical temperature structure in the Arctic. It was found that consistent underestimation values occur for the parameter space characterized by low LTS and low τ values, whereas CTH overestimates occurred for low LTS and high τ values. Using LTS as an indicator of the temperature structure and static stability of the lower atmosphere, we propose that the influence of the surface radiance at the TOA would increase with an increase in surface temperature relative to the CTT. This increase in surface temperature would lead to a corresponding increase in the strength of radiation emitted by the surface according to Plank's law, and therefore the surface radiance would have a stronger impact at the TOA. Since the TOA radiance detected by the passive MODIS sensor is a superposition of radiance from all atmospheric levels and the surface, this leads to a surface-bias in the measured cloud-top BT and an underestimate in the CTH retrieval. Moreover, we also propose that the scale of the CTH bias increases as τ decreases since the surface radiance would be attenuated less as it passes through cloud layers.

However, the large standard deviation values shown in Fig. 4.6a suggest that the CTH biases demonstrated by Fig. 4.4 and Fig. 4.5 come from the averaging of typically much larger individual errors. It is suggested that non-linear potential temperature changes could reduce the coupling between LTS and CTH biases since clouds may sit lower or even higher than the 800 hPa pressure-level. However, Fig. 4.9 suggests that CTH bias might also vary with sea-ice concentration, which we speculate might be due to the increased reflectance of downwelling longwave radiation. While the geographic variance of the CTH biases (Fig. 4.8) showed that the spatial pattern was similar to the spatial pattern of the annual LTS projection with negative biases arising in areas of higher LTS over open-ocean, the two plots showed differences in some key regions as well. More generally, while our results suggest that LTS and τ are important to the magnitude and sign of the CTH bias, other reasons, such as surface type and geographic location, also seem to be important, but no single dominant reason is easily identified. This suggests that further work is needed to more closely tie the CTH biases in the Arctic to other geographically and seasonally varying properties such as sea-ice cover.

Three conclusions may be drawn from our analysis of Hypothesis 2. First, the zonal averaging of BTLR values applied in Eqn. 2.1 and used by MODIS's CTH product is inconsistent with CRTM calculated BTLR values. Second, the use of AMSR-E sea-ice concentration in the computation of clear-sky BT lowers the calculated CTH and BTLR values in polar-day conditions in 2015 due to emissivity differences between open-ocean and fractional sea-ice cover. However, the impact of correctly assigning surface type is small due to similar emissivities between sea-ice and open-ocean at wavelengths around 11 μm. Third, it is clear that there is a discrepancy between the apparent BTLR calculated using Eqn. 1.1 and the temperature lapse rate according to MERRA2 data. The apparent BTLR calculation seems to be overestimating the temperature lapse rate, an issue that also seems to occur for values obtained from the literature (Baum et al., 2012). Upon further investigation, it appears likely that most of the difference is arising due to discrepancies between the MODIS retrieved BT in the 11 μm channel compared to those simulated by the CRTM model in clear-sky conditions. More specifically, MODIS measured BT values seem to be overestimated by the CRTM modelled BT calculated using MERRA2 reanalysis surface temperature data. This hints at the potential for similar discrepancies existing for MODIS measured cloud-top BT relative to "true" cloud-top temperatures and cloud-top BT as simulated by CRTM (although such simulations were not carried out in this work).

Overall, while Hypothesis 2 is qualitatively correct, the magnitude of the impact on CTH calculations was found to be small due to small emissivity differences between water and sea-ice. In contrast, our investigation of BTLR suggests that the methodology described by Eqn. 1.1 overestimates at higher latitudes, particularly in winter months. Therefore, it is likely that BTLR biases, and therefore MODIS CTH biases, are being influenced by factors outside of those outlined by Hypothesis 2.

Our analysis of the MODIS CloudMask showed that the approximation for cloud fraction represented by the variable CF_{AUX} was comparable to the average CF_{2B} cloud fraction for a coarse bin resolution of 10 ° longitude × 3 ° latitude . The difference between the two variables showed a sea-ice concentration dependence and that CF_{AUX} overestimated CF_{2B} more than it underestimated. We suggest this can be explained by the clear-sky conservative nature of the MODIS CloudMask product and the weighting of cloudy pixels used in calculating CF_{AUX} which used a binary pixel classification logic.

Finally, by analysing phase hitrate compared to CALIOP, it was found that the TIR hitrate consistently performs worse than the OP method. It was found that the hitrates are strongly affected by surface type through the use of collocated AMSR-E sea-ice fractional coverage readings. More generally, a key conclusion from this section is that in the case of both liquid and ice-phase hitrates, clear-sky pixels (according to

CALIOP) cause the largest disagreement. In other words, MODIS struggles with misclassifying non-cloudy pixels as either liquid or ice-phase, with peak disagreements occurring for sea-ice bins in the 20–50 % sea-ice fractional coverage range. This is a particular problem for the TIR method, but also a problem for the OP method for liquid-phase clouds. Moreover, it was found that there is a strong seasonal dependence for phase hitrate. We suggest that this is due to a combination of surface type changes, which affects hitrate as verified in Section 4.5.2, but also seasonal cloud type variability.

5.2 Future Work

To further analyse Hypothesis 1, one could use AMSR-E data collocated with MODIS and CALIOP CTH readings to analyse the dependence of CTH bias on sea-ice fractional coverage. Since Fig. 4.9 seems to suggest a seasonal variation in CTH bias, this is a viable avenue for future work that could reveal a clear surface dependence of low-level CTH biases in the Arctic. Additionally, one could use an alternative measure of the vertical potential temperature gradient, such as estimated inversion strength (Wood & Bretherton, 2006), to analyse whether the spread in individual errors shown in Fig. 4.6 is due to a decoupling between LTS and CTH biases. This could be due to non-linear potential temperature changes, as discussed in Section. 4.2.

Narrowing down why the overestimate values of clear-sky CRTM simulated BT occur would be a warranted avenue of future research. First, it could be that these overestimates are occurring over regions of high sea-ice at higher latitudes, or that the MERRA2 reanalysis dataset is inaccurately representing the actual surface temperature influencing MODIS retrievals of BT. To investigate this further, a radiative-transfer-model-based OSSE (Zeng et al., 2020) could be used to simulate the BT that MODIS could detect under different circumstances and the level of precision that could be expected from the instrument. An OSSE usually includes a nature run to simulate the so-called "truth" state of the atmosphere without making use of data assimilation techniques that account for actual observations (e.g., Masutani et al., 2013). This nature state is then used in a simulation of possible observations of a given variable as it would be detected by an instrument (Ye et al., 2022), such as MODIS radiance measurements. In our case, we would want to estimate the true state of the apparent BTLR. This "truth" BTLR could be obtained from reanalysis datasets containing BT values (or temperature and known emissivities at 11 μm), and these simulations should generally also produce realistic errors (Masutani et al., 2013). One could use CALIOP cloud data (such as cloud-top and cloud-base height), to generate optically realistic cloud layers in a CRTM simulation. Then, this simulation could be run to simulate BTs for cloudy-sky and clear-sky conditions while keeping the temperature profile constant to obtain a simulated BTLR related to CALIOP CTH. Then, one could vary various atmospheric and surface properties, such as the temperature profile, surface type, or CTH in this simulation to quantify the impact these variations would have on the simulated BTLR. Since this simulated BTLR would be calculated using the same methodology (described by Eqn. 1.1) as when using actual MODIS retrieved BTs, the uncertainties for the actual MODIS BTLR and CTH estimations would be bounded, assuming MODIS runs perfectly, or with added uncertainties included when there is additional calibration error in the MODIS instruments. This would be a sensible approach to determine how realistic variability in properties such as surface emissivity or surface temperature would impact MODIS retrieved radiances and how this could affect the precision of BTLR, or even CTH. It would also help to better bound the MODIS BTLR calculations and therefore allow for an assessment of the possible reasons for the large variation found in this work for individual data within a latitude and longitude bin (e.g. Fig. 4.12).

For the analysis of MODIS CloudMask, future experiments could include analysis of finer resolutions to find the scale limit of the CF_{AUX} approximation and to investigate the variability of the $CF_{AUX} - CF_{2B}$ distribution for low sea-ice concentration values. Alternatively, we suggest looking at how cloud fractional coverage varies with surface sea-ice cover for points at a constant latitude and longitude to more directly analyse the impact of sea-ice fractional coverage. Moreover, for the analysis of hitrate, we speculate that the misclassification of clear-sky pixels is likely driven by similar thermal properties between partly sea-ice covered surfaces and low-level clouds, but further investigation is warranted. In particular, we suggest investigating how hitrate varies with the underlying surface classification by MODIS since the specific application of the new C6 β parameter depends on surface type (Platnick et al., 2018). Given the known issues with broken cloudy scenes (Platnick et al., 2018), future work may include the analysis of MODIS phase hitrate for pixels classified as partly-cloudy by the CSR mask to analyse the impact of cloud type on phase detection.

Bibliography

Ackerman, S., Holz, R., Frey, R., Eloranta, E., Maddux, B., & McGill, M. (2008). Cloud detection with modis. part ii: Validation. *Journal of Atmospheric and Oceanic Technology*, *25*, 1073–1086. https://doi.org/10.1175/2007JTECHA1053.1

Barnes, B., Cannizzaro, J., English, D., & Hu, C. (2019). Validation of viirs and MODIS reflectance data in coastal and oceanic waters: An assessment of 2 methods. *Remote Sensing of Environment*, *220*, 110–123. https://doi.org/10.1016/j.rse.2018.10.034

Baum, B., Menzel, P., Frey, R., Tobin, D., Holz, R., Ackerman, S., Heidinger, A., & Yang, P. (2012). MODIS cloud-top property refinements for collection 6. *Journal of Applied Meteorology and Climatology*, *51*, 1145–1163. https://doi.org/10.1175/JAMC-D-11-0203.1

Bodhaine, B., Wood, N., Ellsworth, D., & Slusser, J. (1999). On rayleigh optical depth calculations. *Journal of Atmospheric and Oceanic Technology*, *16*, 1854–1861. https://doi.org/10.1175/1520-0426(1999)016<1854:ORODC>2.0.CO;2

Brenguier, J., Burnet, F., & Geoffroy, O. (2011). Cloud optical thickness and liquid water path – does the k coefficient vary with droplet concentration? *Atmospheric Chemistry and Physics*, *11*, 9771–9786. https://doi.org/10.5194/acp-11-9771-2011

Cavalieri, T. M., D. J., & Comiso., J. C. (2014). Amsr-e/aqua daily l3 12.5 km brightness temperature, sea ice concentration, snow depth polar grids, version 3. [Accessed: 2023-08-22]. https://doi.org/10.5067/AMSR-E/AE_SI12.003

Ceppi, P., Brient, F., Zelinka, M., & Hartmann, D. (2017). Cloud feedback mechanisms and their representation in global climate models. *Wiley Interdisciplinary Reviews*, *9*. https://doi.org/10.1002/wcc.465

Chandrasekhar, S. (1960). *Radiative transfer.* Dover Publications. https://store.doverpublications.com/0486605906.html

Cho, H., Yang, P., Kattawar, G., Nasiri, S., Hu, Y., Minnis, P., Trepte, C., & Winker, D. (2008). Depolarization ratio and attenuated backscatter for nine cloud types: Analyses based on collocated CALIPSO lidar and MODIS measurements. *Optics Express*, *16*, 18. https://doi.org/10.1364/OE.16.003931

Cho, H., Zhang, Z., Meyer, K., Lebsock, M., Platnick, S., Ackerman, S., Girolamo, L., Labonnote, L., Cornet, C., Riedi, J., & Holz, R. (2015). Frequency and causes of failed MODIS cloud property retrievals for liquid phase clouds over global oceans. *Journal of Geophysical Research*, *120*, 23. https://doi.org/10.1002/2015JD023161

Curry, J., & Ebert, E. (1992). Annual cycle of radiation fluxes over the arctic ocean: Sensitivity to cloud optical properties. *Journal of Climate*, *5*, 1267–1280. https://doi.org/10.1175/1520-0442(1992)005<1267:ACORFO>2.0.CO;2

Curry, J., Schramm, J., Rossow, W., & Randall, D. (1996). Overview of arctic cloud and radiation characteristics. *Journal of Climate*, *9*, 1731–1764. https://doi.org/10.1175/1520-0442(1996)009<1731:OOACAR>2.0.CO;2

Delst, P., Stegmann, P., & Dang, C. (2020). Crtm: V2.4.0 user guide. *Joint Centre for Satellite Data Assimilation*. https://raw.githubusercontent.com/wiki/JCSDA/crtm/files/CRTM_User_Guide.pdf

Eloranta, E., & Ponsardin, P. (2001). A high spectral resolution lidar designed for long-term arctic cloud and haze observations. *Optical Remote Sensing*, *52*. https://doi.org/10.1364/ORS.2001.OMC4

Froberg, C. (1965). *Introduction to numerical analysis, second edition.* Addison-Wesley. https://sv.20file.org/up1/1382_0.pdf

Gao, G., Goetz, A., & Wiscombe, W. (1993). Cirrus cloud detection from airborne imaging spectrometer data using the 1.38µm water vapor band. *Geophysics Research Letters*, *20*, 301–304. https://doi.org/10.1029/93GL00106

Gelaro, R., McCarty, W., Suárez, M., Todling, R., Molod, A., Takacs, L., Randles, C., Darmenov, A., Bosilovich, M., Reichle, R., Wargan, K., Coy, L., Cullather, R., Draper, C., Akella, S., Buchard, V., Conaty, A., Silva, A., Gu, W., . . . Zhao, B. (2017). The modern-era retrospective analysis for research and applications. *Journal of Climate*, *30*, 5419–5454. https://doi.org/10.1175/JCLI-D-16-0758.1

Global Modeling and Assimilation Office. (2015a). Merra-2 inst3_3d_asm_np: 3d,3-hourly,instantaneous,pressure-level,assimilation,assimilated meteorological fields v5.12.4 [Accessed: 2023-08-22]. https://doi.org/10.5067/QBZ6MG944HW0

Global Modeling and Assimilation Office. (2015b). Merra-2 tavg1_2d_slv_nx: 2d,1-hourly,time-averaged,single-level,assimilation,single-level diagnostics v5.12.4 [Accessed: 2023-08-22]. https://doi.org/10.5067/VJAFPLI1CSIV

Graversen, R., & Wang, M. (2009). Polar amplification in a coupled climate model with locked albedo. *Climate Dynamics*, *33*, 629–643. https://doi.org/10.1007/s00382-009-0535-6

Hahn, L., Armour, K., Zelinka, M., Bitz, C., & Donohoe, A. (2021). Contributions to polar amplification in cmip5 and cmip6 models. *Frontiers in Earth Science*, *9*. https://doi.org/10.3389/feart.2021.710036

Hannon, S., Strow, L., & McMillan, W. (1996). Atmospheric infrared fast transmittance models: A comparison of two approaches. *Proceedings of SPIE*, *2830*, 94–105. https://doi.org/10.1117/12.256106

Heather, C., & Partain, P. (2017). Cloudsat modis-aux auxiliary data process description and interface control document. *CloudSat Project*. https://www.cloudsat.cira.colostate.edu/cloudsat-static/info/dl/modis-aux/MODIS-AUX_PDICD.P_R05.rev1_.pdf

Heidinger, A., O'Dell, C., Bennartz, R., & Greenwald, T. (2006). The successive-order-of-interaction radiative transfer model. part i model development. *Journal of Applied Meteorology and Climate*, *45*, 1388–1402. https://doi.org/10.1175/JAM2387.1

Heidinger, A., & Pavolonis, M. (2009). Gazing at cirrus clouds for 25 years through a split window, part 1: Methodology. *Journal of Applied Meteorology and Climate*, *48*, 1100–1116. https://doi.org/10.1175/2008JAMC1882.1

Hersbach, H., Bell, B., Berrisford, P., Biavati, G., Horányi, A., Sabater, J. M., Nicolas, J., Peubey, C., Radu, R., Rozum, I., Schepers, D., Simmons, A., Soci, C., Dee, D., & Thépaut, J.-N. (2023a). Era5 hourly data on pressure levels from 1940 to present. [Accessed: 2023-08-22]. https://doi.org/10.24381/cds.adbb2d47

Hersbach, H., Bell, B., Berrisford, P., Biavati, G., Horányi, A., Sabater, J. M., Peubey, J. N. C., Radu, R., Rozum, I., Schepers, D., Simmons, A., Soci, C., Dee, D., & Thépaut., J.-N. (2023b). Era5 hourly data on pressure levels from 1940 to present. [Accessed: 2023-08-22]. https://doi.org/10.24381/cds.bd0915c6

Holz, R., Ackerman, S., Nagle, F., Dutcher, S., Kuehn, R., Vaughan, M., & Baum, B. (2008). Global moderate resolution imaging spectroradiometer (modis) cloud detection and height evaluation using caliop. *Journal of Geophysical Research Atmospheres*, *113*, 0–19. https://doi.org/10.1029/2008JD009837

Hu, Y. (2007). Depolarization ratio–effective lidar ratio relation: Theoretical basis for space lidar cloud phase discrimination. *Geophysical Research Letters*, *34*. https://doi.org/10.1029/2007GL029584

Hu, Y., Winker, D., Vaughan, M., Lin, B., Omar, A., Trepte, C., Flittner, D., Yang, P., Nasiri, S., Baum, B., Holz, R., Sun, W., Liu, Z., Wang, Z., Young, S., Stamnes, K., Huang, J., & Kuehn, R. (2009). CALIPSO /CALIOP cloud phase discrimination algorithm. *Journal of Atmospheric and Oceanic Technology*, *26*, 2293–2309. https://doi.org/10.1175/2009JTECHA1280.1

Hu, Y., Winker, D., Yang, P., Baum, B., Poole, L., & Vann, L. (2001). Identification of cloud phase from picasso-cena lidar depolarization: A multiple scattering sensitivity study. *Journal of Quantitative Spectroscopy and Radiative Transfer*, *70*, 569–579. https://doi.org/10.1016/S0022-4073(01)00030-9

Huang, X., Chen, X., Flanner, M., Yang, P., Feldman, D., & Kuo, C. (2018). Improved representation of surface spectral emissivity in a global climate model and its impact on simulated climate. *Journal of Climate*, *31*, 3711–3727. https://doi.org/10.1175/JCLI-D-17-0125.1

Intrieri, J., Fairall, C., Shupe, M., Persson, P., Andreas, E., Guest, P., & Moritz, R. (2002). An annual cycle of arctic surface cloud forcing at sheba. *Journal of Geophysical Research: Oceans*, *107*, SHE 13–1–SHE13–14. https://doi.org/10.1029/2000JC000439

King, M. (1987). Determination of the scaled optical thickness of clouds from reflected solar radiation measurements. *Journal of Atmospheric Sciences*, *44*, 1734–1751. https://doi.org/10.1175/1520-0469(1987)044<1734:DOTSOT>2.0.CO;2

King, M., Platnick, S., Yang, P., Arnold, G., Gray, M., Riedi, J., Ackerman, S., & Liou, K. (2004). Remote sensing of liquid water and ice cloud optical thickness and effective radius in the arctic: Application of airborne multispectral MAS data. *Journal of Atmospheric and Oceanic Technology*, *21*, 857–875. https://doi.org/10.1175/1520-0426(2004)021<0857:RSOLWA>2.0.CO;2

Klein, S., & Hall, A. (2015). Emergent constraints for cloud feedbacks. *Current Climate Change Reports*, *1*, 276–287. https://doi.org/10.1007/s40641-015-0027-1

Lebsock, M., L'Ecuyer, S., & Stephens, G. (2011). Detecting the ratio of rain and cloud water in low-latitude shallow marine clouds. *Journal of Applied Meteorology and Climate.*, *50*, 419–432. https://doi.org/10.1175/2010JAMC2494.1

Liu, Q., & Weng, F. (2006). Advanced doubling–adding method for radiative transfer in planetary atmospheres. *Journal of Atmospheric Sciences*, *63*, 3459–3465. https://doi.org/10.1175/JAS3808.1

Liu, Y., Ackerman, S., Maddux, B., Key, J., & Frey, R. (2010). Errors in cloud detection over the arctic using a satellite imager and implications for observing feedback mechanisms. *Journal of Climate*, *23*, 14. https://doi.org/10.1175/2009JCLI3386.1

Liu, Y., Shupe, M., Wang, Z., & Mace, G. (2017). Cloud vertical distribution from combined surface and space radar–lidar observations at two arctic atmospheric observatories. *Atmospheric Chemistry and Physics*, *17*, 17. https://doi.org/10.5194/acp-17-5973-2017

Liu, Z., Omar, A., Hu, Y., Vaughan, M., & Winker, D. (2005). CALIOP algorithm theoretical basis document—part 3: Scene classification algorithms. *NASA Langley Research Center Doc.*, PC–SCI–202. https://www-\ce{CALIPSO}.larc.nasa.gov/resources/pdfs/PC-SCI-202_Part3_v1.0.pdf

Mace, G., Vane, D., Stephens, G., & Reinke, D. (2007). Level 2 radar-lidar geoprof product version 1.0 process description and interface control document. *CloudSat Project*. https://www.cloudsat.cira.colostate.edu/cloudsat-static/info/dl/2b-geoprof-lidar/2B-GEOPROF-LIDAR_PDICD.P2_R04.20070604.pdf

Marchand, R., Mace, G., Ackerman, T., & Stephens, G. (2008). Hydrometeor detection using cloudsat—an earth-orbiting 94-ghz cloud radar. *Journal of Atmospheric and Oceanic Technology*, *25*, 519–533. https://doi.org/10.1175/2007JTECHA1006.1

Marchant, B., Platnick, S., Meyer, K., Arnold, T., & Riedi, J. (2016). MODIS collection 6 shortwave-derived cloud phase classification algorithm and comparisons with caliop. *Atmospheric Measurement Techniques*, *9*, 1587–1589. https://doi.org/10.5194/amt-9-1587-2016

Markus, T., & Cavaleri, D. (2009). The amsr-e nt2 sea ice concentration algoirthm: Its basis and implementation. *Journal of The Remote Sensing Society of Japan.*, *29*, 216–225. https://doi.org/10.11440/rssj.29.216

Markus, T., Cavaleri, D., & Comiso, J. (2012). *Algorithm theoretical basis document; sea ice products.* NASA Goddard Space Flight Center. https://nsidc.org/sites/default/files/amsr-atbd-supp12-seaice.pdf

Masutani, M., Garand, L., Lahoz, W., Riishøjgaard, L. P., Andersson, E., Rochon, Y., Tsyrulnikov, M., McConnell, J., Cucurull, L., Xie, Y., Ishii, S., Grumbine, R., Brunet, G., Woollen, J. S., & Sato, Y. (2013). Observing system simulation experiments: Justifying new arctic observation capabilities. https://doi.org/10.13140/RG.2.1.4758.4162

Menzel, P., Frey, R., & Baum, B. (2015). *Cloud top properties and cloud phase algorithm theoretical basis document. version 11*. https://www.researchgate.net/publication/242489838_Cloud_top_properties_and_cloud_phase_algorithm_theoretical_basis_document

Menzel, W., Frey, R., Zhang, H., Wylie, D., Moeller, C., Holz, R., Maddux, B., Baum, B., Strabala, K., & Gumley, L. (2008). MODIS global cloud-top pressure and amount estimation: Algorithm description and results. *Journal of Applied Meteorology and Climate*, *47*, 1175–1198. https://doi.org/10.1175/2007JAMC1705.1

Mitchell, J., Senior, C., & Ingram, W. (1989). C02 and climate: A missing feedback? *Nature*, *341*, 132—134. https://doi.org/10.1038/341132a0

MODIS Characterization Support Team. (2017a). Modis 1km calibrated radiances product. nasa modis adaptive processing system. https://doi.org/10.5067/MODIS/MYD021KM.061

MODIS Characterization Support Team. (2017b). Modis geolocation fields product. https://doi.org/10.5067/MODIS/MYD03.061

Mokhov, I., & Akperov, M. (2006). Tropospheric lapse rate and its relation to surface temperature from reanalysis data. *Izvestiya, Atmospheric and Oceanic Physics.*, *42*. https://doi.org/10.1134/S0001433806040037

Moody, E., King, M., Schaaf, C., Hall, D., & Platnick, S. (2007). Northern hemisphere five-year average (2000-2004) spectral albedos of surfaces in the presence of snow: Statistics computed from terra MODIS land products. *Remote Sensing of Environment*, *111*, 337–345. https://doi.org/10.1016/j.rse.2007.03.026

Murray, B., Carslaw, K., & Field, P. (2021). Opinion: Cloud-phase climate feedback and the importance of ice-nucleating particles. *Atmospheric Chemistry Physics*, *21*, 665–679. https://doi.org/10.5194/acp-21-665-2021

Nakajima, T., & King, M. (1990). Determination of the optical thickness and effective particle radius of clouds from reflected solar radiation measurements. part i: Theory. *Journal of Atmospheric Sciences*, *47*, 1878–1893. https://doi.org/10.1175/1520-0469(1990)047<1878:DOTOTA>2.0.CO;2

Parol, F., Buriez, J., Brogniez, G., & Fouquart, Y. (1991). Information content of avhrr channels 4 and 5 with respect to the effective radius of cirrus cloud particles. *Journal of Applied Meteorology*, *30*, 973–984. https://doi.org/10.1175/1520-0450-30.7.973

Pavolonis, M. (2010). Advances in extracting cloud composition information from spaceborne infrared radiances—a robust alternative to brightness temperatures. part i: Theory. *Journal of Applied Meteorology and Climatology*, *49*, 1992–2012. https://doi.org/10.1175/2010JAMC2433.1

Platnick, S., Ackerman, S., King, M., & et al. (2015). Modis atmosphere l2 cloud product (06_l2). [Accessed: 2023-08-22]. https://doi.org/10.5067/MODIS/MYD06_L2.061

Platnick, S., Meyer, K., King, M., Wind, G., Amarasinghe, N., Marchant, B., Arnold, G., Zhang, Z., Hubanks, P., Ridgway, B., & Riedi, J. (2018). MODIS cloud optical properties: User guide for the collection 6/6.1 level 2 mod06/myd06 product and associated level-3 datasets. version 1.1. *IEEEE Trans. Geosci. Remote Sens.*, *55*, 502–525. https://atmosphere-imager.gsfc.nasa.gov/sites/default/files/ModAtmo/MODISCloudOpticalPropertyUserGuideFinal_v1.1_1.pdf

Price, J. (1987). Radiometrie calibration of satellite sensors in the visible and near infrared: History and outlook. *Remote Sensing of Environment*, *22*, 3–9. https://doi.org/10.1016/0034-4257(87)90025-3

Qu, X., Hall, A., DeAngelis, A., Zelinka, M., Klein, S., Su, H., Tian, B., & Zhai, C. (2018). On the emergent constraints of climate sensitivity. *Journal of Cliamte*, *31*, 863–875. https://doi.org/10.1175/JCLI-D-17-0482.1

Reinecker, M., Suarez, M., Todling, R., Bacmeister, J., Takacs, L., Liu, H., Gu, W., Sienkiewicz, M., Koster, R., Gelaro, R., Stajner, I., & Nielsen, J. (2008). The geos-5 data assimilation system- documentation of versions 5.0.1 and 5.1.0, and 5.2.0. *27*, 118. https://ntrs.nasa.gov/citations/20120011955

Roger, J., Vermote, E., & Ray, J. (2015). *MODIS surface reflectance user's guide, collection 6. version 1.4*. https://lpdaac.usgs.gov/documents/306/MOD09_User_Guide_V6.pdf

Sassen, K. (1991). The polarization lidar technique for cloud research: A review and current assessment. *Bulletin of the American Meteorological Society*, *72*, 1848–1866. https://doi.org/10.1175/1520-0477(1991)072<1848:TPLTFC>2.0.CO;2

Sassen, K., & Benson, S. (2001). A midlatitude cirrus cloud climatology from the facility for atmospheric remote sensing. part ii: Microphysical properties derived from lidar depolarization. *Journal of Atmospheric Sciences*, *58*, 2103–2112. https://doi.org/10.1175/1520-0469(2001)058<2103:AMCCCF>2.0.CO;2

Sato, K., Inoue, J., Kodama, Y., & Overland, J. (2012). Impact of arctic sea-ice retreat on the recent change in cloud-base height during autumn. *Geophysical Research Letters*, *39*. https://doi.org/0.1029/2012GL051850

Scipy curve fit function - v1.11.2 [Accessed: 2023-08-22]. (2023). https://docs.scipy.org/doc/scipy/reference/generated/scipy.optimize.curve_fit.html

Scipy gaussian kde function - v1.11.2 manual [Accessed: 2023-08-22]. (2023). https://docs.scipy.org/doc/scipy/reference/generated/scipy.stats.gaussian_kde.html

Scott, R., Myers, T., Norris, J., Zelinka, M., Klein, S., Sun, M., & Doelling, D. (2020). Observed sensitivity of low-cloud radiative effects to meteorological perturbations over the global oceans. *Journal of Climate*, *33*, 7717–7734. https://doi.org/10.1175/JCLI-D-19-1028.1

Shupe, M., Walden, V., Eloranta, E., Uttal, T., Campbell, J., Starkweather, S., & Shiobara, M. (2011). Clouds at arctic atmospheric observatories. part i: Occurrence and macrophysical properties. *Journal of Applied Meteorology and Climatology*, *50*, 626–644. https://doi.org/10.1175/2010JAMC2467.1

Slingo, J. (1987). The development and verification of a cloud prediction scheme for the ecmwf model. *Quarterly Journal of the Royal Meteorological Society*, *113*, 899–927. https://doi.org/10.1002/qj.49711347710

Stokes, G. (1862). On the intensity of the light reflected from or transmitted through a pile of plates. *Proceedings of the Royal Society of London*, *11*, 545–556. https://www.jstor.org/stable/111970

Stramler, S., Genio, A., & Rossow, W. (2011). Synoptically driven arctic winter. *Journal of Climate*, *24*, 1747–1762. https://doi.org/10.1175/2010JCLI3817.1

Strow, L., Hannon, S., Souza-Machado, S. D., Motteler, H., & Tobin, D. (2003). An overview of the airs radiative transfer model. *IEEE Transactions on Geoscience and Remote Sensing*, *41*, 303–313. https://doi.org/10.1109/TGRS.2002.808244

Tan, I., Barahona, D., & Coopman, Q. (2022). Potential link between ice nucleation and climate model spread in arctic amplification. *Geophysical Research Letters*, *49*. https://doi.org/10.1029/2021GL097373

Tan, I., Sotiropoulou, G., Taylor, P., Zamora, L., & Wendisch, M. (2021). A review of the factors influencing arctic mixed-phase clouds: Progress and outlook. *Authorea*. https://doi.org/10.1002/essoar.10508308.1

Tan, I., Storelvmo, T., & Zelinka, M. (2016). Observational constraints on mixed-phase clouds imply higher climate sensitivity. *Science*, *352*, 224–227. https://doi.org/10.1126/science.aad5300

Taylor, P., Boeke, R., Boisvert, L., Feldl, N., Henry, M., Huang, Y., Langen, P., Liu, W., Pithan, F., Sejas, S., & Tan, I. (2021). Process drivers, inter-model spread, and the path forward: A review of amplified arctic warming. *Frontiers in Earth Science*, *9*. https://doi.org/10.3389/feart.2021.758361

Taylor, P., Boeke, R., Li, Y., & Thompson, D. (2019). Arctic cloud annual cycle biases in climate models. *European Geosciences Union*, *19*, 24. https://doi.org/10.5194/acp-19-8759-2019

Tsushima, Y., Emori, S., Ogura, T., Kimoto, M., Webb, M., Williams, K., Ringer, M., Soden, B., Li, B., & Andronova, N. (2006). Importance of the mixed-phase cloud distribution in the control climate for assessing the response of clouds to carbon dioxide increase: A multi-model study. *Climate Dynamics*, *27*, 113–126. https://doi.org/10.1007/s00382-006-0127-7

Uttal, T., Curry, J., McPhee, M., Perovich, D., Moritz, R., Maslanik, J., Guest, P., Stern, H., Moore, J., Turenne, R., Heiberg, A., Serreze, M., Wylie, D., Persson, O., Paulson, C., Halle, C., Morison, J., Wheeler, P., Makshtas, A., … Grenfeld, T. (2002). Surface heat budget of the arctic ocean. *Bulleting of the American Meteorological Society*, *83*, 255–276. https://doi.org/10.1175/1520-0477(2002)083<0255:SHBOTA>2.3.CO;2

Vaughan, M., Winker, D., & Powell, K. (2005). CALIOP algorithm theoretical basis document—part 2: Feature detection and layer properties algorithms. *NASA Langley Research Center Doc.*, PC–SCI–202. https://www-\ce{CALIPSO}.larc.nasa.gov/resources/pdfs/PC-SCI-202_Part2_rev1x01.pdf

Virtanen, P., Gommers, R., Oliphant, T. E., Haberland, M., Reddy, T., Cournapeau, D., Burovski, E., Peterson, P., Weckesser, W., Bright, J., van der Walt, S. J., Brett, M., Wilson, J., Millman, K. J., Mayorov, N., Nelson, A. R. J., Jones, E., Kern, R., Larson, E., … SciPy 1.0 Contributors. (2020). SciPy 1.0: Fundamental Algorithms for Scientific Computing in Python. *Nature Methods*, *17*, 261–272. https://doi.org/10.1038/s41592-019-0686-2

Wallace, J., & Hobbs, P. (1977). *Atmospheric science: An introductory survey*. Academic Press. https://sv.20file.org/up1/1382_0.pdf

Wang, C., Luo, Z., & Huang, X. (2011). Parallax correction in collocating cloudsat and moderate resolution imaging spectroradiometer (modis) observations: Method and application to convection study. *Journal of Geophysical Research: Atmosphere*, *116*. https://doi.org/10.1029/2011JD016097

Warren, S., & Brandt, R. E. (2008). Optical constants of ice from the ultraviolet to the microwave: A revised compilation. *Journal of Geophysical Research*, *113*, 1206–1225. https://doi.org/10.1029/2007JD009744

Winker, D., Hosteltler, C., Vaughan, M., & Omar, A. (2006). *CALIOP algorithm theoretical basis document. part 1: CALIOP instrument, and algorithms overview. volume 2.0.* https://www.researchgate.net/publication/255578893_CALIOP_Algorithm_theoretical_basis_document

Winker, D., Pelon, J., & Trepte, C. (2023). Calipso: Data user's guide - data product descriptions - lidar level 2 cloud, aerosol, and merged layer v4.20 products [Accessed: 2023-08-22]. https://www-calipso.larc.nasa.gov/resources/calipso_users_guide/data_summaries/layer/index_v420.php

Wood, R., & Bretherton, C. (2006). On the relationship between stratiform low cloud cover and lower-tropospheric stability. *Journal of Climate*, *19*, 6425–6432. https://doi.org/10.1175/JCLI3988.1

Wuebles, D., Fahey, D., & Hibbard, K. (2017). *Climate science special report: Fourth national climate assessment.* (Vol. 1). https://doi.org/10.7930/J08S4N35

Wylie, D., Piironen, P., Wolf, W., & Eloranta, E. (1995). Understanding satellite cirrus cloud climatologies with calibrated lidar optical depths. *Journal of the Atmospheric Sciences.*, *52*. https://doi.org/10.1175/1520-0469(1995)052<4327:USCCCW>2.0.CO;2

Ye, H., You, W., Zang, Z., Pan, X., Wang, D., Zhou, N., Hu, Y., Liang, Y., & Yan, P. (2022). Observing system simulation experiment (osse)-quantitative evaluation of lidar observation networks to improve 3d aerosol forecasting in china. *Atmospheric Research*, *270*, 106069. https://doi.org/https://doi.org/10.1016/j.atmosres.2022.106069

Young, S., Vaughan, M., Garnier, A., Tackett, J., Lambeth, J., & Powell, K. (2018). Extinction and optical depth retrievals for CALIPSO 's version 4 data release. *Atmospheric Measurements Techniques*, *11*, 5701–5727. https://doi.org/10.5194/amt-11-5701-2018

Yu, Y., Taylor, P., & Cai, M. (2019). Seasonal variations of arctic low-level clouds and its linkage to sea ice seasonal variations. *Journal of Geophysical Research*, *124*, 12206–12226. https://doi.org/10.1029/2019JD031014

Zelinka, M., Klein, S., & Hartmann, D. (2012a). Computing and partitioning cloud feedbacks using cloud property histograms. part i: Cloud radiative kernels. *Journal of Climate*, *25*, 3715–3737. https://doi.org/10.1175/JCLI-D-11-00248.1

Zelinka, M., Klein, S., & Hartmann, D. (2012b). Computing and partitioning cloud feedbacks using cloud property histograms. part ii: Attribution to changes in cloud amount, altitude, and optical depth. *Journal of Climate*, *25*, 3715–3737. https://doi.org/10.1175/JCLI-D-11-00249.1

Zelinka, M., Myers, T., McCoy, D., Po-Chedley, S., Caldwell, P., Ceppi, P., Klein, S., & Taylor, K. (2020). Causes of higher climate sensitivity in cmip6 models. *Geophysical Research Letters*, *47*. https://doi.org/10.1029/2019GL085782

Zelinka, M., Zhou, C., & Klein, S. (2016). Insights from a refined decomposition of cloud feedbacks. *Geophysical Research Letters*, *43*. https://doi.org/10.1002/2016GL069917

Zeng, X., Atlas, R., Birk, R. J., Carr, F. H., Carrier, M. J., Cucurull, L., Hooke, W. H., Kalnay, E., Murtugudde, R., Posselt, D. J., Russell, J. L., Tyndall, D. P., Weller, R. A., & Zhang, F. (2020). Use of observing system simulation experiments in the united states. *Bulletin of the American Meteorological Society*, *101*(8), E1427 – E1438. https://doi.org/https://doi.org/10.1175/BAMS-D-19-0155.1

Zhang, Z., Ackerman, A., Feingold, G., Platnick, S., Pincus, R., & Xue, H. (2012). Effects of cloud horizontal inhomogeneity and drizzle on remote sensing of cloud droplet effective radius: Case studies based on large-eddy simulations.

Journal of Geophysical Research: Atmospheres, *117*. https://doi.org/10.1029/2012JD017655